

Investigation of Plasma Effects in the KATRIN Source with $^{83\text{m}}\text{Kr}$

Master's Thesis of

Raphael Ostertag

at the Department of Physics
Institute for Experimental Particle Physics (ETP)

Reviewer:	Prof. Dr. G. Drexlin
Second Reviewer:	Prof. Dr. U. Husemann
Advisor:	M.Sc. Moritz Machatschek

Submission Date: 26th June 2020

Declaration of authorship

I declare that I have developed and written the enclosed thesis completely by myself, and have not used sources or means without declaration in the text.

Karlsruhe, 26th June 2020, _____

Raphael Ostertag

Accepted as master's thesis

Contents

Introduction	1
1 Neutrino physics	3
1.1 The discovery of the neutrino	3
1.2 Neutrino oscillations	3
2 The KATRIN experiment	7
2.1 Tritium β -decay	7
2.2 Experimental setup	8
2.2.1 Windowless gaseous tritium source and rear section	9
2.2.2 Transport section	10
2.2.3 MAC-E filter	11
2.2.4 Focal plane detector	14
2.3 Data analysis	15
2.3.1 Likelihood function	15
2.3.2 Gaussian error interpretation	16
3 Plasma in the KATRIN tritium source	19
3.1 Categorization and comparison	19
3.2 General plasma properties	20
3.3 Gas dynamics	23
3.3.1 Gas flow regimes in the WGTS and DPS	23
3.3.2 Calculation of the mass flow rate	23
3.3.3 Calculation of throughput for tritium and krypton	24
3.4 Plasma potential simulation	25
3.5 Experimental investigation with gaseous krypton	25
4 Modeling of the krypton mode	29
4.1 Source and spectrometer settings in krypton mode	29
4.2 Krypton spectrum	32
4.2.1 Shake up/off effect	33
4.2.2 Voigt profile	34
4.3 Spectrum modeling	35
4.3.1 Software framework	35
4.4 $^{83\text{m}}\text{Kr}$ observables	36
4.4.1 Voigt model	36
4.4.2 Scattering model	37
4.4.3 Column density dependence and comparison	42
4.4.4 Impact on the neutrino mass	42
5 Analysis of KNM2 krypton campaign	43
5.1 General methodology	43
5.1.1 Measurement procedure	43

5.1.2	Fitting procedure	44
5.1.2.1	Fit result stacking	45
5.1.2.2	Line width error propagation	45
5.1.3	Systematical uncertainties	45
5.2	KNM1 reference measurements	47
5.3	Intrinsic line width determination with $N_{2,3}$ method	49
5.4	Rear wall voltage dependent plasma regimes	52
5.4.1	Longitudinal shape	54
5.5	Radially dependent plasma potential	55
5.5.1	Radially dependent column density	56
5.5.2	Radially dependent coupling to the rear wall	56
5.6	Rear wall voltage of best radial homogeneity	61
5.7	Time dependent drifts of column densities	62
5.8	Time dependent drifts of the L_3 line position	66
5.8.1	Rear wall voltage and radially dependent drift over time	70
5.9	Azimuthally dependent observables from misalignment	70
5.9.1	Flux tube misalignment	70
5.9.1.1	Radially dependent non-adiabaticity	73
5.9.2	Asymmetrical potential	76
	Conclusion and outlook	81
	A Appendix	85
A.1	Derivation of the mass flow rate	85
A.2	Retarding potential values for L_3 line runlist	86
A.3	Documentation for python-based plot generator	86
A.3.1	Krypton plot parameters	87
A.3.2	Class reference	87
A.3.2.1	<code>__init__</code>	87
A.3.2.2	<code>DrawScatterplot</code>	87
A.3.2.3	<code>DrawHistogram</code>	89
A.3.3	Step-by-step instructions for pixel-wise KaFit results	90
A.4	Additional analysis plots	90

List of Figures

2.1	Electron energy spectrum of tritium β -decay.	8
2.2	Setup of the KATRIN experiment	8
2.3	Setup of the WGTS.	9
2.4	Measurement principle of a MAC-E-filter.	11
2.5	KATRIN response function	13
2.6	Focal plane detector system	14
3.1	Electron temperature versus density	19
3.2	Potential distribution	21
3.3	Plasma sheath model	21
3.4	Gas density profiles for tritium and krypton	24
3.5	Simulated longitudinal plasma potential profile of the WGTS	26
4.1	Loop operation in tritium mode.	30
4.2	Loop operation in krypton mode.	30
4.3	The maximum column density in krypton mode	31
4.4	Decay scheme of $^{83\text{m}}\text{Kr}$	32
4.5	Internal conversion lines of $^{83\text{m}}\text{Kr}$	34
4.6	Basic scheme of the KaFit software module,	35
4.7	Krypton spectrum observables.	37
4.8	Energy loss function for singly-scattered electrons,	38
4.9	Scattering probabilities	39
4.10	Starting potential distribution of unscattered electrons	39
4.11	Weighted plasma potential	40
4.12	Rectangular approximation of simulated plasma model	41
5.1	KNM1 reference value for the intrinsic line width	48
5.2	KNM1 reference value for the L_3 line position	48
5.3	Pseudo-ring-wise line broadening of $N_{2,3}$ lines	50
5.4	Fitted intrinsic L_3 line width	51
5.5	Histogram of fitted intrinsic L_3 line width	51
5.6	Pseudo-ring-wise line broadening over rear wall voltage.	52
5.7	Sweep-wise line broadening and line position depending on the rear wall voltage.	53
5.8	Rear wall voltage dependent energy loss shift parameter and mean plasma potential,	54
5.9	Line position versus rear wall voltage	55
5.10	Fitted column density depending on the ring number	56
5.11	Radial coupling strength in good coupling regime.	57
5.12	Simulated transversal plasma potential shape for planar plasma (2D)	59
5.13	Line broadening over radius	59
5.14	Ring-wise relative line broadening,	60

5.15	Ring-wise line positions in the good coupling regime along with the resulting standard deviation,	63
5.16	Rear wall voltage of best radial homogeneity over time	63
5.17	Fitted column density over time	64
5.18	Illustration of plasma dependence on different column density	64
5.19	Energy loss shift parameter over time	65
5.20	Averaged pixel-wise krypton count rate of over time	65
5.21	L_3 line position over time	67
5.22	Line broadening and energy loss shift over time	68
5.23	WGTS beam tube temperature over time	69
5.24	Pseudo-ring-wise line position drift depending on the rear wall voltage in the good coupling regime	69
5.25	Fitted background rate over pixels	71
5.26	Time dependence of flux tube center offset fit parameters.	71
5.27	Pixel mixing method	73
5.28	Center offset corrected fitted background rate	74
5.29	Pixel-wise line position for different rear wall voltages	74
5.30	FPD maps of the line position	75
5.31	Linear fit of normed line intensity over pixel for $N_{2,3}$ and L_3	75
5.32	Comparison of the (center offset corrected) background rate with the simulation.	76
5.33	Corrected line positions	77
5.34	exemplary potential center offset fit	78
5.35	Potential center offset fit parameters	79
A.1	Scheme of the KASPER software framework	85
A.2	Radial dependence of the line position in KNM1 reference measurement	91
A.3	Illustration of measured sweeps.	91
A.4	Line broadening comparison for two different reference values	94
A.5	Normed chi-squared for $N_{2,3}$ lines fits.	95
A.6	Ring-wise line broadening of $N_{2,3}$ lines	95
A.7	Line position over ring number	96
A.8	Energy loss shift parameter over time	96

List of Tables

2.1	Ring-wise pixel segmentation	14
4.1	Energies of conversion electron spectral lines of $^{83\text{m}}\text{Kr}$	33
5.1	Fit results of Fick's equation	57
A.1	KNM2 krypton L_3 runs	92
A.2	KNM2 krypton $N_{2,3}$ runs	93
A.3	Sweep numbers with their included run numbers	93
A.4	KNM1 krypton L_3 reference runs	93
A.5	2.7 G field setting in krypton mode.	93
A.6	Pseudo-ring-wise line broadening values for $N_{2,3}$	94

List of Abbreviations

Abbreviation	Meaning
AP	A nalyzing P lane
BIXS	B eta-ray I nduced X -ray S pectrometry
CD	C olumn D ensity
CPS	C ryogenic P umping S ection
DPS	D ifferential P umping S ystem
eLFCS	extended L ow F ield C ompensation S ystem
EMCS	E arth M agnetic F ield C ompensation S ystem
FPD	F ocal P lane D etector
FSD	F inal S tate D istribution
FT-ICR	F ourier T ransform I on C yclotron R esonance
ICR	I nnner C onversion
IE	I nnner E lectrodes
KATRIN	K ARlsruher T RITium N eutrino
KIT	K arlsruhe I nstitute of T echnology
KNMX	K ATRIN N eutrino M ass (measurement campaign) X ($\mathbf{X} \in \mathbb{N}$)
MAC-E Filter	M agnetic A diabatic C ollimation with E lectrostatic F iltering
MS	M ain S pectrometer
MTD	M easurement T ime D istribution
PAE	P ost A cceleration E lectrode
PDF	P robability D ensity F unction
PS	P re S pectrometer
RW	R ear W all
SM	S tandard M odel
SPD	S tarting P otential D istribution
UHV	U ltra H igh V acuum
WGTS	W indowless G aseous T ritium S ource

Introduction

After the postulation of the neutrino 90 and its experimental discovery more than 60 years ago, the subsequent neutrino research is ever since one important field in particle physics. Among photons, neutrinos are the most frequent particles in the universe and carry important information about its structural formation. Because neutrinos only interact weakly with other particles, it is challenging to detect them. Experiments like IceCube [Ice11] or SNO+ [Loz14] have large instrumented volumina to reach significant detection rates.

With the discovery of neutrino oscillation [Fuk98] and the resulting conclusion of massive neutrinos, the question of the weight of the neutrinos naturally arises. The determination of the model-independent neutrino mass scale is the goal of the KARlsruher TRItium Neutrino (KATRIN) collaboration which has been performing successfully m_ν measurements since 2019 [Ake+19], and set the world-leading upper limit in direct m_ν measurements of

$$m_\nu \leq 1.1 \text{ eV}/c^2 \quad (90\% \text{ C.L.}).$$

The desired goal is to increase this sensitivity further down to $200 \text{ meV}/c^2$ (90% C.L.) in the next 1000 days of measurement time. The consequences for the experimental requirements are tremendous. Possible sources of systematic uncertainties, which were negligible before, are becoming relevant and need to be improved.

KATRIN's approach for the m_ν determination is a direct kinematic measurement of electrons which are produced in the β -decay of molecular tritium. The high precision spectroscopy of the β -spectrum near the endpoint of 18.6 keV is achieved with a high activity source and a large scale MAC-E filter. Additionally, a consistently high demand for the minimization of the systematic uncertainties is required. As an example, the potential inside the windowless gaseous tritium source (WGTS) is majorly influenced by a cold, low density plasma. The KATRIN plasma is mainly driven by self-ionization caused by the radioactive decay of tritium and inelastic scattering of β -electrons which leads to many charged ions and secondary electrons. The result is a spatially varying starting potential of the electrons, which leads to a non-uniform starting potential distribution. The standard deviation σ of energy scale smearings convolved with the spectrum leads in leading order to a negative shift of the measured squared neutrino mass [Rob10]

$$\Delta m_\nu^2 = -2\sigma^2.$$

Hence, the plasma plays an important role in the m_ν analysis and must precisely be measured.

One way to measure the longitudinal plasma potential profile is to use an additional gas as nuclear standard in the source. $^{83\text{m}}\text{Kr}$ has been used in the predecessor experiment in Troitsk [Bel+08] and is also a feasible candidate at KATRIN. Its gaseous state leads to almost the same density profile as for tritium enabling the spatial investigation of the KATRIN source plasma potential. Also, $^{83\text{m}}\text{Kr}$ provides quasi-monoenergetic electrons from internal conversion processes in the favorable energy range of the tritium endpoint. The

latter is important for not having β -electrons as background. The inhomogeneity of the starting potential distribution can be approximated by fitting the Gaussian broadening of the measured $^{83\text{m}}\text{Kr}$ conversion electron line.

The topic of this thesis is the planning, execution, and analysis of these commissioning measurements with $^{83\text{m}}\text{Kr}$ in the second KATRIN neutrino mass measurement campaign (KNM2).

This thesis is divided into five chapters.

Chapter 1 gives a brief overview of neutrino physics, including the historical background from the discovery itself, and neutrino oscillation as motivation for non-vanishing masses. Chapter 2 introduces the KATRIN experiment and explains all components which are necessary to understand the principle and the analysis of the krypton measurements.

Chapter 3 focuses on the cold low density KATRIN plasma. It is categorized and compared to other types of plasmas, general plasma properties are explained, and the existing approach of plasma simulation is introduced. At the end, the need of the krypton measurements is motivated.

Chapter 4 covers the krypton mode used for the investigation of the systematic caused by the plasma. This includes the source and spectrometer settings, their differences to neutrino mass scans, the krypton spectrum and its modeling, the gas dynamics in mixture with tritium, and the krypton observables of the measurements which are used in the analysis.

Chapter 5 deals with the krypton measurements which took place in December of 2019. At the beginning, the general methodology is explained, followed by analyses which allow different views on the radial and longitudinal structure of the source plasma potential. Additionally, the $^{83\text{m}}\text{Kr}$ observables are used to quantify different alignment effects within the beam line.

1. Neutrino physics

In 1930, Wolfgang Pauli postulated the neutrino particle [Mey85] to explain the observed continuous energy spectrum of electrons/ positrons, respectively emitted in β -decay (Sect. 2.1). Consequently, the processes cannot be described as two body decay anymore because this would violate both energy and angular momentum conservation. Rather, three-body decay models are valid:

$${}^A_Z\text{N} \rightarrow {}^A_{Z+1}\text{N} + e^- + \bar{\nu}_e \quad \text{and} \quad {}^A_Z\text{N} \rightarrow {}^A_{Z-1}\text{N} + e^+ + \nu_e. \quad (1.1)$$

Here, A is the mass number and Z the atomic number of element N , $e^-/+$ represents an electron/ positron and $\nu_e, \bar{\nu}_e$ an electron neutrino and its antiparticle.

Pauli derived some criteria for the new, hypothetical particle. It must have no charge, its spin must be $S = 1/2$ and it should only interact weakly with other particles, otherwise it would have been found already. On the other hand, it was not yet possible to give an approximation of its mass.

1.1 The discovery of the neutrino

26 years later, in 1956, the neutrino was detected for the first time. The Poltergeist experiment by Cowan and Reines [Cow56] investigated the interaction between reactor antineutrinos from the Savannah River nuclear reactor and protons of 200l of water. The corresponding absorption reaction of the inverse β -decay reads as

$$\bar{\nu}_e + p \rightarrow e^+ + n, \quad (1.2)$$

in which p is a proton and n a neutron. To detect the neutron, 40 kg of cadmium chloride (CdCl_2) is added to the water to make use of the so-called delayed coincidence signature of both created particles. The positron emits two photons from annihilation with an electron and the neutron gets captured by the cadmium chloride. The latter quickly de-excites under the emission of a 10 μs delayed photon. The detection of both signals showed the antineutrino interaction.

In the upcoming years also the muon neutrino ν_μ [Dan62] and the tau neutrino ν_τ [Kod+01] were discovered.

Experiments like ALEPH [DeC89] showed that there are only three generations of neutrinos, which were then included in the standard model of particle physics. They belong to the family of leptons ($S = 1/2$), but carry no electric charge. Neutrinos have negative and antineutrinos positive chirality [Wu+57] which is the reason for parity violation within the weak interaction [LY56].

1.2 Neutrino oscillations

The sun is, due to the high number of massive fusion processes, a source of electron neutrinos. The Homestake experiment [DHH68] was designed to detect these neutrinos

by the radiochemical reaction



Despite the large mass of 615 t of perchloroethylene (C_2Cl_4) the detection rate was smaller than 1 interaction/day. By analyzing the amount of Ar atoms in the tank, it was found that the detected neutrino rate was only 1/3 of the expected one. This discrepancy is known as the solar neutrino problem and was the basis for the postulation of neutrino oscillations.

However, periodic changes of the neutrino's flavor to another $\nu_i \rightarrow \nu_j$ are only possible for non-zero masses [Pon67], which was a contradiction to the common understanding of that time. Consequently, the identified flavors of neutrinos $\nu_\alpha \in \{\nu_e, \nu_\mu, \nu_\tau\}$ are no mass eigenstates ν_i , but a superposition of them

$$|\nu_\alpha\rangle = \sum_i U_{\alpha i} |\nu_i\rangle . \quad (1.4)$$

This formulation enables the transition between the different flavors depending on the Pontecorvo-Maki-Nakagawa-Sakata (PMNS) mixing matrix U . The first experimental validation of this concept was achieved in 1998 by the Super-Kamiokande collaboration [Fuk98] which investigated the angular dependence of atmospheric neutrinos. Atmospheric neutrinos are secondary particles from cosmic rays. In most of the cases, high energy protons are entering the atmosphere where they create pions and kaons which further decay into muons and muon neutrinos. The muons decay into electrons/ positrons, along with both muon and electron (anti) neutrino.

The Super-Kamiokande collaboration investigated the ν_μ and thereby discovered a significant asymmetry in the muon neutrino flux up-going and down-going to earth. Neutrinos propagating upwards must traverse the earth globe before they reach the detector and therefore must travel longer distances on the order of 10^3 km than neutrinos moving downwards which only cover distances on the level of 10 km. Thus, in the first case, there is more time for oscillating from the muon into the tau flavor $\nu_\mu \rightarrow \nu_\tau$ which explains the measured muon neutrino deficit in upward direction.

Four years later, SNO [Ahm02] provided the corresponding evidence for solar neutrino oscillations from the electron into the muon state.

Mixing parameters

The PMNS matrix introduced in Eq. (1.4) contains the information about the transition probabilities of the different flavor eigenstates. It is a complex 3×3 matrix, which has in general 18 degrees of freedom. With the unitary restriction $U^\dagger U = 1$, it can be reduced by nine and with the absorption of five phases in lepton fields, the PMNS matrix can fully be described by four parameters. In the standard parametrization, these are three mixing angles θ_{ij} and one complex phase δ_{13} .

The transition probability is given by

$$P(\nu_\alpha \rightarrow \nu_\beta) = |\langle \nu_\beta | \nu_\alpha \rangle|^2 , \quad (1.5)$$

leading to different channels depending on the flavor. For instance, in two flavor approximation, Θ_{ij} reduces to Θ and the probability to detect a new flavor ν_β in a ν_α flux is given by

$$P(\nu_\alpha \rightarrow \nu_\beta) = \sin^2(2\theta) \sin^2\left(\Delta m^2 \frac{L}{4E}\right) , \quad (1.6)$$

in which E is the energy and L the traveled distance of the neutrino. This relation can be used in reactor and long-baseline measurements. By tuning the ratio L/E , one can choose the channel in which the experiment's sensitivity is maximized. Hereby, the amplitude

of the oscillation is given by the mixing angle θ and the frequency by the squared mass difference Δm^2 . Along with measurements of solar and atmospheric neutrinos, the values in normal ordering are determined to [Est+19]

$$\begin{aligned}\theta_{12} &\approx 33.8^\circ & \text{and} & & \Delta m_{21}^2 &\approx 7.39 \cdot 10^{-5} \text{ eV}, \\ \theta_{23} &\approx 48.6^\circ & \text{and} & & \Delta m_{32}^2 &\approx 2.53 \cdot 10^{-3} \text{ eV}, \\ \theta_{13} &\approx 8.60^\circ & \text{and} & & \Delta m_{31}^2 &\approx 2.53 \cdot 10^{-3} \text{ eV}.\end{aligned}$$

The major disadvantage of neutrino experiments which measure the mixing angles θ_{ij} and the squared mass differences Δm_{ij} is that they are not sensitive to the absolute mass scale. This parameter can for instance be determined by a direct kinematic neutrino mass measurements of β -decay electrons. This approach has successfully been realized with tritium in Troitsk [Ase11] and Mainz [Kra05] and is still pursued in the KATRIN experiment [Ang+05]. The latter provided the world-leading upper limit for the absolute neutrino mass of [Ake+19]

$$m_\nu \leq 1.1 \text{ eV}/c^2 \quad (90\% \text{ C.L.}). \quad (1.7)$$

2. The KATRIN experiment

The major goal of the KATRIN collaboration is to precisely determine the neutrino mass via a direct kinematic measurement of electrons from the radioactive β -decay of tritium (${}^3\text{H}$). To achieve this goal, KATRIN is restricted to the high-energy tail of the energy spectrum, where almost all of the energy of the decay is carried by the electron. A non-zero neutrino mass m_ν would shift the spectrum endpoint by $\Delta E = m_\nu c^2$ to lower energies and distort the spectral shape in the endpoint region.

Due to the determination of simple, kinematic parameters and the usage of the well known energy and momentum conservation, the measurement principle allows a model-independent determination of the neutrino mass. The desired sensitivity in doing so is $\Delta m_{\bar{\nu}_e} = 0.2 \text{ eV}/c^2$, which leads to an approximately 100 better determination of $m_{\bar{\nu}_e}^2$ [Rei13] than in the previous experiments in Troitsk [Ase11] and Mainz [Kra05]. This can only be achieved with a consistently high demand for both statistics and systematics of all used components [Ang+05].

This chapter explains all components and principles of the KATRIN experiment which are relevant for the understanding of the experiment. In the beginning, the special case of tritium beta-decay (Sect. 2.1) and the experimental setup (Sect. 2.2) are explained based on [Ang+05]. At the end, a brief introduction in data analysis of the measurements which are recorded at KATRIN is given (Sect. 2.3).

2.1 Tritium β -decay

At KATRIN, the (anti)neutrino is created via the β^- -decay of molecular tritium ${}^3\text{H}$

$${}^3\text{H} \rightarrow {}^3\text{He}^+ + e^- + \bar{\nu}_e. \quad (2.1)$$

Aside from the antineutrino, a heavy helium ion ${}^3\text{He}^+$ and an electron are created, which are crucial for the used measurement principle. The energy in this three-body decay is randomly distributed among the different final-state particles. Indirectly, the antineutrino mass can be inferred from the obtained shape of the electron energy spectrum around the endpoint at $E_0 \sim 18.57 \text{ keV}$. The ion has the largest mass and moves slowly along the magnetic field lines towards the differential pumping section where they are getting blocked by ring electrodes. On the other hand, the neutrino leaves the setup immediately with the speed of light and without any further interference due to its tiny interaction cross sections. Hence, only the electron is guided to the detector. A theoretical model of the differential spectrum dN/dE can be derived from Fermi's golden rule [Fer34]

$$\frac{dN}{dE} = R \cdot \sqrt{(E_0 - E)^2 - m_{\bar{\nu}_e}^2 c^4} \theta(E_0 - E - m_{\bar{\nu}_e} c^2), \quad (2.2)$$

with

$$R = \frac{G_F^2}{2\pi^3 c^5 \hbar^7} \cos^2 \theta_C |M|^2 \times F(Z + 1, E) \cdot p_e (E + m_e c^2) (E_0 - E).$$

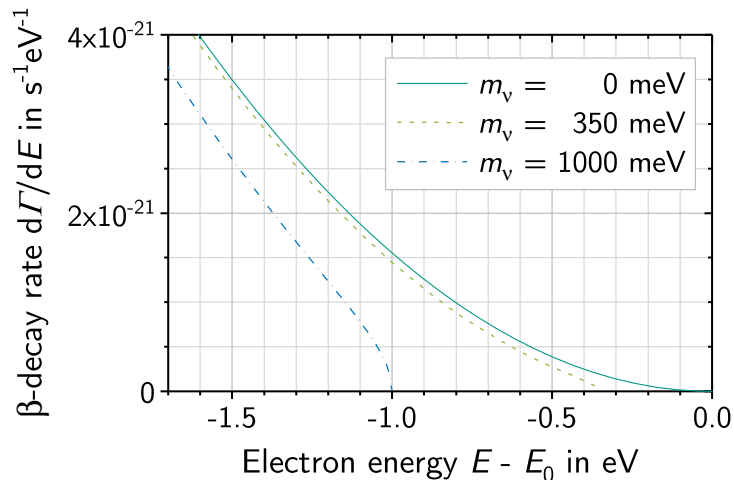


Figure 2.1: Electron energy spectrum of tritium β -decay. The differently colored lines show how the spectrum would look like for massless, light, and heavy neutrinos. Additionally, it visualizes the small scale of the endpoint region. Figure from [Kle+19] (modified).

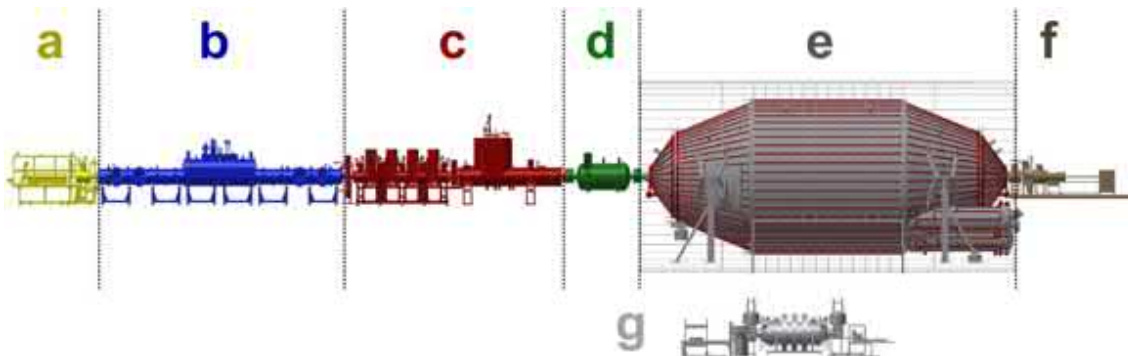


Figure 2.2: Setup of the KATRIN experiment with the different sections. The electrons originate from β -decay of the tritium gas contained inside the WGTS (b). The so-called rear section (a) allows calibration and monitoring of the WGTS. The transport section (c) is composed of different vacuum pumps and solenoid magnets to reduce the tritium flux and guide the electrons to the pre spectrometer (PS). The PS (d) is a pre-filter which reduces the electron flux reaching the main spectrometer significantly by blocking low energy electrons. The remaining ones are guided into the MS (e) for energy analysis, which is described in Sect. 2.2.3. Its applied high voltage of the retarding potential is monitored by the monitor spectrometer (g). Finally, the electrons with sufficiently high energy hit the FPD (f). Figure from [Har15].

Here, E is the kinetic energy of the electron with mass m_e , E_0 is the endpoint energy, p the momentum of the electron, G_F the Fermi constant, θ_C the Cabbibo angle, $F(Z + 1, E)$ the Fermi function, c the speed of light, and M the nuclear matrix element. The theta function θ ensures energy conservation.

The spectrum is shown in Fig. 2.1. The fraction of emitted electrons in the region of interest, i.e. within an energy range of 1 eV below the endpoint, is only $2 \cdot 10^{-13}$. Therefore, a high-activity source is indispensable to accumulate sufficiently high count rates.

2.2 Experimental setup

The experiment is located at the Karlsruhe Institute of Technology (KIT), Campus North. The beam line is subdivided into different systems (sections), each fulfilling a specific task.

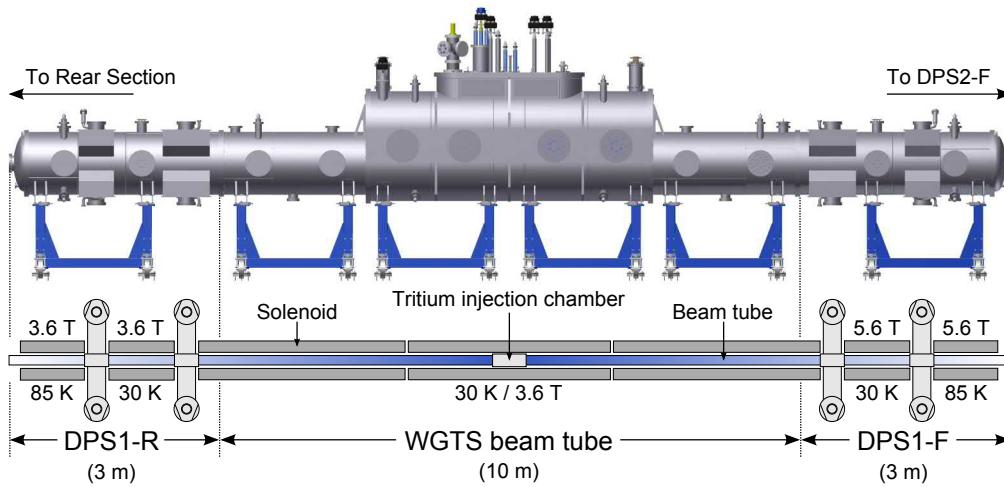


Figure 2.3: Setup of the WGTS. Two differential pumping systems are mounted at the front and rear side of the WGTS. This leads to a decrease in density towards the ends, indicated by the blue colored band in the beam tube. The beam tube itself is surrounded by superconducting solenoids which create strong magnetic fields to guide the charged particles inside. Figure from [Har15].

Thereby, the electrons pass each section of the 70 m long beam line from the source to the detector consecutively (Fig. 2.2). The most important ones are explained in the following.

2.2.1 Windowless gaseous tritium source and rear section

Starting point of the β -electrons is inside the windowless, gaseous tritium source (WGTS), a 10 m long tube with a diameter of 90 mm. There are no windows at the tube's ends which minimizes possible systematic effects due to energy loss inside the material. To one end, the electrons can leave the source tube undisturbed while at the rear end the gold-plated rear wall is housed in the so-called rear section (RS). The rear wall can independently from the rest of the beam tube be set to an electric potential, and illuminated by UV light via a CERMAX lamp. It is meant to provide stable boundary conditions for the tritium plasma gas.

The latter can cause an inhomogeneous starting potential distribution of the electrons, which causes a significant systematic effect on the neutrino mass analysis. The investigation of the shape of this plasma potential is the topic of this thesis and discussed in detail in Chap. 3.

The gas has a tritium purity of $\geq 95\%$ and is continuously monitored by a Laser Raman (LARA) setup. The gas is injected at a rate of $5 \cdot 10^{19}$ molecules/s at the center of the WGTS (Fig. 2.3). At this point, a within 0.1% constant partial pressure of $\lesssim 3 \cdot 10^{-3}$ mbar takes ~ 1 s for the molecules to diffuse to the ends, where they get pumped out causing a non-linear decrease of the density by a factor of ~ 100 . This is one necessary measure to prevent the gas molecules from reaching the spectrometer section. The resulting activity in the flux tube is $1.7 \cdot 10^{11}$ Bq which can be monitored by two beta-ray induced X-ray spectrometry (BIXS) detectors [Rö15].

The low temperature of 30 K reduces the broadening due to doppler and plasma effects and allows the integrated tritium density along the beam axis inside the WGTS, the column density (CD), of $\rho d \approx 5 \cdot 10^{21} \text{ m}^{-2}$. The desired stability of the column density is within 0.1%.

The emitted β -electrons are guided adiabatically in the magnetic field of 3.6 T – 5.6 T, created by superconducting solenoids, towards the transport section. Along with the flux tube radius of $r = 4.5$ cm, KATRIN is designed to a transported magnetic flux of

$\Phi = 191 \text{ T cm}^2$, which is $\sim 85\%$ of the initial magnetic flux of $\Phi \approx B \cdot A = 229 \text{ T cm}^2$ inside the WGTS.

Rear wall

The rear section at the end of the WGTS houses the rear wall and fulfills many purposes and requirements, which can be found in [Sch16]. An important one for the krypton measurements is the electric coupling to the plasma. The rear wall surface potential can be tuned via regulating the applied bias voltage, independently from the rest of the beam tube. This enables the investigation of the plasma potential to understand its behavior or to determine a voltage set point which minimizes systematic plasma effects. Also, the current induced by ions and electrons from the rear wall against a reference potential can be measured.

CERMAX UV lamp

Primarily to produce photoelectrons emitted from the rear wall, a high intensity xenon lamp is installed in the rear section. Additional photoelectrons inside the source improve the electric coupling between the rear wall and the plasma [Ang+05; Ful20].

The total CERMAX power output is $\sim 1 \text{ kW}$ in a broad wavelength range of $\lambda \gtrsim 1 \mu\text{m}$. However, only a fraction corresponding to 2.1 W is UV light with $\lambda \leq 260 \text{ nm}$. Via beam splitters and lenses, only the UV light is shining to the rear wall [Bie17].

Additionally, it is possible to use the CERMAX to clean the rear wall surface from adsorbates which cause unwanted surface effects.

Krypton mode of the WGTS

The investigation of all these different source effects has been performed dedicated measurements with gaseous krypton, which are the focus of this thesis.

The idea is to have in addition to tritium $^{83\text{m}}\text{Kr}$ gas in the source, which produces quasi-monoenergetic electrons allowing the longitudinal investigation of the plasma potential. To perform these measurements, some changes in operational settings, e.g. temperature, must be made which must be considered in the analysis. Details about this realization are explained in Chap. 3.

2.2.2 Transport section

In the transport section (Fig. 2.2.c), the β -electrons are guided adiabatically along the magnetic field lines towards the spectrometer section. Another main purpose for the transport section is to reduce the tritium flow by more than 14 orders of magnitude. The transport section is subdivided into the differential (DPS) and cryogenic pumping section (CPS).

DPS

Four turbomolecular vacuum pumps reduce the tritium density by at least seven orders of magnitude. The pumps are mounted at beam line pump ports located in between five individual beam tube sections which are surrounded by a solenoid magnets. They are aligned in a 20° angle in between two consecutive parts to prevent tritium molecules passing in a direct line of sight without getting scattered into the pump entrances. Additionally, two positively biased ring electrodes at the downstream end of the DPS block positively charged ions (e.g. $^3\text{HeT}^+$) and dipole electrodes remove the stored ions via $E \times B$ -drift in negative dipole potentials [Kle19]. To monitor the different ion species, a FT-ICR penning trap is installed at the end of the DPS [Dia11].

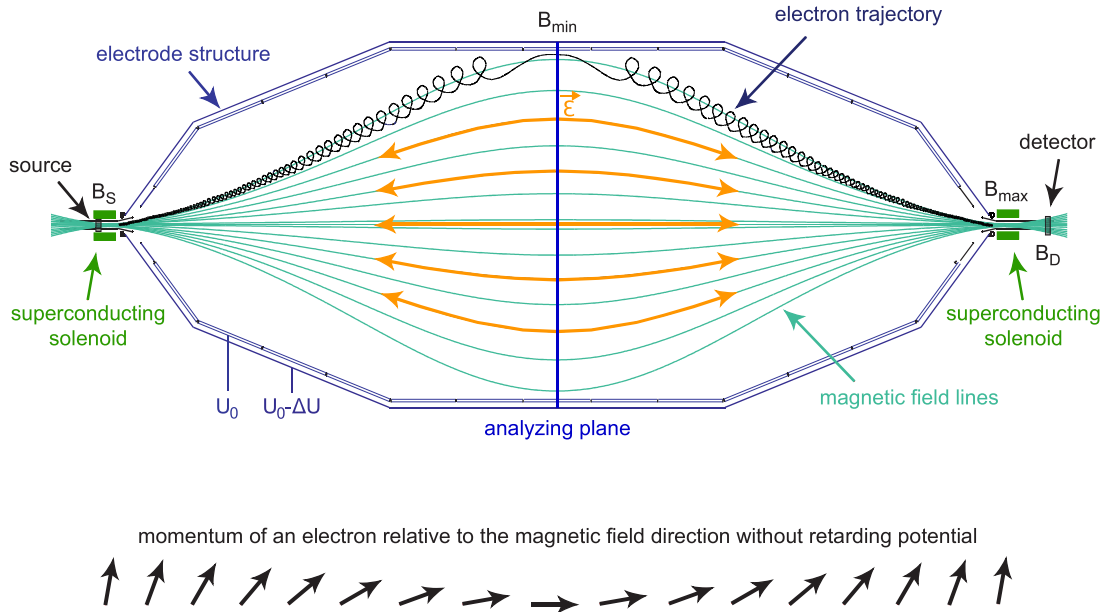


Figure 2.4: Measurement principle of a MAC-E-filter. Two superconducting solenoids at both ends of the spectrometer (green) create an axial magnetic field which field lines (turquoise) guide the electrons on a cyclotron motion through the spectrometer (black). The electrode system (blue) inside the spectrometer creates a retarding potential. The arrows below indicate the change of the momentum direction of the electrons. Thereby, the change of the momentum due to the retarding potential is ignored. Figure from [Erh16].

CPS

The CPS is located downstream of the DPS. Due to the reduced tritium flow, a differential pumping approach is not efficient anymore. Thus, a different pumping mechanism is realized in the CPS. The beam tube is cooled down via liquid helium to $T = 3\text{ K} - 5\text{ K}$. At this temperature, tritium is efficiently pumped via cryosorption at a layer of argon frost, prepared on the inner CPS beam tube surface. This process reduces the tritium flux by at least another seven orders of magnitude. After 60 days of measuring time, the beam tube must be purged with gaseous helium to remove the argon layer along with the adsorbed tritium. Afterwards, a fresh argon layer is prepared. As in the DPS, the beam tube is also slightly curved to block straight going molecules.

2.2.3 MAC-E filter

Magnetic adiabatic collimation with electrostatic filtering (MAC-E filter) is a well established technique for measuring an energy spectrum near the kinematic endpoint [KAT01], which has also been used in the predecessor experiments. Inside the spectrometer, a combination of an electric and a highly inhomogeneous magnetic field is used for creating a high-pass energy filter for β -electrons. The basic idea is to focus the momentum direction of the electrons by converting the transversal component to a longitudinal one without losing or gaining energy (Fig. 2.4). In adiabatic motion, the magnetic moment $\mu = E_{\perp}/B$ is conserved which allows the reduction of the transversal energy of the electrons E_{\perp} by reducing the magnetic field B along the symmetry axis of the spectrometer.

Only if the magnetic field gradient is small enough, fulfilling

$$\Delta B_{\text{rot}}/B \ll 1, \quad (2.3)$$

it is assured that the electron energy is not affected during the process. Here, ΔB_{rot} is the magnetic field difference for one cyclotron rotation.

The inhomogeneous magnetic field is provided by two superconducting magnets mounted at both ends of the MAC-E filter. Additionally, electrodes are installed cylindrically inside the spectrometer creating the retarding potential U_0 at the analyzing plane to only pass electrons of charge q with sufficiently high energy qU_0 . By changing the potential U_0 , the threshold energy for the electrons changes accordingly which enables an integrated measurement of the spectrum. After passing the analyzing plane, the electrons are accelerated to their original energy and enter the detector section (Sect. 2.2.4).

Energy resolution

If the condition stated in Eq. (2.3) is fulfilled, the ratio of smallest and highest magnetic field strength B_{\min}/B_{\max} describes the fraction of the transversal energy which can be converted into the longitudinal component. Hence, it is a measure of the energy resolution as referred to the filtering width of a MAC-E filter for an electron with energy E

$$\Delta E = E \cdot \frac{B_{\min}}{B_{\max}}. \quad (2.4)$$

The minimal magnetic field strength B_{\min} is given by the field in the analyzing plane $B_{\text{ana}} = 300 \mu\text{T}$, which is $2 \cdot 10^4$ times smaller than the maximal magnetic field strength $B_{\max} = 6 \text{ T}$ along the magnetic field lines of the strong magnetic field of the superconducting pinch magnet. The resulting energy resolution at the endpoint is

$$\Delta E = 0.93 \text{ eV}. \quad (2.5)$$

It should be noted that according to Eq. (2.4), the energy resolution depends linearly on the scale of the electron energy.

Maximum acceptance angle

In this setup with varying magnetic field, it is possible that particles get magnetically reflected if the initial polar angle θ_i , defined as the angle between their momentum and the magnetic field line at their creation site in the WGTS, is larger than the maximum acceptance angle θ_{\max} , at which the electrons do not reach the detector anymore. The maximum acceptance angle is given by the magnetic-mirror effect, which describes the energy-independent conversion of transversal energy E_{\perp} into the longitudinal component E_{\parallel} . This is the case if an electron travels into a region of higher magnetic field, where its polar angle θ increases. If θ of an electron reaches 90° , it gets reflected. Because the magnetic field in the source B_s is smaller than the maximum magnetic field strength at the pinch magnet B_{\max} , the maximum acceptance is given by

$$\theta_{\max} = \arcsin \sqrt{\frac{B_s}{B_{\max}}} = \arcsin \sqrt{\frac{3.6 \text{ T}}{6 \text{ T}}} = 50.77^\circ. \quad (2.6)$$

By changing the magnetic field setting, the maximum acceptance angle can be tuned. Because electrons with large θ_i have a longer pathlength inside the spectrometer and are consequently more likely to lose energy via scattering processes or synchrotron radiation, the current value of θ_{\max} is set to reduce this contribution to the systematic uncertainty of the filter.

Transmission function

The transmission function describes the probability of an electron to get transmitted by the MAC-E filter. It connects the physical decay process, represented by the differential spectrum $\frac{dN(E_0, m_\nu^2)}{dE}$ from Eq. (2.2), to the rate

$$R(qU_0) \propto \int_{qU_0}^{E_0} \frac{dN}{dE}(E_0, m_\nu^2) \cdot T(E, qU_0) dE, \quad (2.7)$$

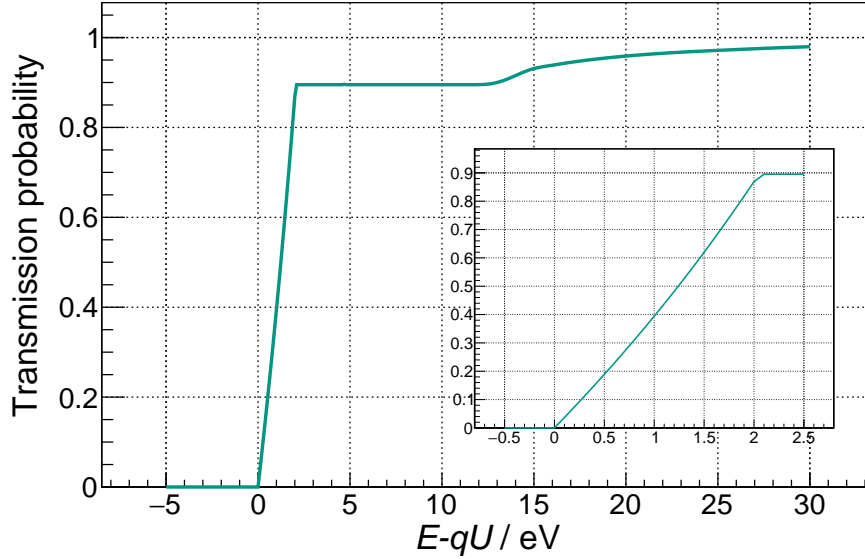


Figure 2.5: KATRIN response function at nominal neutrino mass measurement conditions describing the transmission probability depending on the surplus energy $E - qU_0$. For small surplus energies < 2 eV, the response function represents the transmission function and is shown in the detailed view on the bottom right. Plot inspired by [Gro15] and made with `KaFit` (KATRIN fitting software introduced in Sect. 4.3.1).

which is measured by the detector. Here, $T(E, qU_0)$ describes the transmission function depending on the electron energy E and the retarding potential U_0 . Because the differential spectrum contains the information about the parameter m_ν , it is crucial to know precisely the transmission function to deconvolute this information from the integral.

The transmission function depends mainly on the surplus energy $E_+ = E - qU_0$ and the initial angular distribution of the electrons in the source. Combining these two parameters, the transmission function of isotropically distributed electrons can be divided into three regions

$$T(E, E_+) = \begin{cases} 0 & \text{if } E_+ < 0 \\ 1 - \sqrt{1 - \frac{E_+}{E} \frac{B_s}{B_{\text{ana}}}} & \text{if } 0 \leq E_+ \leq \Delta E \\ 1 - \sqrt{1 - \frac{B_s}{B_{\text{max}}}} & \text{if } E_+ > \Delta E. \end{cases} \quad (2.8)$$

One can see that the full transmission is limited by the maximum acceptance angle θ_{max} . The transmitted electrons are confined within in flux tube from the source to detector. In between, their spatial extension changes while the magnetic field changes inversely. The conserved quantity is called magnetic flux and is defined as

$$\Phi = \int_A \mathbf{B} \cdot d\mathbf{A} = \text{const} \approx B \cdot A. \quad (2.9)$$

KATRIN is designed for a magnetic flux of $\Phi = 191 \text{ T cm}^2$ which serves as a boundary condition for the modulation of the electromagnetic input parameters of the transmission function [Erh16].

Additionally, there are several other effects which have an influence on the electron energy after creation and thus on the transmission function. Prominent examples are the energy loss due to inelastic scattering on tritium gas inside the WGTS, synchrotron radiation, and the Doppler effect. Those effects are covered by the response function which extends the transmission function.

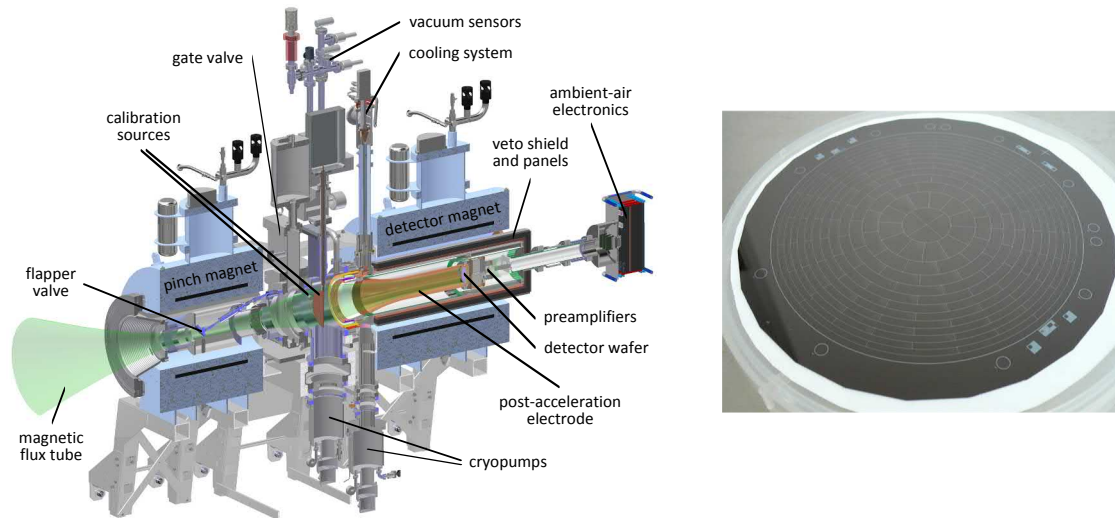


Figure 2.6: Focal plane detector system (left) and its silicon detector wafer (right). The size of the sensitive magnetic flux tube from the main spectrometer is reduced by two superconducting solenoids, pinch magnet, and detector magnet. The thereby magnetically guided electrons get additional energy from the post-acceleration electrode to enhance the signal-to-noise ratio of the detector and to reduce back scattering. Figure from [Erh16].

Table 2.1: Ring-wise pixel segmentation used in the analysis. The bull’s eye only comprises 4 pixels, instead of 12, and is defined as ring 0. Ring 12 is the outermost ring and is excluded in the measurement-specific pixel selection. In some cases, it is useful to combine rings to so-called pseudo-rings for the analysis, allowing a better visibility and higher statistics. The distance of the ring radii decreases, because each pixel covers the same area.

Ring	Pseudo-ring	Pixels	Outer bound radius / mm
0	0	0 - 3	7.398
1	0	4 - 15	14.796
2	0	16 - 27	19.573
3	1	28 - 39	23.394
4	1	40 - 51	26.674
5	1	52 - 63	29.592
6	2	64 - 75	32.245
7	2	76 - 87	34.699
8	2	88 - 99	36.990
9	3	100 - 111	39.146
10	3	112 - 123	41.190
11	3	124 - 135	43.137
12	3	136 - 147	45.000

2.2.4 Focal plane detector

At the downstream end of the beam line, the β -electrons are eventually measured by the detector system (Fig. 2.6). Hereby, the electrons which have passed the retarding potential of the MAC-E filter are magnetically guided to the individual pixels of the silicon detector wafer. Therefore, the superconducting pinch (PGH) and detector magnet (DET) create a 6 T and 3.6 T strong magnetic field. To reduce back scattering and to enhance the signal-to-noise ratio, the electron energies are increased up by 10 keV via the post-acceleration electrode (PAE). This allows a better background discrimination because of the relatively

low energy resolution of the detector wafer of ~ 1 keV. Further, the detector is surrounded by lead and copper, acting as a passive shielding. Additional plastic scintillators are used as an active veto system for cosmic ray background.

The detector wafer itself has a diameter of 9 cm and a thickness of 500 μm . It is a monolithic silicon PIN-diode array, segmented into 148 individual pixels. They are equally sized and aligned in a 4 pixels bull's eye surrounded by 12 rings of 12 pixels each (exact values can be found in Tab. 2.1). As a result, the FPD can resolve radial and azimuthal effects within the beam line. This is important for the investigation of source effects because the strong magnetic fields along the beam line cause the electrons to stay in their radially relative position (x and y), mapping the position of origin directly onto the FPD. Further, if a bias voltage is applied to the rear wall, a radially dependent coupling of the plasma can be analyzed. Some pixels cannot be used due to alignment and other technical issues which leads to 117 which can be used for analysis.

After the second KATRIN neutrino mass measurement (KNM2), the FPD wafer was replaced by an identically dimensioned new one providing a better energy resolution and an increased upper limit for the measurable rates.

2.3 Data analysis

Measuring a fundamental property like the neutrino mass with the KATRIN setup is a challenging task. Although, the general process is simple: Electrons are leaving the source, get transported, overcome the retarding potential (or not) and reach the detector. The result is the count rate which must be interpreted considering all the different parameters and settings used during the measurement. To do so, a sophisticated model must be developed which calculates the expected count rate $N_{\text{theo},i}(\mathbf{p})$, given the complex parameter configuration \mathbf{p} . Moreover, the expected count rate must be compared with the measured one which allows the derivation of the parameters of interest.

Ultimately, this is only achievable by a comprehensive software framework like `KaFit` with all its different components. The most important software packages which are necessary for the krypton analysis are introduced in Sect. 4.3.

For the comparison of expected and observed rate, there are many different approaches available, which can in first order be divided into *Bayesian* and *frequentist* methods. Hereby, the main difference is how each strategy interprets probability and thus how systematic errors are treated. A frequentist probability is defined by the relative frequency of the results of many independent events. A Bayesian probability on the other hand represents a personal degree of belief by restricting the parameter in advance, the prior. For data analysis in KATRIN, both methods correspond to each other, as it has been shown in [Kle14].

2.3.1 Likelihood function

One key element in model-dependent extraction of parameters is the likelihood function L . It measures the likelihood of observing x_i under the assumption of a probability density function (PDF), i.e. the model f , depending on a set of parameters \mathbf{p} . This can analytically be described as

$$L(\mathbf{p}) = \prod_{i=1}^n f(x_i; \mathbf{p}). \quad (2.10)$$

The PDF comes down to the expected rate, which shows at KATRIN naturally a statistical character because of the underlying radioactive decay. The corresponding function is a Poisson distribution which means that for every repetition of the measurement, one will receive a slightly different result which only allows the inference of parameters with uncertainty. Consequently, for a sufficiently high number of events ($\gtrsim 25$), the likelihood

function stated in Eq. (2.10) can be approximated as a product of Gaussian distributions for each event $N_{\text{obs},i}$ [Mac16; Kle14]:

$$L(N_{\text{obs},i}, N_{\text{theo},i}(\mathbf{p})) = \prod_{i=1}^n \frac{1}{\sigma_i \sqrt{2\pi}} \exp \left[-\frac{1}{2} \left(\frac{N_{\text{obs},i} - N_{\text{theo},i}(\mathbf{p})}{\sigma_i} \right)^2 \right]. \quad (2.11)$$

Here, the errors σ_i can be derived from Poisson statistics

$$\sigma_i = \sqrt{N_{\text{theo},i}(\mathbf{p})}. \quad (2.12)$$

Instead of maximizing the likelihood function it is computationally less intensive to minimize the χ^2 function

$$\chi^2 = -2 \log L = \sum_{i=1}^n \left(\frac{N_{\text{obs},i} - N_{\text{theo},i}(\mathbf{p})}{\sigma_i} \right)^2 \quad (2.13)$$

instead, which is known as Pearson's χ^2 -statistic (weighted least squares) [Pla83]. If the uncertainties σ_i are equal and fixed, their contribution leads to a constant factor, which can be neglected for minimization.

In the analysis of the krypton measurements, some parameters cannot be extracted from the fit due to small statistics. In this case, the pull method can be used, which is shortly introduced in the following.

Pull method

Finding the global minimum of Eq. (2.13) strongly depends on the used minimizer and the starting parameters. To save computation time, to prevent the fitter to converge into a local minimum and to increase the goodness of the fit, additional information about a parameter ψ can be used. This is achieved by penalizing strong deviations from the best estimated value $\hat{\psi}$, normalized by its uncertainty σ_ψ . Eq. (2.13) then can be extended by a so-called pull term to [Kle14]

$$\chi^2 = \sum_{i=1}^n \left(\frac{N_{\text{obs},i} - N_{\text{theo},i}(\mathbf{p})}{\sigma_i} \right)^2 + \left(\frac{\hat{\psi} - \psi}{\sigma_\psi} \right)^2 + \dots \quad (2.14)$$

This allows to account for systematic uncertainty or to constraint parameters which have small sensitivity in the fit. Also, the influence on the total result can directly be seen because of the direct influence on χ^2 [SM19].

On the contrary, this method is not applicable to all fit parameters. Especially not to the ones which only exist in discrete form, e.g. the energy loss function describing inelastic scattering [SM19].

2.3.2 Gaussian error interpretation

For a complete analysis, not only the obtained values are important, but also the description of their statistical and systematical uncertainty and how they contribute to the final result. The likelihood method also provides tools to determine systematical σ_{sys} and statistical (random) uncertainties σ_{stat} . In general, the statistical uncertainty $\sigma_{\text{stat},x}$ of a parameter x can be inferred by the derivative(s) around the minimum of the χ^2 function as a function of x [Lis17].

In the case of Gaussian distributed values, a method to describe the uncertainty is the standard deviation because it includes 68.27% of all measured values. Moreover, larger ranges of confidence can be calculated by multiplying σ with a constant factor, e.g. 2σ covers 95.45% and 3σ covers 99.73%.

A Poissonian distribution as a description of decay processes leads to a linear proportionality of the counts N to the total measuring time T_{tot} , transforming Eq. (2.12) to a statistical error

$$\sigma_{\text{stat}} \propto \frac{1}{\sqrt{T_{\text{tot}}}}. \quad (2.15)$$

In a complex setup like KATRIN, there are many systematic effects to consider which do not necessarily follow a Gaussian distribution, but due the central limit theorem, the quadratic sum of all individual effects (with their correlation) can be approximated by a Gaussian distribution with a defined error $\sigma_{\text{sys,tot}}$. Because systematical and statistical errors are uncorrelated by definition, one can derive the total uncertainty via [Mac16]

$$\sigma_{\text{tot}} = \sqrt{\sigma_{\text{stat}}^2 + \sigma_{\text{sys,tot}}^2}. \quad (2.16)$$

3. Plasma in the KATRIN tritium source

The KATRIN plasma provides the starting potential of the β -electrons. The determination of this plasma potential shape inside the WGTS, both radially and longitudinally, is essential to quantify the resulting systematic uncertainty for the neutrino mass measurements.

In this chapter, the cold low density KATRIN plasma is categorized and compared to other plasmas in nature (Sect. 3.1). General plasma properties are explained (Sect. 3.2) and the existing approach of simulating the special plasma in the KATRIN source is introduced (Sect. 3.4). At the end, the possibility of the krypton measurements for the investigation of the plasma is discussed (Sect. 3.5).

3.1 Categorization and comparison

The KATRIN source plasma properties are unusual compared to other types of plasmas in nature, which are shown in Fig. 3.1, regarding the following properties [Kuc16; Din05]:

- **Temperature:** The source temperature of $T_s \approx T_{\text{gas}} \approx T_{\text{ion}} = 30 \text{ K}$ is low, even for low temperature plasmas, which are characterized by a temperature of $\sim 10^4 \text{ K}$.

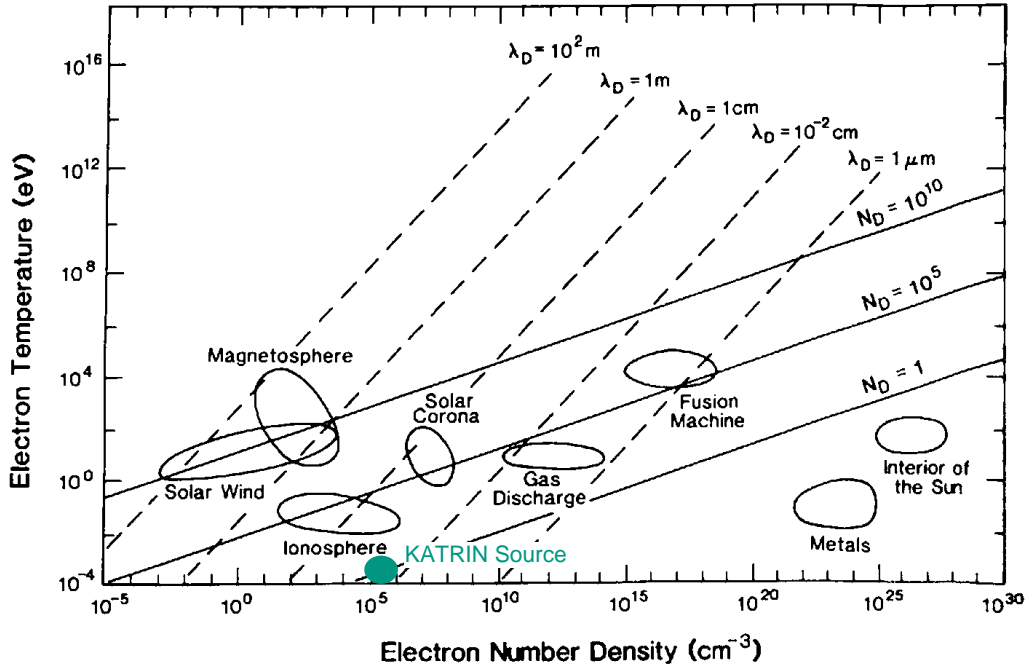


Figure 3.1: Electron temperature versus density of common plasmas in the universe, and KATRIN’s plasma. The corresponding values of $T_e = 2 \cdot 10^{-3} \text{ eV}$ and $n_e = 5 \cdot 10^5 \text{ cm}^{-3}$ place the KATRIN source plasma apart from other occurring plasmas in nature. Plot modified from [Gal12], inspired by [Kuc16].

- **Density:** The charged particle density of $10^{11...12} \text{ m}^{-3}$ is on the lower side of the possible plasma range of $10^{5...35} \text{ m}^{-3}$. The strong longitudinal gradient of the density within the WGTS from the center to the ends causes different gas flow regimes to evolve, as describes in Sect. 3.3.1.
- **Creation Process:** The dominant creation process is self-ionization caused by β -electrons and inelastic scattering on neutral gas¹. Each β -electron creates $\gtrsim 30$ secondary electrons and ions and cools down to thermal energies of $\sim 3 \text{ meV}$. The created ions are T^+ , He^+ , $^3\text{HeT}^+$, T_2^+ , and via chemical reactions and clustering effects even ions of higher order like T_3^+ or T_5^+ . The most frequent one are T_3^+ ions.
- **Spatial boundary:** The plasma is contained in a long tube of 10 m with a small diameter of only 9 cm and a rear wall with variable bias on one end. This creates in combination with strong longitudinal magnetic fields additional boundary effects and confinement. As a result, compared to ions, the mobility of electrons is higher longitudinally, but smaller transversally. Thus, electrons can leave the plasma to the rear wall and the ions to the beam tube walls. This process can be influenced by the rear wall voltage, which has a dominant influence in the radial center of the WGTS. At outer radii the potential is dominated by the beam tube.

Any change of an experimental setting which changes one of these properties directly leads to a change of plasma. Therefore, four elements strongly influence the plasma parameters and therefore its shape.

- The z -dependent gas density profile and its integrated value, the column density.
- The magnetic field.
- The temperature.
- The applied rear wall voltage.

In KNM2, the first three items were kept constant and different rear wall voltages were used to investigate the behavior of the source plasma potential, as discussed in Chap. 5.

However, to make statements about the plasma by interpreting the results, the general plasma properties and expected behavior are introduced in the following.

3.2 General plasma properties

To understand the plasma in the WGTS, the most important properties and effects are introduced in the following.

Debye shielding

If not marked otherwise, this paragraph is based on [Din05].

Plasmas are often defined by their “collective” behavior. This describes the preponderance of many-particle interactions instead of binary ones. If the distance of two charged particles changes, the Coulomb force causes other particles within the nearby regime of those particles to move collectively and “shield out” the Coulomb potential of the medium [Cal06]. This is called Debye shielding and is characterized by the the Debye shielding length scale λ_D

$$\lambda_D = \sqrt{\frac{\epsilon_0 k_B T}{ne^2}}. \quad (3.1)$$

¹Typical creation processes of other plasmas are high temperatures or large external fields.

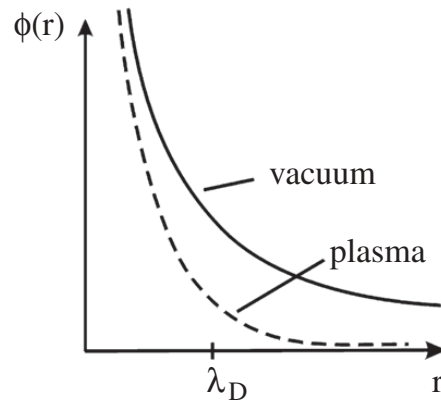


Figure 3.2: Potential distribution of an electric charge in vacuum and plasma. The plasma potential declines faster (in terms of distance) due to Debye shielding and converges to 0, describing the quasi-neutrality. Plot from [Din05] (modified).

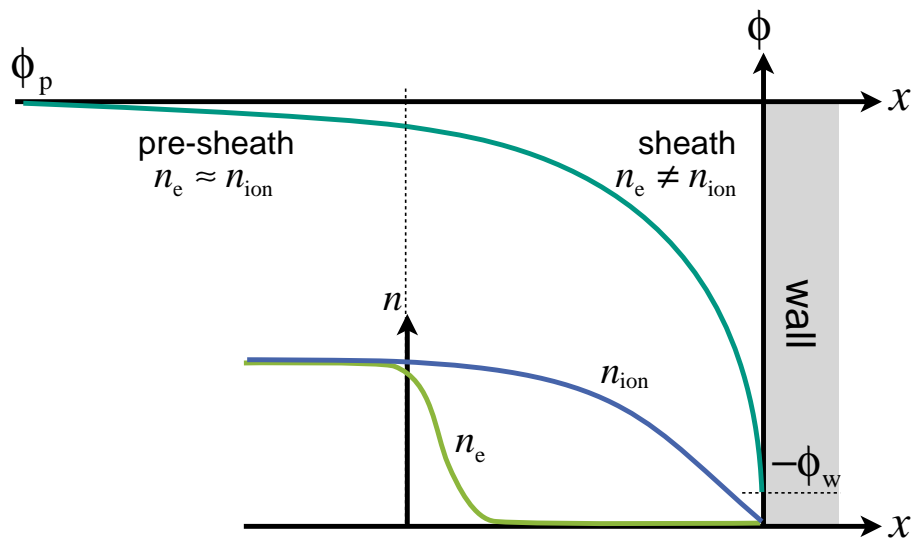


Figure 3.3: Plasma sheath model in 1D near a wall. There are three distinct regions to consider. The quasi-neutral plasma, the collisional quasi-neutral pre-sheath and the non-neutral sheath. Also, the charge densities for electrons and ions are shown. Figure from [MSL15] (modified).

Hereby, ϵ_0 is the vacuum permittivity, k_B the Boltzmann constant, T the temperature, n the particle density, and e the electric charge.

Perturbations of the charge distribution in the plasma typically fall off within λ_D .

Due to the screening effect of Debye shielding, plasmas appear to be neutral on the macroscopic scale $L \gg \lambda_D$ (Fig. 3.2). Confined by electromagnetic fields, charged particle ensembles can lack of this quasi-neutrality.

Plasma at boundaries

Boundaries or immersed probes drain the charged particles in a plasma by offering the possibility of recombination of electrons and ions at the surface [Hut03]. The boundary is on a negative potential with respect to the plasma potential ϕ_p because of the higher mobility of electrons compared to the ions ($\propto [m_i T_e / (m_e T_i)]^{1/2}$). This negatively charged surface gets shielded by a plasma sheath [TL29]. The potential of the sheath determines the charged particle transport between the surface and the plasma (Fig. 3.3). Further, the characteristic of the transition region between the plasma and the sheath can be described

with a pre-sheath [Din05].

The potential drop across the plasma sheath ϕ_w can be characterized by the so-called Bohm velocity [Din05]

$$v_{\text{Bohm}} = \sqrt{\frac{k_{\text{B}}T_{\text{e}}}{m_{\text{i}}}}, \quad (3.2)$$

in which m_{i} is the mass of the ion.

Frictional forces accelerate ions to the velocity v_{Bohm} , at which the ions enter the plasma sheath after falling through the potential drop in the pre-sheath of

$$\Delta\phi_{\text{Bohm}} = \frac{1}{2} \frac{k_{\text{B}}T_{\text{e}}}{e}. \quad (3.3)$$

The Bohm velocity v_{Bohm} and the potential drop $\Delta\phi_{\text{Bohm}}$ are connected via the so-called Bohm criterion [Fra76]

$$\frac{m_{\text{i}}}{2} v_{\text{Bohm}}^2 \geq \frac{1}{2} k_{\text{B}}T_{\text{e}}, \quad (3.4)$$

which pictures the minimal required kinetic energy of the ions to create the same flux as the electrons [Kuc16].

At the sheath boundary the quasi-neutrality relation $n_{\text{i}} \approx n_{\text{e}}$ holds and the potential drop across the plasma sheath is given by

$$\phi_w = \frac{k_{\text{B}}T_{\text{e}}}{4e} \ln \frac{2\pi m_{\text{e}}}{m_{\text{i}}}. \quad (3.5)$$

Using this formula at KATRIN source conditions in krypton mode (100 K), the plasma sheath potential at the rear wall can be approximated to

$$\phi_{\text{RW}} \simeq 17.00 \text{ mV}$$

using T_3^+ ions with $m_{\text{i}} = 9 \text{ u}$.

Work function

The surface potential depends on the Fermi level influenced by a bias potential and the work function ϕ . The latter can intuitively be defined as the energy needed to extract one electron from the Fermi level E_{F} to infinity E_{vac} (vacuum) [Lü10]

$$e\phi = E_{\text{vac}} - E_{\text{F}}. \quad (3.6)$$

In this case, E_{F} can be interpreted as the difference in energy for the ground state of the whole substrate for N and $N - 1$ electrons [WB35].

However, even on a clean metal surface in vacuum, the electron density “leaks out” from the rigid structure of positive ions forming a so-called dipole layer at the surface. Additionally, the possibility of chemisorption can cause a charge shifting towards or away from the adsorbed molecule, leading to change of $e\phi$. The same applies for physisorption which creates image charges by screening [Lü10].

Work functions, and especially their changes, play an important role in the analysis of potential systematics in the source. Hydrocarbonates at the rear wall or at the beam tube walls can cause radial and azimuthal potential dependencies.

3.3 Gas dynamics

As pointed out in Sect. 3.1, particle density distributions of electrons and ions are one major driver for the shape of the plasma.

At KATRIN, the tritium gas inside the WGTS forms a strong gradient from the center, where it gets injected, towards both ends, where it gets pumped out. The gas profile describes this gradient, depending on the injection pressure and the temperature. The gas profile cannot be determined by measurement and needs to be precisely modeled and simulated [Kuc16; Hoe12; KS10].

In krypton mode, the whole calculation must be repeated for the krypton gas, and interactions between both gases added. In this section, the most important findings to describe the gas profile in krypton mode are introduced, starting with the gas flow regimes and followed by the calculation of the mass flow rate and the effect of the different gas species.

3.3.1 Gas flow regimes in the WGTS and DPS

Because the tritium density inside the WGTS decreases over ~ 2 orders of magnitude from the center to the ends, the gas flow changes significantly. A suitable parameter to describe this change is the so-called rarefaction parameter δ . It is defined as [Kuc16]

$$\delta = \frac{d}{\lambda}, \quad \text{where} \quad \frac{1}{\lambda} = \frac{p}{\eta v_m}. \quad (3.7)$$

In these equations, d is the characteristic size of the system, i.e. the beam tube diameter, and λ is the mean free path. The latter can be calculated using the gas viscosity η , the pressure p , and the mean molecular velocity v_m . Then, three regimes can be defined, depending on δ [Kuc16].

$\delta \gg 1$: Hydrodynamic, continuum regime, description via continuum mechanics possible.

$\delta \ll 1$: Free molecular regime, intermolecular collisions are negligible.

$\delta \approx 1$: Transitional regime, neither continuum mechanics nor the neglect of collisions applies: **Solving of linearized Boltzmann equation is necessary.**

In the WGTS, under nominal conditions, there is mainly a hydrodynamic regime at the center, tending towards a transitional regime in the direction of DPS1, which is the reason for need of the linearized Boltzmann ansatz for the gas dynamics modeling of the source. At the beginning of DPS2, a free molecular regime can be assumed.

3.3.2 Calculation of the mass flow rate

To determine the gas and column density distributions, and their changes, one-dimensional gas flow calculations for the WGTS are needed. Reduction of the gas dynamics inside the WGTS to 1D applies sufficiently well, considering the size of the WGTS, a length of 10 m and a diameter of 9 cm.

The density profiles of krypton and tritium can be obtained via numerical integration from the following equation, which is derived in Sect. A.1

$$\dot{M} = \frac{\pi R^3}{v_m} \left[-G \frac{\delta_{\text{in}} - \delta_{\text{out}}}{L} + G_T(\delta) \frac{p}{T} \frac{dT}{dz} \right]. \quad (3.8)$$

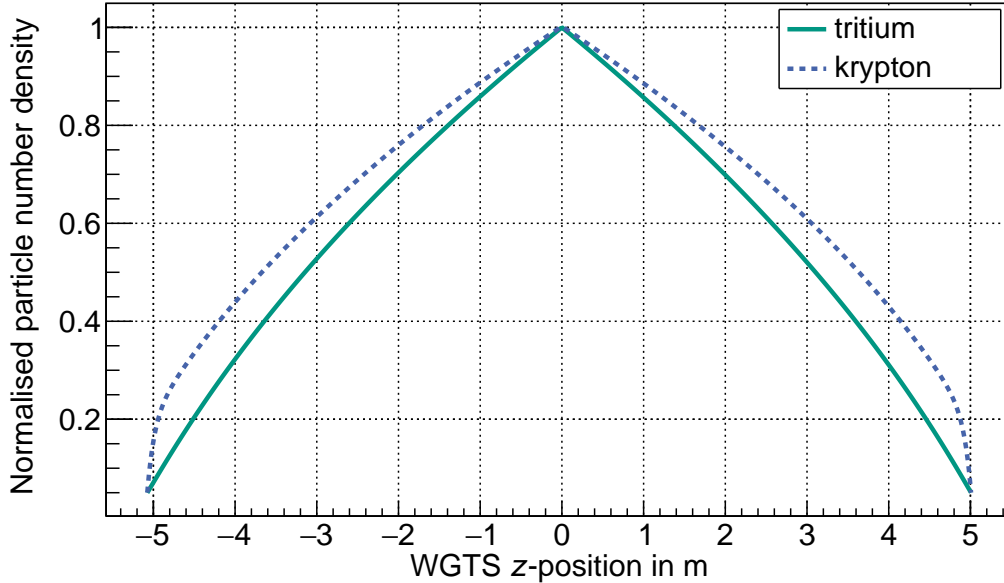


Figure 3.4: Gas density profiles for tritium and krypton at $T = 110$ K. Both are normalized to their maximum at the gas injection in the center of the WGTS ($z = 0$). They show a different shape, which leads to different starting potential distributions for both gases, due to different scatterings probabilities. Consequently, this needs to be considered in the transfer of krypton analysis results to tritium mode. Figure from [Mac16] (modified).

3.3.3 Calculation of throughput for tritium and krypton

The procedure of Sect. 3.3.2 must be repeated for krypton and extended, because interactions of different gases must be considered. This has been worked out by [KS10] and is summarized in the following.

Based on the derivation of the mass flow rate in Eq. (3.8), one can define a more generic dimensionless throughput J_α for species α , depending on the individual density gradients n_α, n_β

$$J_\alpha = -\frac{L}{n_{\text{in}}} \sqrt{\frac{m_{\text{m,in}}}{m}} \sum_{\beta} G_{\alpha\beta} \frac{n_\alpha}{n_\beta} \frac{dn_\beta}{dz}, \quad (3.9)$$

in which the suffix \square_{in} specifies the given parameter at injection, m_{m} is the mean molecular mass, depending on the concentration, and $G_{\alpha\beta}$ are the dimensionless gas flow rates for gas species α . The gas flow rate $G_{\alpha\beta}$ depends on the rarefaction δ and the individual density gradients of gas species β . Consequently, $G_{\alpha\alpha}$ corresponds to a single gas based on the kinetic Boltzmann equation.

The steps to calculate the total throughput with Eq. (3.9) can be divided into three stages [KS10]. First, the flow rate for tritium G_{11} gets integrated over δ to obtain the function $z = z(\delta)$ and hence the z -dependence of $\delta = \delta(z)$. Second, the krypton flow rates G_{21} and G_{22} are calculated based on the McCormack model [McC73], which assumes a hard sphere molecular model and the diffusive scattering on the tube wall. Third, by combining the results of the previous stages, one can calculate the density distribution of krypton by numerically integrating

$$J_2 = \frac{n_{1,\text{in}}}{L} = -G_{21}(z) \frac{n_2}{n_1} \frac{dn_1}{dz} - G_{22}(z) \frac{dn_2}{dz}, \quad (3.10)$$

which is the last step for solving Eq. (3.9). Note that the tritium gas flow, depending on the krypton density gradient G_{12} , is negligible. The reason for this is that the krypton concentration is several orders of magnitude lower than tritium ($\sim 10^6$).

The resulting density profiles from numerical integration of Eq. (3.10) in radial direction is constant down to an order of 10^{-5} [Mac16]. In z -direction on the other hand, it shows a significantly different shape compared to tritium as can be seen in Fig. 3.4. The different shapes can be explained by their different molecular masses, according to [Mac16]. The latter also provides further details regarding the implementation of the gas model in the software module `SSC` (introduced in Sect. 4.3.1).

3.4 Plasma potential simulation

Plasma measurements provide observables, which describe the plasma potential shape only in a limited manner, e.g. the integrated longitudinal potential profile. Plasma simulations on the other hand can calculate the plasma potential distribution and are therefore indispensable for the understanding of the precise plasma potential shape.

In the KATRIN collaboration, various model-based simulations have been developed, the most recent one which has provided results for plasma potential distribution is introduced in the following.

The development and implementation of a two-dimensional, i.e. axial symmetric, plasma model was conducted by [Kuc16], which was the basis for further sensitivity studies in [Mac16]. The latter also provides the framework on how to interpret the krypton measurements and to infer plasma properties (Sect. 4.4).

For the simulation, a time-dependent model was chosen because it allows to converge to the stationary solution via many iterations, whereas finding the initial conditions in a stationary approach that drives the simulation to convergence is difficult.

The first implementation assumed the electron energy distribution to be ideally Maxwellian with a fixed mean energy and a constant temperature. This was a reasonable assumption because the lower-energetic electrons were in fact Maxwellian and the high-energetic tail was neglected.

Further, the electron density distribution was approximated using the electron diffusion model, in which an important simplification was made. The used drift-diffusion equation only applies in the continuum regime and was therefore only simulated at the center of the WGTS and the rear wall was assumed to be at $z = -5$ m.

In the following step, ions and intrinsic electric field calculations, using the Poisson equation, were implemented. The three-particle fluid model was calculated for two dimensions, i.e. the planar plasma model.

Finally, the axial-symmetric model was created which considers the geometrical and field setting parameters at the center of the WGTS. The results for two different temperatures are shown in Fig. 3.5. A temperature of 30 K, at which neutrino mass measurements are recorded and at 110 K, close to the temperature of krypton measurements in KNM2.

With `KARL` and `ACRONYM` there is currently a new plasma simulation software framework in development. The major differences are a particle-in-cell approach and the covering of regions away from the center of the WGTS-C with molecular gas flow. However, detailed particle-in-cell simulations of the KATRIN source plasma are complex and have a high demand for computational resources ($\sim 10^6$ cpu · h)¹.

3.5 Experimental investigation with gaseous krypton

Due to the forming of a cold low density plasma, the starting potential of the electrons in the source is not constant, but changes both spatially and temporally. Local space charges and an induced change of the beam tube work functions result in potential inhomogeneities,

¹Internal communication with Jonas Kellerer.

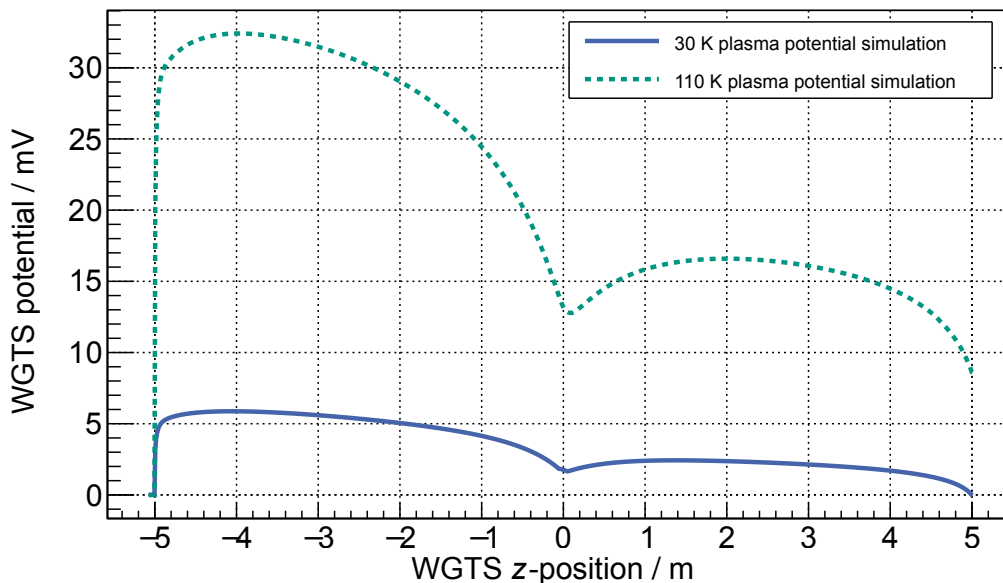


Figure 3.5: Simulated longitudinal plasma potential profile of the WGTS using the two-dimensional three-particle approach at both 110 K and 30 K. The total longitudinal differences are ~ 20 mV at 110 K and ~ 5 mV at 30 K. Plot from [Mac16] (modified) with data from [Kuc16].

fluctuations, and shifts. All lead to a systematic uncertainty in the measurement of the integrated spectrum and thus the neutrino mass analysis.

The determination of the longitudinal and radial shape of the plasma potential is crucial to approximate and optimize the systematic influence for the neutrino mass scans. Available methods for this task are the BIXS detectors [Rö15], high-rate measurements with PRO-KATRIN, the measurement of the WGTS currents depending on the rear wall voltage, and gaseous krypton¹ measurements.

The idea of using an additional gas as nuclear standard is to measure the electrons which leave the source carrying the information about spatial source starting potential. Further, with varying source conditions, the change of its characteristics can be investigated. Gaseous $^{83\text{m}}\text{Kr}$ was used for similar purposes in previous neutrino and dark matter experiments [Rob91; Bel+08].

At KATRIN, there are four requirements for such a gas:

- It must be possible to inject it into the WGTS at nominal source conditions (or at least close to), i.e. a temperature of ~ 30 K and a partial pressure of $\lesssim 3 \cdot 10^{-3}$ mbar. Otherwise, it cannot be assured that the results also hold for neutrino mass scans.
- It must not change the source conditions within or after the measurement, i.e. it must not change the plasma properties, and its residual activity must be negligible on a short time scale of days.
- Ideally, it produces monoenergetic electrons to be most sensitive to systematic effects and to allow calibration in the sub-eV range.
- The activity must be high to achieve high statistics within the limited time in systematic measurement phases.

Gaseous $^{83\text{m}}\text{Kr}$ is a good candidate to fulfill most of these requirements. It is gaseous down to ~ 100 K [Bel+08], has a half-life time of $T_{1/2} = 1.83$ h [McC15] and its parent nuclide in

¹There are two different krypton modes performed with KATRIN main spectrometer, gaseous and condensed $^{83\text{m}}\text{Kr}$. In this work only gaseous krypton source is described.

the decay chain rubidium-83 provides a specific activity of $> 3.7 \text{ GBq/g}$ [Rba]. Moreover, it offers different electron energy levels of $5 \text{ keV} - 32 \text{ keV}$ from internal conversion processes with different widths of $\simeq 1 \text{ eV}$.

The quasi-monoenergetic krypton electrons enable the determination of the radial plasma potential shape via the segmented FPD. The longitudinal profile on the other hand is challenging because the FPD is measuring an integrated count rate over z . An ansatz on how to exploit information about the longitudinal shape with krypton is the focus of the following chapter.

4. Modeling of the krypton mode

The electron spectroscopy with KATRIN relies on a precise knowledge of the electric potential difference between the starting potential in the source and the retarding potential in the analyzing plane of the spectrometer. The precise knowledge about the plasma potential shape in the WGTS is getting more important because the initially expected limit of the longitudinal source potential variation of 10 meV [Ang+05] might be exceeded.

Gaseous krypton provides a method to investigate the shape of the plasma potential in the WGTS, but also has some challenges in the realization.

Although $^{83\text{m}}\text{Kr}$ properties come close to the required ones, to perform such a measurement at KATRIN, different experimental settings must be used which are discussed in Sect. 4.1. Also, due to the electron creation by internal conversion, the measured krypton spectrum has a unique shape which is described in Sect. 4.2.

The details of the implementation of the krypton spectrum in the analysis software is explained in Sect. 4.3.

At the end of this chapter, the method how the krypton observables can be used to infer characteristic plasma properties are derived in Sect. 4.4.

4.1 Source and spectrometer settings in krypton mode

To have the most reliable comparison between systematic studies and neutrino mass measurements, the operational settings should be as close as possible to each other. This is not possible in every manner, which is discussed in the following.

Temperature

One the difference with large impact on the plasma is the different temperatures of the WGTS in both measuring modes. KATRIN was designed to operate at a source temperature of $T_{\text{WGTS}} = 30\text{ K}$ for the following reasons:

- Reduction of the broadening due to the doppler effect.
- Avoiding clustering of tritium molecules, which sets a lower limit of 27 K.
- Allowing a high column density, which is crucial for high activity at a given (limited) injection pressure.
- Reduction of the influence of the electron final state distributions.

The experience of other experiments has shown that krypton freezes out at temperatures below $\sim 110\text{ K}$ [Bel+08], depending on the partial pressure. The krypton measurements in KNM1 were successfully performed at $T_{\text{WGTS}} = 100\text{ K}$. This was therefore also the used temperature of the krypton measurements in KNM2.

The operational temperature of the WGTS cannot be set continuously. KATRIN uses a two phase cooling system which provides a technically feasible range of $\Delta T = 5\text{ K} - 7\text{ K}$ at the

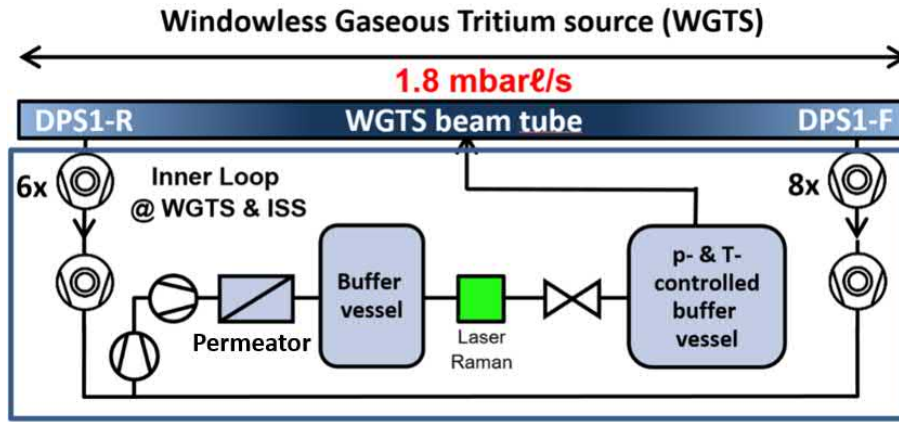


Figure 4.1: Loop operation in tritium mode. Gas gets injected at the center of the WGTS from the pressure controlled buffer vessel. The gas is leaving the source via multiple pumps at both ends of the WGTS. Further, the gas is guided through a permeator into a feed buffer vessel and through the laser Raman (LARA) cell back into the pressure stabilized buffer. Scheme from [Mar19] (modified).

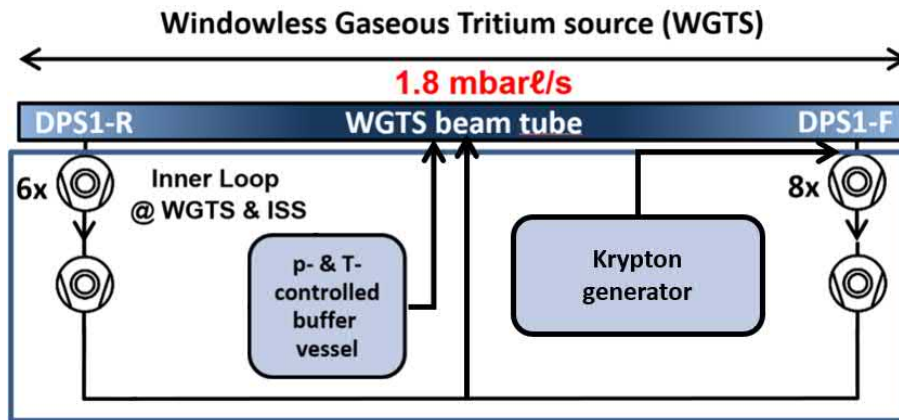


Figure 4.2: Loop operation in krypton mode. At the beginning of the circulation, a certain amount of tritium gets injected by the buffer vessel. After that, the krypton generator and the buffer vessel continuously inject krypton and tritium to compensate the lost gas to the DPS and the decayed krypton. Simultaneously, the pumps are circulating the gas by pumping it out from both ends and injecting it back at the center of the WGTS. Due to the krypton atoms, no permeators can be used to clean the source gas from hydrocarbons. Scheme from [Mar19] (modified).

characteristic temperature of a coolant. Possible temperature regimes depending on the coolant are 27 K – 33 K for neon, 80 K – 85 K for nitrogen, and 93 K – 100 K for argon. The temperature difference of 70 K between neutrino mass and krypton measurements makes it difficult to transfer the results from krypton measurements to the m_ν measurement conditions. This was one reason for the decision to perform both neutrino mass and krypton measurement at 80 K in KNM3.

Gas circulation and purity

There are three different modes of gas circulation in the KATRIN source, depending on the gas composition:

- Tritium (T)
- Krypton (T + Kr)
- Krypton only (Kr)

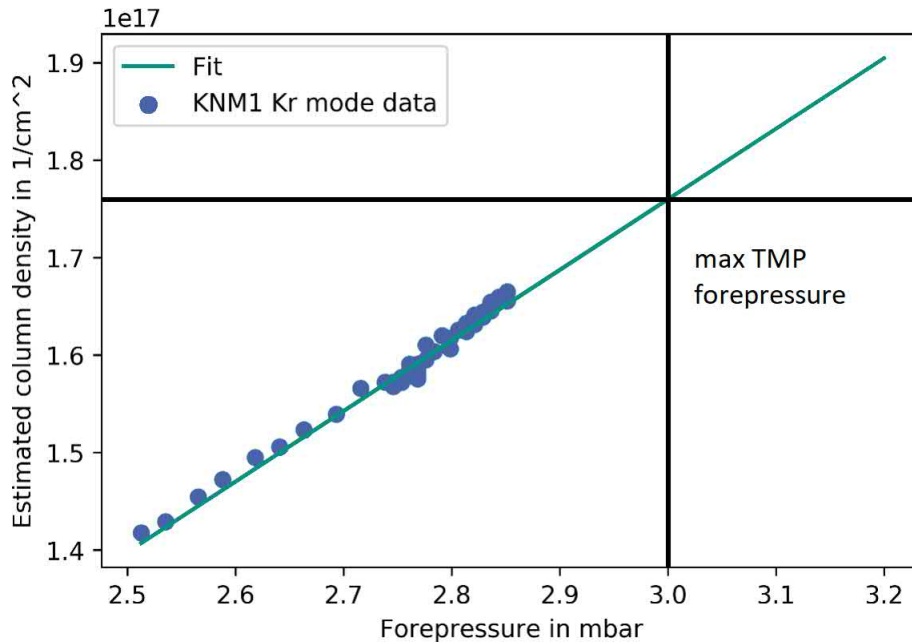


Figure 4.3: The maximum column density in krypton mode at 100 K is limited by the forepressure of WGTS TMPs and comes to $\rho d_{\max, \text{Kr}} \approx 1.8 \cdot 10^{21} \text{ m}^{-2} = 36 \% \text{ CD}_{\text{nominal}}^{-1}$. Plot from [Mar19] (modified).

The krypton only mode is used for reference measurements, because it is assumed to have negligible systematic effects from the plasma. The mode is realized by using the krypton mode without tritium injection and is therefore not explained separately.

The tritium circulation shown in Fig. 4.1 provides a continuous cleaning of the source gas by removing other gases with the permeator. This allows a stable operation in time. In krypton mode, the use of the permeator is not possible because it would also remove the krypton itself. Hence, this leads to a different procedure for gas injection and circulation as shown in Fig. 4.2. One consequence is that the tritium purity decreases in the order of $< 0.05 \%/\text{h}$ [Mar19] due to carbohydrates, created by materials in the TMPs which leak into the system. Additionally, the injection of both gases is performed differently which leads to an individual time dependent concentrations of krypton and tritium.

Independent of the different circulation methods, simulations show that the longitudinal gas density of krypton and tritium is significantly different which leads to different starting potential distributions for tritium and krypton due to the different scattering probabilities. This makes the transfer of the krypton results to tritium difficult as explained in detail in Sect. 3.3.

Column density

Particle density is one major factor for the plasma conditions. The maximum column density of tritium in krypton mode depends on the maximum flow rate of the gas injection, limited by the forepressure of the WGTS TMPs. Fig. 4.3 shows the relation between the forepressure and the resulting maximum column density of tritium. The value $\rho d_{\max, \text{Kr}} = 1.8 \cdot 10^{21} \text{ m}^{-2}$ corresponds to a maximal possible column density of $\sim 36 \%$.

Field setting in the main spectrometer

Equally to the beta scan measurements, the common offset of the inner electrodes (IE) is set to -200 V and the steep cone offset to 130 V [Rod18].

The tritium endpoint at $\sim 18.57 \text{ keV}$ is below the krypton L_3 position at $\sim 30.472 \text{ keV}$.

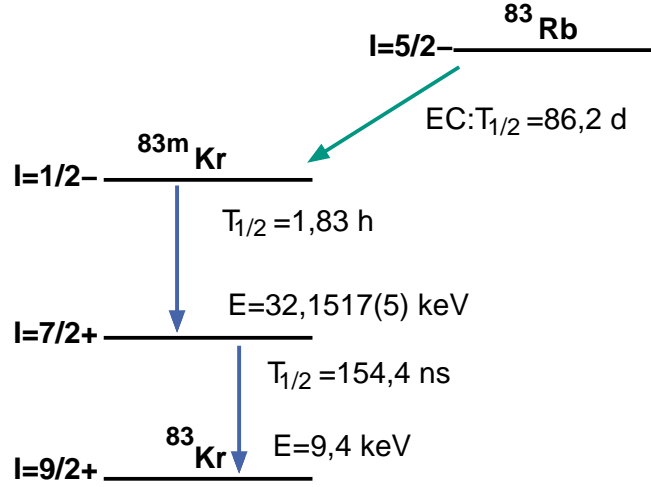


Figure 4.4: Decay scheme of $^{83\text{m}}\text{Kr}$ from its mother isotope ^{83}Rb . $^{83\text{m}}\text{Kr}$ is created by electron capture of ^{83}Rb which leads to an excited state which decays into the ground state in two steps. Quantum number I describes the angular momentum and α the conversion coefficient of each state. Figure from [Ost08] (modified).

Thus, using the 6 G field setting of the neutrino mass measurements would downgrade the possible MAC-E filter sensitivity. Consequently, the field setting is scaled to higher energies, which allow a lower magnetic field strength in the analyzing plane. The currents for the coils of the extended low field compensation system (eLFCS) are optimized for the krypton measurements via simulation to the so-called 2.7 G setting. The exact values can be found in Tab. A.5. To crosscheck the 2.7 G field setting with the simulation, one can compare the values of the three magnetic field (Bartington) sensors which are attached to the main spectrometer vessel. As a result, the simulated values 2.0 G, 3.2 G and 1.5 G (south, center, north) are within $\lesssim 0.1$ G in agreement with the measured values of 1.9 G, 3.1 G and 1.5 G.

4.2 Krypton spectrum

In contrast to the electrons from the beta decay of tritium which produce a continuous spectrum, $^{83\text{m}}\text{Kr}$ offers several quasi-monoenergetic electrons of finite intrinsic line width from internal conversion processes (IC). Internal conversion is a radioactive decay which takes place if the probability of γ -emission of excited states is small. This can be the case due to a complex configuration of the nucleons or small excitation energies. Then, the nucleus transfers its excitation energy to an electron on an inner shell, mainly K and L , but also M and N . Depending on the shell, different energy levels (lines) of electrons are created. For naming, the lines of each shell get numerated, e.g. L_3 is the third line of L shell electrons.

Internal conversion is getting more likely for atoms with high nucleon counts because this leads to inner shells which are closer to the nucleus. As a consequence, a better energy transfer from the nucleus to a shell-electrons is possible. Because this is not a particle decay, the mass number A , nucleon number Z , and therefore also the neutron number N of the atom is conserved, but the mass defect of the nucleus increases. Due to energy conservation, the electron energy E_e corresponds to the mass defect of the nucleus E_γ reduced by the binding energy of the electron $E_{\text{bind},e}$, yielding

$$E_e = E_\gamma - E_{\text{bind},e}. \quad (4.1)$$

Because $E_{\text{bind},e}$ is different for each shell, there are several sharp spectral lines in the energy spectrum of conversion electrons instead of continuous ones as shown in Fig. 4.5. The

Table 4.1: Energies of conversion electron spectral lines of $^{83\text{m}}\text{Kr}$ for the decay from the state $I = 1/2^-$ to $I = 7/2^+$ (Fig. 4.4). The total de-excitation energy is $E \simeq 32.152$ keV. The currently best values for the line energies are provided by using a combination of different methods namely optical, photoelectron, electron impact and absorption spectroscopy, combination of X-ray, photoelectron data (or absorption data), and compilation [Vén+18]. If available, the values for the line width Γ are used from [Ost08], otherwise from [CP01]. All other values are used from [Vén+18].

Line	Energy / eV	Γ / eV	α_{theo}	Intensity per decay / %
K	17824.2(5)	2.70(6)	478.0(50)	24.8(5)
L_1	30226.8(9)	3.75(93)	31.7(3)	1.56(2)
L_2	30419.5(5)	1.165(69)	492.0(50)	24.3(3)
L_3	30472.2(5)	1.108(13)	766.0(77)	37.8(5)
M_1	31858.7(6)	3.5(4)	5.19(5)	0.249(4)
M_2	31929.3(5)	1.230(61)	83.7(8)	4.02(6)
M_3	31936.9(5)	1.322(18)	130.0(13)	6.24(9)
M_4	32056.4(5)	0.07(2)	1.31(1)	0.0628(9)
M_5	32057.6(5)	0.07(2)	1.84(2)	0.0884(12)
N_1	32123.9(5)	—	0.643(6)	0.0255(4)
N_2	32136.7(5)	—	7.54(8)	0.300(4)
N_3	32137.4(5)	—	11.5(1)	0.457(6)

corresponding decay scheme can be found in Fig. 4.4. The energy levels are characteristic for the nuclide. Among the decay via IC, γ -emission is also a valid process to de-excite the mother nuclide [Kri19]. The ratio of the possibilities for each process is called conversion coefficient α . It is specific for each shell and can experimentally be determined by measuring

$$\alpha_i = \frac{\dot{N}_{i,e}}{\dot{N}_{i,\gamma}}, \quad i \in \{K, L, M, N\}, \quad (4.2)$$

in which $\dot{N}_{i,e}$, $\dot{N}_{i,\gamma}$ are the rate of emitted conversion electrons and photons of shell i . Conversion coefficients are important for the modeling of an IC spectrum because they specify the contribution of each line with its intensity. The exact values for the line positions and conversion coefficients are shown in Tab. 4.1.

In this thesis, only the transition from the state $I = 1/2^-$ to $I = 7/2^+$ with a de-excitation energy of $E \simeq 32.152$ keV plays a role, because the transition $I = 7/2^+$ to $I = 9/2^+$ with a de-excitation energy of $E \simeq 9.4$ keV is deep inside the tritium spectrum and would complicate any analysis. Therefore, all lines are named without the transition suffix, e.g. L_3 is assumed to be $L_3 - 32$.

4.2.1 Shake up/off effect

When an atom de-excites via emission of a conversion electron, the potential distribution of the atom changes quickly and the electrons in the shell rearrange, leading to so-called shake up/off effects. Shake up describes the excitation of a shell electron to a bound state with higher binding energy and shake off the de-excitation into the continuum. The probabilities for these processes are not negligible [Arm+85] and produce satellite lines in the spectrum [KCD68]. The excitation energy reduces the energy of the emitted conversion electron accordingly to the discrete binding energies. With continuous contributions from the shake off process, the satellite line is placed at ~ 20 eV (in case of L_3) lower energy than the primary line [War+91; Mac16] (Fig. 4.5).

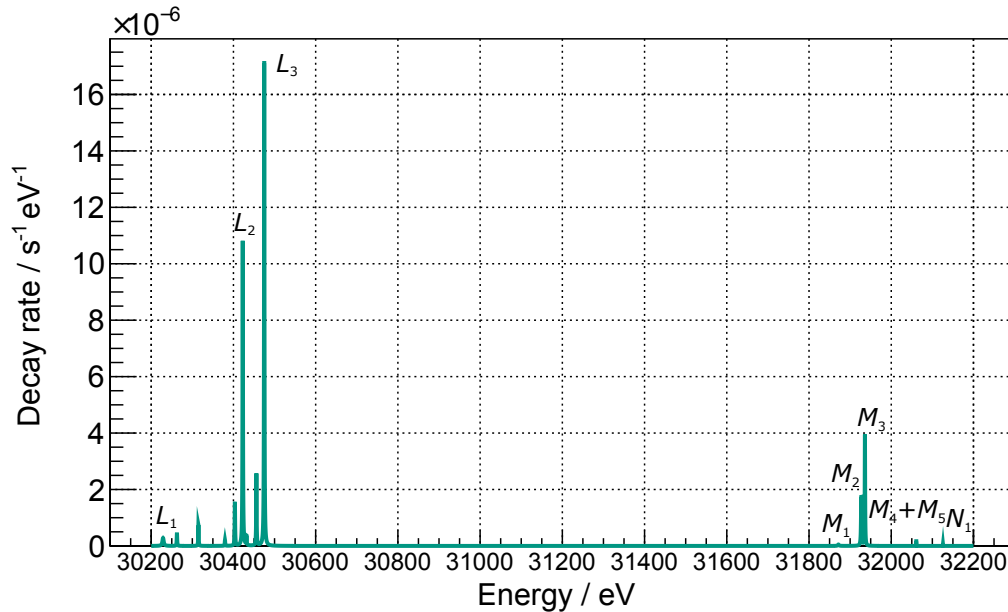


Figure 4.5: Internal conversion lines of $^{83\text{m}}\text{Kr}$ for a selection of different shells, along with their corresponding shake up/off lines. The higher lines from M and N shells show significantly less intensity compared to $L_{2,3}$. Plot from [Mac16] (modified).

The main analysis in this work is done at the primary line of L_3 and the first scattering peak, $\bar{\epsilon} \approx 12.8 \text{ eV}$ below. For this reason, the modeling of the satellite lines with the different probabilities for every shell is not necessary [Hua10]. Nevertheless, shake up/off effects matter in the analysis because they reduce the yield of the primary line.

4.2.2 Voigt profile

Quasi-monoenergetic electrons from krypton imply that at least some lines do not have the shape of a perfect δ -function. According to Heisenberg's uncertainty principle, the lifetime of an excited state τ leads to some uncertainty on electron energy E , quantified by the width

$$\Gamma_e = \frac{\hbar}{\tau}, \quad (4.3)$$

in which \hbar is the reduced Planck's constant. The natural shape of the line can be derived by solving the time dependent Schrödinger's equation, which leads to a Lorentz profile

$$L(E, E_e, \Gamma_e) = \frac{dN}{dE} = A \cdot \frac{\Gamma_e}{2\pi} \cdot \frac{1}{(E - E_e)^2 + \Gamma_e^2/4}. \quad (4.4)$$

In this equation, E represents the energy of the electron and E_e the line position [WW30; Hua10].

To consider systematics of (approximately) Gaussian distributions, the line can be convolved with a Gaussian

$$G(\Delta E, \sigma^2) = \frac{1}{\sqrt{2\pi\sigma^2}} e^{-\frac{\Delta E^2}{2\sigma^2}}. \quad (4.5)$$

Here, ΔE is defined as $\Delta E = E - E_e$ and σ is the standard deviation. The observed line shape can consequently be described as a convolution of both Lorentz (Eq. (4.4)) and Gauss (Eq. (4.5)) distributions, forming a so-called Voigt profile

$$V(E, E_e, \sigma^2, \Gamma_e) = \int_{-\infty}^{\infty} G(E', \sigma^2) L(E - E', E_e, \Gamma_e) dE'. \quad (4.6)$$

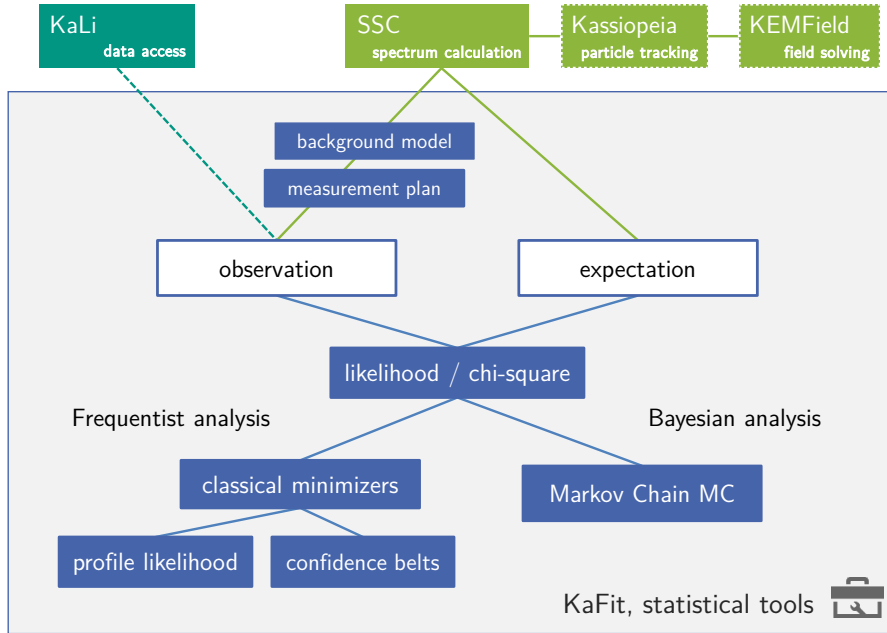


Figure 4.6: Basic scheme of the KaFit software module, showing the different analysis methods and the connection to other modules. Figure from [Kle14] (modified).

If both widths of Gauss $\Gamma_G = \sqrt{8 \ln(2)}\sigma$ and Lorentz Γ_e are known, the resulting total width of the Voigt profile can be approximated via [OL77]

$$\Gamma_V \approx 0.5346 \Gamma_G + \sqrt{0.2166 \Gamma_e^2 + \Gamma_G^2}. \quad (4.7)$$

4.3 Spectrum modeling

To infer any information about the plasma, the shape of the measured $^{83\text{m}}\text{Kr}$ spectrum must be fitted and the relevant parameters extracted. Thus, a model is needed which has the possibility to explain the observed count rate N_{obs} with a calculated rate N_{theo} , i.e. what to expect from the measurement. Then, Eq. (2.13) can be used to state how good the model represents the data, given the fitted parameters. It follows that it is not possible to see any effects which have not been specifically implemented in the model. Ultimately, a sophisticated model of the spectrum considering all experiment-specific parameters is necessary. The better the model fits to the data, the better can the different values of interests be extracted. On the other hand, it is also important to choose the number of free model parameters wisely based on physical assumptions to save computational time, to minimize correlations, and not to overfit the data.

All krypton spectrum fits in this work have been performed with the KATRIN software package `KASPER` (Sect. 4.3.1) which allows the complex modeling of N_{theo} .

The different features of the krypton spectrum which allow to determine the relevant plasma observables have been implemented in the modules `KaFit` and `SSC`, and are described in Sect. 4.4.

4.3.1 Software framework

For fitting detector data, in the KATRIN collaboration are several equivalent software frameworks available, e.g. `KaFit`, `Fitrium` or `Samak`. In terms of krypton analysis, `KaFit` already provides an implementation of the krypton source spectrum which was implemented by [Mac16] and is the reason for using `KaFit` in this work.

`KaFit` is part of the `KASPER` framework, a unified analysis and simulation package (for illustration see Fig. A.1). `KASPER` is written in C++ and uses existing established libraries like `CMake`, `Doxygen`, `boost` and `ROOT`. All (sub)modules are implemented as independent classes, making them both generally accessible and extendable [Kle14].

The module `KaFit` realizes statistical methods, which are described in Sect. 2.3, allowing the investigation of different measurement strategies with their systematic impact and the parameter inference, e.g. the neutrino mass. It covers both, Bayesian approaches, with Markov Chain methods used as minimizer, and frequentist strategies with classical minimizers like Minuit. An illustration of the different modules is shown in Fig. 4.6.

A key role in `KaFit` for the source spectrum calculation plays the submodule `SSC`. It allows the pixel-wise calculation of the \dot{N}_{theo} considering the response function, a spatially dependent source model, and differential spectra for tritium and krypton. The source model includes individual density profiles for each of these gases. The response function comprises physical processes which influence the electron energy during the transport from the source to the main spectrometer, for instance the transmission function, energy loss via inelastic scattering inside the WGTS, or the doppler effect. Considering radially dependent distributions is crucial to make use of the segmented focal plane detector. This is achieved by the individual calculation of cells inside the WGTS, the so-called voxels. Thereby, relative x and y coordinates of the fluxtube are simply given by the position of the pixels on the the FPD and the z coordinate depends on the number of horizontal slices of the WGTS which are summed up to calculate the integral spectrum of a certain pixel [Mac16].

4.4 $^{83\text{m}}\text{Kr}$ observables

To infer information about the plasma from krypton measurements, the measured electron rate with the FPD is compared with the expected rate given the retarding potential of the main spectrometer, using the optimization of free fit parameters. Then, these fitted parameters can be used for quantification and mitigation of the source systematics in neutrino mass scans.

Source systematics can be derived from krypton measurements with two complementary approaches.

- Use of the spectrum parameters (Voigt profile) itself.
- Exploitation of inelastic scattering to derive an additional information about the longitudinal shape of the plasma potential.

Both methods make no assumptions of the expected plasma potential shape and focus on obtaining longitudinal information of the WGTS plasma, because the radial and azimuthal dependence can be resolved by the segmented FPD. The details on how each approach interprets its parameters in terms of plasma systematics are explained in the following.

In Sect. 4.4.3 their different dependence on the column density is explained and the parametrization of the impact on the neutrino mass discussed.

4.4.1 Voigt model

The parameters of a fitted integrated krypton spectrum line are given by the Voigt profile (Sect. 4.2.2). This includes the position of the main line $E_{\text{main},0}$, the amplitude, and the total width of the main line, composed of the intrinsic line width Γ and the Gaussian broadening σ_0 . The contributions of lines of higher energy produce a background rate, which is considered by a constant offset¹. An example is shown in Fig. 4.7.

¹Due to non-adiabatic transmission of electrons with large surplus energies the background rate shows a slope and a constant approximation of this slope introduces a systematic effect on the $^{83\text{m}}\text{Kr}$ observables.

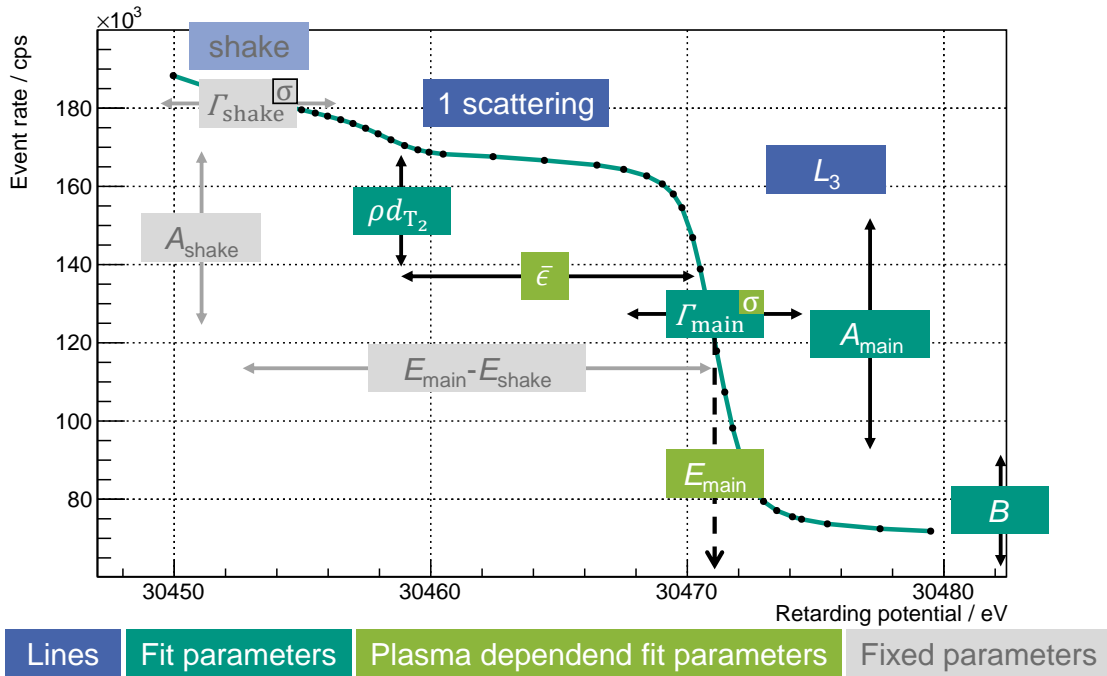


Figure 4.7: Krypton spectrum observables. The idea is to investigate the change of the L_3 main line parameters under different WGTS conditions. The main line has the Voigt parameters position E_{main} , amplitude A_{main} and intrinsic width Γ_{main} which may get broadened depending on the plasma inhomogeneities and instabilities by $\sigma = \sigma_0$. Due to lines of higher energy, there is also a background rate B . Due to inelastic scattering, a scattering peak is $\bar{\epsilon}$ below the main line. Here, $\bar{\epsilon}$ is the mean of the energy loss function. In the scattering model, Δ_{10} can be used to measure differences in the longitudinal plasma potential of front and rear part of the WGTS. The tritium column density can be fitted as well due to the strong dependence of inelastic scattering on the gas density. The shake line does not contribute any information to infer plasma related parameters, but need to be considered because of its vicinity to the main line.

The subset of fit parameters which are influenced by the plasma potential V are in first order the line position $E_{\text{main},0}(V) = E_{\text{main,ref}} + e\langle V \rangle_0$ and in second order the Gaussian line broadening $\sigma_0^2(V)$. The energy $E_{\text{main,ref}}$ corresponds to the line position if there is no plasma present. In the case of a different source potential caused by the plasma, the position of the main line (as shown in Fig. 4.7) would be shifted. In the case of a varying shape, the measured line width in the integrated spectrum would experience an additional broadening.

The observed line position $E_{\text{main},0}(V)$ and line broadening $\sigma_0^2(V)$ only include unscattered electrons, which are more likely to originate from the front part of the WGTS than from the rear. This indicates the limitations of this method. The potential of the rear part of the WGTS could be changed, e.g. by the influence of the rear wall and the observed line position $E_{\text{main},0}(V)$ would not be different. However, scattered electrons are more likely to be created in the rear part of the WGTS which is used in scattering method to obtain information about the longitudinal plasma potential in the rear part compared to the front. This is explained in detail in the next section.

4.4.2 Scattering model

[Mac16] investigated how well the krypton measurements would be able fit the expected longitudinal plasma potential shape (Fig. 3.5). As a conclusion, the different plasma potentials could not be distinguished with the line broadening only because the integrated spectrum does not provide any information about the longitudinal plasma potential profile

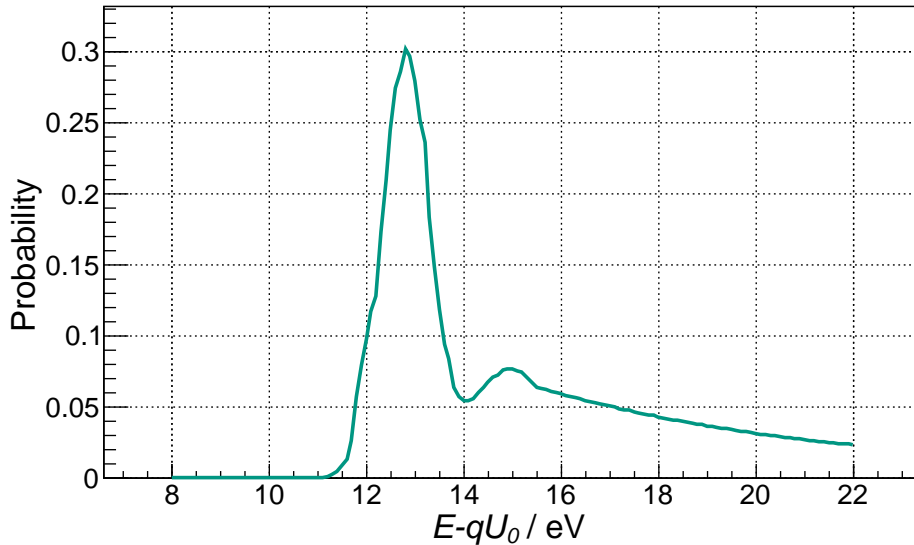


Figure 4.8: Energy loss function for singly-scattered electrons, which was determined experimentally under the usage of the rear section e-gun at 18 keV. The energy loss function, as a reference value for Δ_{10} , was not yet measured at 30 keV and makes it a possible source of systematic uncertainty in krypton measurements (Sect. 5.1.3). Plot made with `KaFit`.

itself. Thus, the deviation of the difference between the mean energy for unscattered and singly-scattered electrons from the mean energy loss, the so-called energy loss shift is introduced. This allows to obtain two more parameters than with the Voigt method only. Basic principle from [Mac19] is as follows.

Electrons from the main line appear at lower energies because of energy loss due to inelastic scattering inside the source. The energy loss function ϵ_{loss} describes the probability of a certain energy loss, if an electron scatters. With a known ϵ_{loss} and no plasma present, the expected additional peak can be calculated precisely. The ϵ_{loss} function is experimentally determined under the usage of the electron gun (e-gun) in the rear section. The result is shown in Fig. 4.8. It's shape is asymmetric with a steep increase before and a flat tail after the maximum value at $\bar{\epsilon} \approx 12$ eV. Further reading can be found in [Deb19].

The probability of an electron P_i , created at axial position z and initial angle θ , to scatter i times strongly increases with the gas column density ρd and is described by a Poissonian distribution [Ase+00]

$$P_i(z, \theta) = \frac{(\rho'(z, \theta) \cdot \sigma_{\text{tot}})^i}{i!} \exp[-\rho'(z, \theta) \cdot \sigma_{\text{tot}}], \quad (4.8)$$

where the partially integrated density $\rho'(z, \theta)$ is defined as [Mac16]

$$\rho'(z, \theta) = \frac{1}{\cos \theta} \int_z^{L_{\text{WGTS}}/2} \rho(z') dz'. \quad (4.9)$$

The resulting $P_i(z, \theta)$, up to $i = 2$, are shown in Fig. 4.9. As a result, the different average axial creation positions \bar{z}_i of an electron which scatters i times are not constant. In other words, unscattered electrons are likely to come from the front part of the WGTS, whereas scattered electrons are more likely to come from the rear part, the more often they have scattered. In the measured spectrum, the different peaks for the i th scattering are separated and their position

$$E_{\text{main},i} = E_{\text{main},0} - i \cdot \bar{\epsilon} + \Delta_{10} \quad (4.10)$$

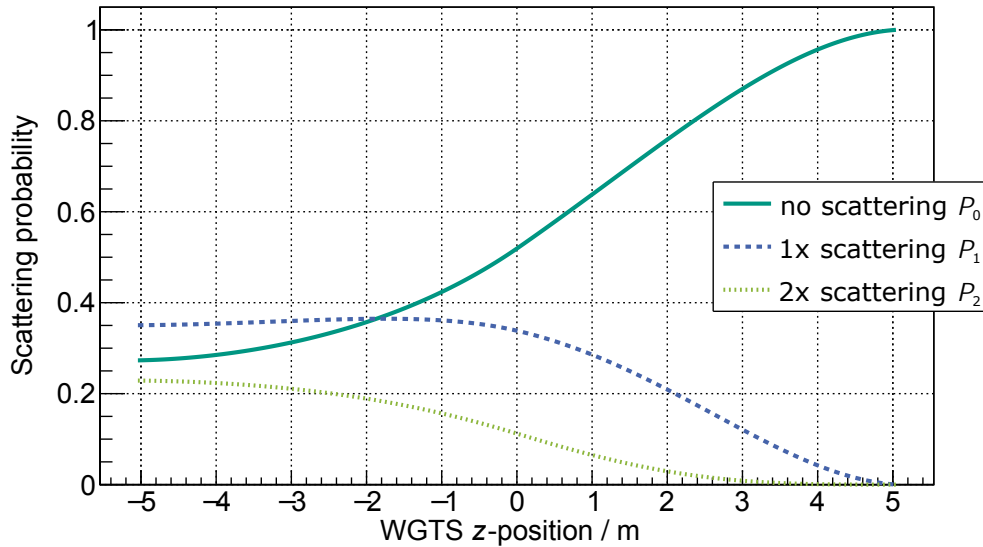


Figure 4.9: Scattering probabilities as a function of the axial position of creation at nominal column density of $\rho d = 5 \cdot 10^{21} \text{ m}^{-2}$. Plot from [Mac16] (modified).

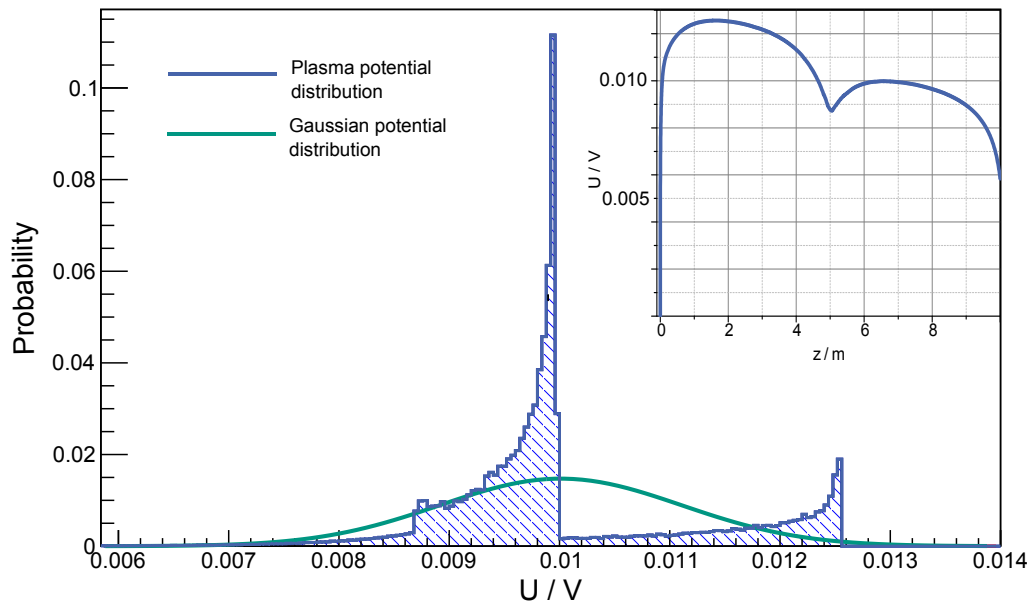


Figure 4.10: Starting potential distribution of unscattered electrons created in the simulated plasma potential, shown on the top right. A Gaussian fit as first and second estimators is included as well. Plot from [Kuc16] (modified).

can be fitted individually. $E_{\text{main},0}$ is the observed main line position for zero scattering, $\bar{\epsilon}$ is the mean energy loss for one scattering process¹ and Δ_{10} is the difference between the start potentials of zero and i -time scattered electrons. At nominal column density, the longitudinal shape can sufficiently well be described by only using the peak for singly- and unscattered electrons.

One possibility to get an easier access to the plasma potential from the obtained spectrum is to use the so-called starting potential distribution (SPD), instead of the potential profile [Mac16]. The former considers all z -dependent functions as a scalar average.

¹In `KaFit`, a convolution of the whole energy loss function is used instead of the mean energy loss only.

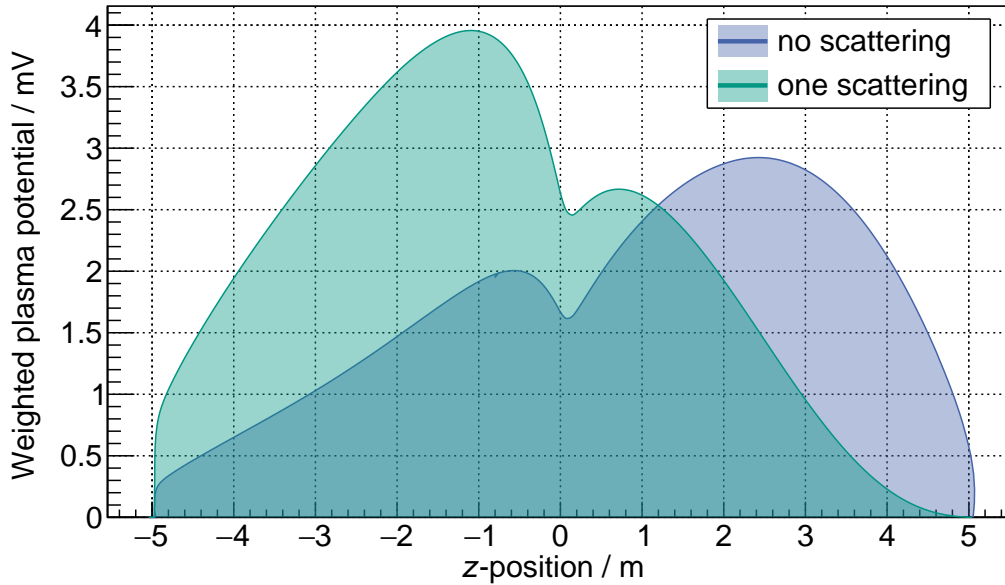


Figure 4.11: Weighted plasma potential for zero and singly-scattered electrons in krypton mode. It represents the integrand in Eq. (4.11) and therefore considers the maximum acceptance angle, the gas profile, the scattering probabilities, and the simulated plasma potential shape at 110 K from Fig. 3.5. Plot from [Mac16] (modified).

The first order estimate for the SPD values $\langle V \rangle_i$ for i times scattered electrons is given by the axial integration of the weighted plasma potential

$$\langle V \rangle_i = \frac{\int_z dz \theta_{\max} N_{\text{Kr;T}} P_i(z) V(z)}{\int_z dz \theta_{\max}(z) N_{\text{Kr;T}} P_i(z)}. \quad (4.11)$$

and the second order via $\text{Var}(\langle V \rangle_i)$. Here, θ_{\max} represents the maximum acceptance angle and $N_{\text{Kr;T}}$ the gas density profile for krypton and tritium. The illustration of the integrated function is shown in Fig. 4.11 for up to $i = 1$. This allows to obtain a distribution which depends on the scattering count i , not z . Thus, any translation to $V(z)$ is model dependent. The SPD for unscattered ($i = 0$) electrons is shown in Fig. 4.10. The Gaussian fit is justified because non-Gaussian distributed systematic contributions are approximated in second order by their first two moments and higher orders are comparatively small [Mac19; Sle15].

First order estimate of the start potential: Line position shift

The access for the leading order of the SPD is provided by measuring only the spectrum of singly- and unscattered electrons. Hence, one can define the shifting of the energy loss function as the starting potential differences for zero and singly-scattered electrons

$$\Delta_{10} = \langle V \rangle_1 - \langle V \rangle_0, \quad (4.12)$$

as visualized in Fig. 4.12. The total spectrum shift is given by $\langle V \rangle_0$

$$E_{\text{main},0} = E_{\text{main,ref}} + e\langle V \rangle_0. \quad (4.13)$$

This allows to neglect all more frequent scatterings for the determination of the main line position to derive $\langle V \rangle_0$.

On the other hand, there are two notable dependencies on external parameters, which introduce systematic effects. First, the inference of $\langle V \rangle_0$ from $E_{\text{main},0}$ depends on a

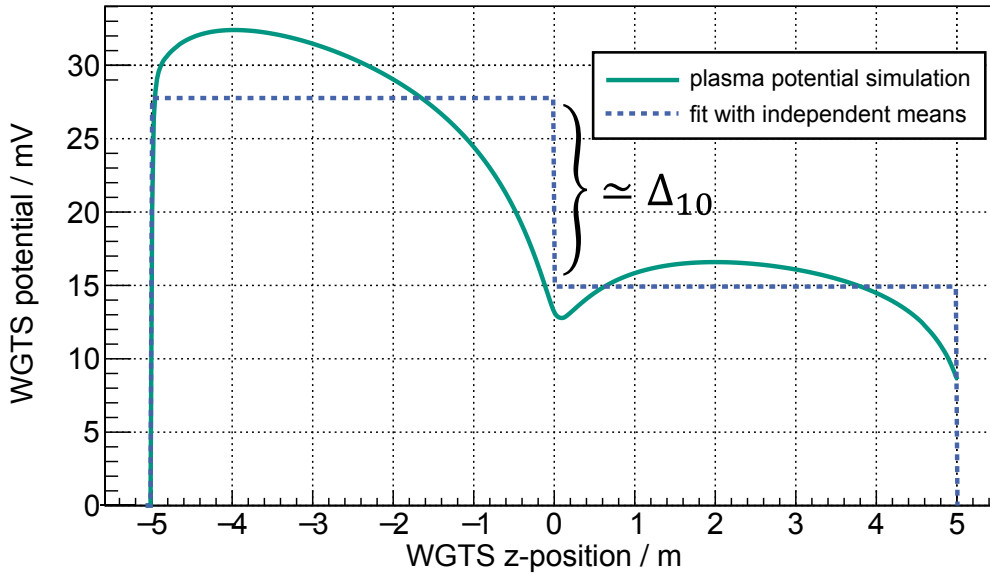


Figure 4.12: Rectangular approximation of simulated plasma model comparable to scattering model approach. The differently scattered electrons only see two different potential means, according to their different probability of longitudinal origin shown in Fig. 4.9. Plot from [Mac16] (modified).

dedicated reference measurement for $E_{\text{main,ref}}$ and may depend on other systematic effects, e.g. work function changes. Second, the calculation of Δ_{10} as a measure of $\langle V \rangle_1$ is given by

$$\Delta_{10} = \frac{1}{e} (E_{\text{main},1} - E_{\text{main},0} + \bar{\epsilon}) , \quad (4.14)$$

as indicated by Eq. (4.10). It depends on the energy loss function *epsilon* which was precisely measured at 18 keV, but cannot be determined for L_3 position energies of ~ 30 keV¹. Thus, the absolute values of the fitted Δ_{10} must be used carefully because they have a systematic uncertainty. For instance, an obtained positive value for Δ_{10} must not necessarily mean that $\langle V \rangle_1 > \langle V \rangle_0$ holds, it could also be the other way around with an overestimated $\bar{\epsilon}$. Therefore, Δ_{10} is more conclusive if used in comparison to different rings or rear wall voltages.

Nevertheless, [Mac20] introduces a method based on data self-consistency which leads to a estimation for ϵ_{loss} at 30 keV via a correction of ϵ_{loss} measured at 18 keV by adding 90 meV. Consequently, the shown Δ_{10} parameters in this work are corrected by this value. Although this brings the scale of the absolute values in a more reasonable region with a zero-crossing around $U_{\text{RW}} \approx 0$ V depending on the rear wall voltage. Nonetheless, it cannot replace the energy loss function measurement at ~ 30 keV.

Second order estimate of the start potential: Line broadening

The second order of the SPD is the variance $\sigma_i(V)$ of the mean starting potential for a i times scattered electron

$$\sigma_i(V) = \sqrt{\langle V^2 \rangle_i - \langle V \rangle_i^2} . \quad (4.15)$$

To simplify the fits, only the zero scattering broadening σ_0 is fitted, which is identical to the Voigt model broadening. It should be noted that σ_0 does not only describe a non-constant plasma potential, but would also absorb other inhomogeneities, for instance temporal fluctuations within the beam line. Thus, the observed line broadening is composed of

$$\sigma_{0,\text{obs}} = \sqrt{\sigma_0^2 + \sigma_{\text{fluct}}^2} . \quad (4.16)$$

¹The operation of an e-gun which is capable of creating electrons with such high energies is planned.

One access to σ_{fluct} is a reference measurement, but the likewise necessary reference measurement of the intrinsic line width is not available.

4.4.3 Column density dependence and comparison

As pointed out, the Voigt and the scattering models are complementary for the estimation of the starting potential distribution. They depend on the column density of tritium, but their sensitivity scales oppositely.

The Voigt parameter estimate of σ_0 only considers unscattered electrons for which holds, the smaller the column density, the smaller is the probability of scattering. Thus, more electrons in a given period contribute to the main line in the measured spectrum. Also, the statistics of unscattered electrons which are created in the rear part of the WGTS, and starting at the rear part plasma potential, increases.

The scattering model on the other hand makes use of the additional scattering peak, which is more dominant with higher column density, but lacks the reference value of ϵ_{loss} .

Given the above, is it recommended to use both models together to achieve the best possible sensitivity on the plasma estimates in the given measuring time.

Also, because of the strong column density dependence of the scattering probabilities P_i , defined in Eq. (4.8), the amplitude of the scattering peaks can be used to determine the amount of molecules in the source, i.e. the gas column density.

4.4.4 Impact on the neutrino mass

The goal of performing measurements with $^{83\text{m}}\text{Kr}$ is the quantification and, if possible, mitigation of plasma-related systematic effects to the neutrino mass measurements. The mitigation could be achieved by the determination of a rear wall voltage which minimizes the longitudinal inhomogeneity of the source potential.

The systematic uncertainty caused by the electron final state distribution (FSD) of the β -decay in direct neutrino mass measurements with tritium was derived in [RK88]

$$\Delta m_{\nu}^2 = -2\sigma^2. \quad (4.17)$$

Although σ^2 indicates a Gaussian width of a given uncertainty, this equation also holds for other distributions up to second order approximation [Sle15].

The observables for the longitudinal plasma potential shape are Δ_{10} and σ_0 . In this case Eq. (4.17) gets modified to [Mac20]

$$\Delta m_{\nu}^2(\sigma_{0,\text{obs}}^2, \Delta_{10}) = -2\sigma_{0,\text{obs}}^2 - \epsilon_{\Delta}\Delta_{10}. \quad (4.18)$$

Here, $\sigma_{0,\text{obs}}$ is the observed line broadening due to plasma potential inhomogeneities and other fluctuations and ϵ_{Δ} is a phenomenologically absolute energy scale, which depends on the column density and the measurement time distribution. Thus, all parameters must be determined at the same measurement conditions. This includes the demand for reproducibility and temporal proximity.

Given the above, the use of Eq. (4.18) without translation is not possible for KNM2 because the neutrino mass and krypton measurements were performed at different column densities and temperature.

However, in order use the simplified estimation of Eq. (4.17), krypton measurements must be performed nevertheless because it is not possible to extract a line broadening value from the continuous spectrum of tritium. The analysis of the performed krypton measurements within KNM2 is discussed in the following.

5. Analysis of KNM2 krypton campaign

As motivated in Sect. 3.5, performing krypton measurements for systematics studies is indispensable and has been done along with every measurement campaign. The analysis of these krypton measurements is a sophisticated task in which many peoples are involved, leading to continuously new findings at a short time scale of weeks. One example is the simulation of the so-called background slope (Sect. 5.1.3) which can explain many radial effects but was not available at the time of performing the analysis in this work.

In this chapter, the analysis of the krypton measurements within the second neutrino mass measuring campaign KNM2 is discussed, starting with the general methodology (Sect. 5.1) and followed by a comprehensive analysis of the krypton observables (Sect. 5.2-Sect. 5.9).

5.1 General methodology

The main goal of krypton measurements is the quantification of plasma properties and the resulting systematic uncertainty on the neutrino mass. Thus, all observables of the krypton measurements themselves, which allow drawing conclusions about the plasma, must be significant regarding both systematics and statistics.

The systematical uncertainty of the krypton measurements is given by the experimental setup in $^{83\text{m}}\text{Kr}$ -mode. The influence of the main systematic sources are comparable to beta-scans, and with 0.32 eV^2 [Ake+19] on the m_ν^2 small. However, because some operational settings are different, a short qualitative description of the existing systematical effects is given in Sect. 5.1.3.

The statistical uncertainty is the dominating one compared to systematics for most of the observables, although the quantification of the influence of some systematic effects are still under investigation, e.g. the background slope. Therefore, all analysis of the KNM2 krypton measurements will only consider statistical errors, if not explicitly described otherwise.

The whole KNM2 krypton campaign, comprising 201 individual runs of the L_3 line at various rear wall voltages, took ~ 1 week. The details of the measurement and fitting procedure are explained as follows.

5.1.1 Measurement procedure

The krypton measurements are performed like the neutrino mass scans. Nevertheless, in doing so, there are different ways and possible settings, given the experimental setup. One must distinguish between settings which stay (mostly) the same for the whole campaign, i.e. operational settings (Sect. 4.1), and those which are changed between or within runs. Changing settings comprises the retarding potential to measure the integrated spectrum, the rear wall voltage, and whether the CERMAX lamp is turned on.

The operational settings are set once at the beginning of the krypton campaign and then only checked for stability. The changing parameters can, thanks to the high level

of automatization at KATRIN, mostly be adjusted by a script, iterating the following procedure.

First, one must decide whether the CERMAX lamp should be turned on. Second, the rear wall voltage U_{RW} for which the spectrum scan shall be performed must be set. Third, performing an integrated measurement of the krypton spectrum by processing a list of retarding potentials and their corresponding duration times.

In KNM1, the CERMAX lamp did not show any significant improvements concerning the plasma-induced source potential inhomogeneity on the time scale of one spectrum scan. Thus, the CERMAX was only turned on for one set of measurements.

Also, in KNM1 it was difficult to draw a conclusion about rear wall dependencies of the plasma given the short assigned time. In KNM2, many more scans at different rear wall voltages and repetitions of them could be performed. The Focus was to cover the region around the so-called good coupling regime and some larger absolute voltages. In the good coupling regime, the overall plasma potential follows the externally applied potential of the rear wall and inhomogeneities are minimized. At the time of planning, the good coupling regime was assumed to be $-0.5 \text{ V} \lesssim U_{\text{RW}} \lesssim 0.5 \text{ V}$. For the large values, voltages up to $\pm 5 \text{ V}$ were chosen. A complete run list can be found in Tab. A.1.

The continuous measurement of a set of rear wall voltages is called sweep. In total, 11 sweeps were performed (Tab. A.3).

A spectrum was measured step-wise with 41 potential values for one scan direction. This has shown in KNM1 to be a good compromise between more potential values allowing to resolve significant features of the krypton spectrum and less potential values because setting them takes time and the analysis needs more computational resources to calculate the model.

The potential values are distributed within a $\sim 30 \text{ V}$ range. The exact values can be found in Sect. A.2.

For setting one retarding potential value, the advanced post regulation [Rod18] was used which took $\sim 15 \text{ s}^1$. After 40 s of measuring time in histogram mode, the next retarding potential value was set. Additionally, before each scan, the rate at a retarding potential value of $\sim 30 \text{ kV}$ was measured for 60 s to monitor the longtime stability within KNM2 krypton.

Because one upwards and one downwards scan were performed right after each other, the total measuring time for one rear wall voltage T adds up to

$$T \approx 60 \text{ s} + 2 \times 41 \times (15 + 40) \text{ s} = 4570 \text{ s} = 1 \text{ h } 16 \text{ min} . \quad (5.1)$$

5.1.2 Fitting procedure

The obtained fit parameters strongly dependent on the model and slightly on the fitting algorithm itself. For best comparability, not only within all fits performed in this thesis, but also with other krypton fitters in the KATRIN collaboration, the same configuration of the fit is used. The different parameters are configured as follows.

- **Mode:** Pixel-wise, one fit for each pixel of each run. Every stacking is performed afterwards as described in Sect. 5.1.2.1.
- **Error:** All displayed errors show statistical uncertainty only. A qualitative description of systematic effects is given in Sect. 5.1.3. For the parameters L_3 line position and energy loss shift Δ_{10} , the more accurate Minos error [Jam98] is used. The single fit error for the squared line broadening σ_0^2 can not be determined every time. Because

¹Setting a retarding potential value for the first time needs more time because there are no existing parameters available which could be used as initial values for the regulation.

the error of one fit does not depend on the run or pixel, a conservative constant of 0.02 eV^2 is generally chosen, motivated by the fits which have successfully constructed the Minos error.

- **Pixel selection:** KNM2 pixel selection (117 pixels)
- **Pile-up correction:** On
- **Energy loss:** On
- **Synchrotron:** On
- **Detailed Transmission:** Off
- **Initial WGTS slicing:** 100
- **Gas dynamics:** Complex gas dynamics model from Eq. (3.10) is used¹.

5.1.2.1 Fit result stacking

The FPD provides individual count rates for each pixel. To make use of this individual information, every spectrum scan is fitted pixel-wise. However, depending on the analysis, it can be necessary to combine individual fit results, for example to gain more statistics by combining multiple scans or to perform ring-wise analysis by combining pixels. In this case, the individual fit results x_i with their uncertainty σ_i are combined by using a weighted mean

$$\bar{x} = \frac{\sum_i w_i x_i}{\sum_i w_i}, \quad (5.2)$$

in which $w_i = \frac{1}{\sigma_i^2}$ correspond to the individual weights. This procedure makes it easy to calculate the standard error

$$\sigma_{\bar{x}} = \sqrt{\frac{1}{\sum_i w_i}} \quad (5.3)$$

of the weighted mean.

5.1.2.2 Line width error propagation

The krypton observables for the line width of the Voigt profile are the Gaussian width σ_0^2 and the Lorentz width Γ^2 . Even so, in some cases it is more intuitive, and better comparable to other quantities, to use σ_0 and Γ instead. Using the propagation of uncertainty, these values and their corresponding standard error can be calculated via

$$x = \sqrt{x^2} \quad \text{and} \quad \sigma_x = \left| \frac{\partial \sqrt{x^2}}{\partial x^2} \right| \sigma_{x^2} = \left| \frac{1}{2x} \right| \sigma_{x^2}, \quad \text{for } x^2 \in \{\sigma_0^2, \Gamma^2\}. \quad (5.4)$$

5.1.3 Systematical uncertainties

It should be noted that some systematic effects, additional to the one induced by the source plasma, contribute to the observed Gaussian broadening. Because the Gaussian broadening is a free parameter in the fitting of the spectrum, some systematic effects are also covered, at least to some extent. However, it is important to distinguish the different effects and their contribution to $\sigma_{0,\text{obs}}$ to transfer the values for the systematic effects, which are also present in tritium mode, to the neutrino mass analysis.

A sophisticated quantification of systematic effects as it exists for tritium mode does not exist yet. However, possible contributions to systematic uncertainties in krypton mode, many of which are still under further investigation, are the following.

¹This is one main driver for the long fitting time of up to 6 h for one pixel-wise fit on 1 cpu core compared to ~ 30 s without (KNM2 krypton campaign contains $201 \text{ run} \cdot 117 \text{ fit/run} \cdot 6 \text{ cpu} \cdot \text{h/fit} = 23517 \text{ fit} \cdot 6 \text{ cpu} \cdot \text{h/fit} \approx 140 \cdot 10^3 \text{ cpu} \cdot \text{h}$).

Period summary files

The interpretation of the count rate are performed pixel-wise. This means that electrons of each pixel follow a different path through the spectrometer and therefore see different magnetic and electric fields in the analyzing plane. To correct for this, the values get corrected by a Monte Carlo simulation of the field setting, stored in the so-called period summary file.

To quantify the scale of this possible uncertainty by a flux tube offset, one can compare the values of the center pixel and shift it by 2 mm, which is a reasonable scale as showed in Sect. 5.9.1. The result is a difference of the magnetic field in the analyzing plane $\Delta B_{\text{ana}} \lesssim 400$ nT and of the electric potential $\Delta U_{\text{ana}} \lesssim 30$ mV [Beh20].

Pixel dependent MAC-E filter resolution

According to Eq. (2.4), the energy resolution of the MAC-E filter depends mainly on the magnetic field setting. Thus, different magnetic fields in the analyzing plane could lead to a different energy resolution of each pixel. The largest difference of the magnetic field in the analyzing plane is between ring 0 and 4. Using Eq. (2.4) to calculate the energy resolution at the L_3 line position results in

$$\left. \begin{array}{l} \text{Ring 0: } \Delta E = 30472 \text{ eV} \frac{2.68 \text{ G}}{4.232 \text{ T}} = 1.93 \text{ eV} \\ \text{Ring 4: } \Delta E = 30472 \text{ eV} \frac{2.64 \text{ G}}{4.238 \text{ T}} = 1.90 \text{ eV} \end{array} \right\} \Rightarrow 30 \text{ meV difference.} \quad (5.5)$$

Background uniformity

As described in Sect. 4.4, the fitted background rate is a constant covering the tails from lines of higher energy. Admittedly, this is only an approximation because the closer the lines are to the measured one, the larger is their non-constant contribution. On the other hand, tests of fitting this non-constant background only lead to a minimal change in the order of \sim mV for the line broadening. Moreover, this only holds for the L_3 -line scans, line $N_{2,3}$ are of highest energy and see no additional background.

Even so, the L_3 shake line, which is close to the main line, is separately considered in the model.

However, the major effect from the background is given by the non-adiabaticity.

Background non-adiabaticity

Analyzing pixel-wise background shows the effect of $\sim 3\times$ higher background count rates on inner rings of the FPD than on outer ones. This can be explained by non-adiabatic transmission on outer radii of electrons with large surplus energy, as the ones created from lines of higher energy M_{1-5} and N_{1-3} . In this case, the electrons change their trajectory and falsify the results by creating a non-zero slope of the background. Because every fitted parameter shows a radial dependence, this is likely to be a large systematic which is further investigated in Sect. 5.9.1.1, but not yet explicitly considered in the fitting of the krypton spectrum.

Lorentzian reference

The largest systematic effect for the line broadening is the reference value for the intrinsic line width. Both add up non-linearly, according to Eq. (4.7), to the total measured total line width of the Voigt profile. This results in both shifting and scaling of the line broadening parameter, depending on the reference line width. This is illustrated in Fig. A.4.

Fitting both parameters at the same time without a pull term restriction does not work well due to large correlation between these parameters. Thus, the value must be determined separately. The value which was determined by the KNM1 reference measurement in krypton only mode shows the tendency to be (too) large, because it leads to negative line broadening values. This is discussed in Sect. 5.2 and Sect. 5.3.

Detector effects

Even though all pixels have the same size, they do not necessarily share the same sensitivity. Correction for pile-up is performed, but additional radial dependencies due to backscattering or other effects are not excluded yet. Also, the current energy calibration does not fulfill the requirements yet and needs to be improved.

Krypton column density drift

Due to the half-life time of krypton’s parent nuclide $^{83\text{m}}\text{Rb}$ of ~ 86 d, the total krypton activity decreases by $\sim 5\%$ within the measurement time of ~ 6 d. As a result, the krypton observables experience “tailwind” or “headwind” depending on the scan direction with regard to the retarding potential. To counteract this dependence, a spectrum scan is performed in both directions, up and down, one behind the other. This allows averaging both values afterwards for an “effective” value. Nonetheless, it is a possible source of systematic effects and further investigated in Sect. 5.7.

Gas column density drift

Like the krypton column density drift, the gas column density, which mainly consists of tritium, also shows a drift of $\sim 2.4\%$ in 6 d of krypton mode measurements. This affects directly the plasma potential itself, because it depends on the column density. Because it is not clear how large the influence of this effect is on the krypton observables, it is further investigated in Sect. 5.7.

5.2 KNM1 reference measurements

The main focus of this thesis is the analysis of the KNM2 krypton campaign in the end of 2019. Nevertheless, similar measurements were recorded before in May 2019 during the KNM1 krypton campaign. Although the KNM1 krypton results are less extensive, the comparison of certain analysis is informative. Especially the reference measurement for the intrinsic line position and the line width, i.e. krypton only, was only performed in KNM1. However, there is a possibility to extract the line width value from KMN2 data by including the $N_{2,3}$ line (Sect. 5.3).

For the KNM1 reference measurement, the rear wall voltage was set to $U_{\text{RW}} = -150$ mV. It is not expected that this U_{RW} affects the observed line width parameters in any way because there is no tritium inside the source. As a consequence, the charged particle density is low and thus no plasma expected, to which the rear wall could couple¹.

In total, six runs were performed and the detailed run list can be found in Tab. A.4.

Line Width

The fitted histogram of the intrinsic line width is shown in Fig. 5.1. It determines the reference value to

$$\Gamma_{\text{L}3}^{\text{ref}} = (1.070 \pm 0.064) \text{ eV} . \quad (5.6)$$

It is to mention that the mean single error of one pixel-wise fit $\overline{\Delta x}$ is smaller than the fitted standard error $\sigma = \sigma_{\text{hist}}$. This indicates a systematic

$$\sigma_{\text{sys}} = \sqrt{\sigma_{\text{hist}}^2 - \overline{\Delta x}^2} = 14.08 \text{ meV} , \quad (5.7)$$

which was not considered before. One possible candidate for this additional broadening is a radial dependence of the line width as it can also be seen in Fig. 5.4. A decrease of

¹This has been validated within the KNM3 krypton measurements.

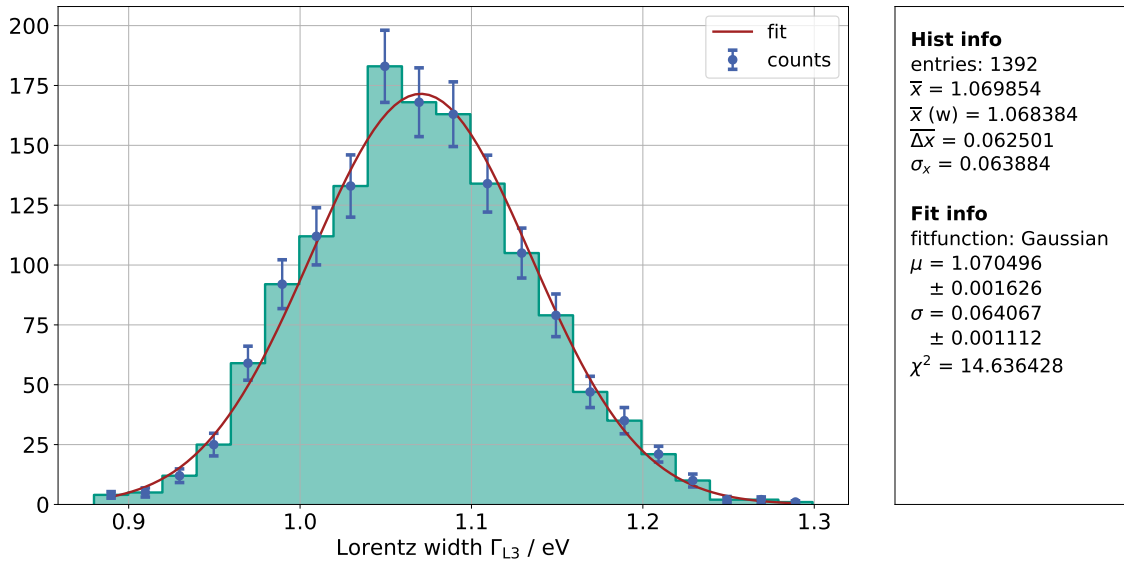


Figure 5.1: KNM1 reference value for the intrinsic line width determined in krypton only configuration of the source. The values in the hist info box refer to the single entries, i.e. 1392 in total. \bar{x} is the mean value, $\bar{x}(w)$ weighted with their uncertainty, σ_x the standard error and $\overline{\Delta x}$ is the average single value error. The parameter in fit info correspond to the Gaussian fit parameters after creating the weighted histogram.

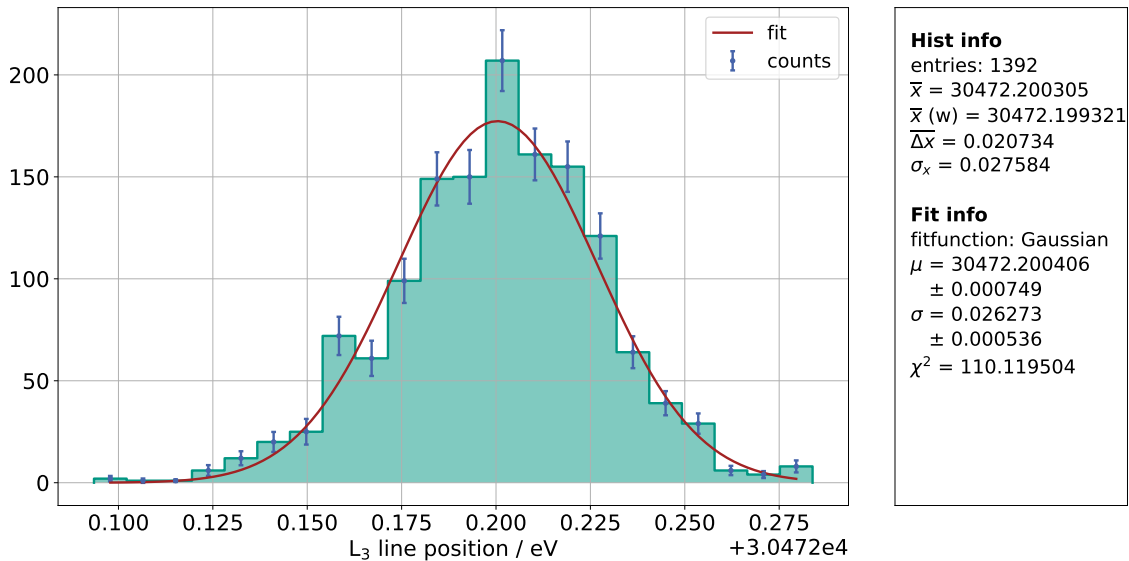


Figure 5.2: KNM1 reference value for the L_3 line position determined in krypton only configuration of the source. The values in the hist info box refer to the single entries, i.e. 1392 in total. Parameter \bar{x} is the mean fitted line position, $\bar{x}(w)$ the mean weighted with the individual single value errors, σ_x the standard error and $\overline{\Delta x}$ is the average single value error. The parameter in fit info correspond to the Gaussian fit parameters of the weighted histogram.

the width towards outer radii indicates that the center sees a different, larger broadening. Because the gas density is low, inhomogeneities of the beam tube work function could lead to this effect. However, this effect also appears in the most recent analysis of the KNM3 reference measurements which favor a non-constant background as cause of this radial effect.

Line position

The fitted histogram in Fig. 5.2 of the line position shows a Gaussian distribution around the mean value of

$$E_{\text{main}}^{\text{ref}} = (30472.200 \pm 0.026) \text{ eV}. \quad (5.8)$$

Like the line width, the mean single error $\overline{\Delta x}$ is ~ 5.5 meV smaller than the fitted Gaussian width of the histogram. This introduced a systematic contribution of

$$\sigma_{\text{sys}} = \sqrt{\sigma_{\text{hist}}^2 - \overline{\Delta x}^2} = 16.14 \text{ meV}, \quad (5.9)$$

which can be explained by the radial effect shown in Fig. A.2. However, because the radial difference is visible even without tritium in the source, the same explanation as for the line width holds, non-constant background and work function inhomogeneities.

5.3 Intrinsic line width determination with $N_{2,3}$ method

The obtained reference value for the intrinsic line width Γ_{L_3} from KNM1 seems to be too large, because it leads to a negative line broadening values and shows strong systematic effects. Thus, the measurement of the $N_{2,3}$ lines in KNM2 can be used to obtain an intrinsic line width indirectly. Inasmuch as the $N_{2,3}$ lines themselves have vanishing intrinsic lines width they can be used to constraint the line broadening in the L_3 line fits.

The major disadvantage of measuring the $N_{2,3}$ is statistics. The observed rate is $\sim 60\times$ smaller and the sensitivity on the line broadening per run $\sim 8\times$ worse compared to the L_3 line measurement. However, because the lines have no background from higher lines, there are no non-adiabaticity effects which would introduce systematic effects.

Given the above, the analysis of the $N_{2,3}$ lines provide a good opportunity to crosscheck the L_3 reference measurements.

General idea and configuration

The determination of the intrinsic line width Γ of the L_3 line with the $N_{2,3}$ method requires two major steps. First, the line broadening σ_0^2 is fitted in the $N_{2,3}$ measurements. Second, the obtained result is used to constraint the line broadening and fit the intrinsic line width Γ of the L_3 line measurements.

As can be seen in Tab. 4.1, the $N_{2,3}$ lines are created by electrons from the outermost shell and are therefore assumed to have vanishing intrinsic line widths [Vén+18]. However, there is a theoretical consideration which sets a general lower limit on the width to $\Gamma_{\text{min}} = 30$ meV [CP01]. Thus, both values are tested.

Because the $N_{2,3}$ measurement took place in usual krypton mode right within the L_3 measurements, the plasma induced line broadening σ_0 is assumed to be the same. This σ_0 can then be included as pull term parameter in the regular L_3 line measurements to fit the intrinsic line width Γ . Additionally, the fit range of the $N_{2,3}$ must be restricted to the part of unscattered electrons because the N_1 line overlaps with the line of singly-scattered electrons at $\sim E_{\text{main},N_{2,3}} - 12$ eV (Tab. 4.1).

The $N_{2,3}$ lines were only measured once at one rear wall voltage of $U_{\text{RW}} = 0.2$ V (Tab. A.2). For this reason, only the L_3 line measurements at the same U_{RW} should be used to fit the intrinsic line width.

For the first step, two delta functions must be included in the model. Fortunately, this can be achieved by using the Lorentzian part f of the Voigt profile with vanishing width. It follows a representation of a delta function [Mur06]

$$\lim_{\Gamma \rightarrow 0} f(E, E_{\text{line}}, \Gamma) = \lim_{\Gamma \rightarrow 0} \frac{1}{\pi} \frac{\Gamma}{(E - E_{\text{line}})^2 + \Gamma^2} \quad (5.10)$$

$$= \delta(E - E_{\text{line}}). \quad (5.11)$$

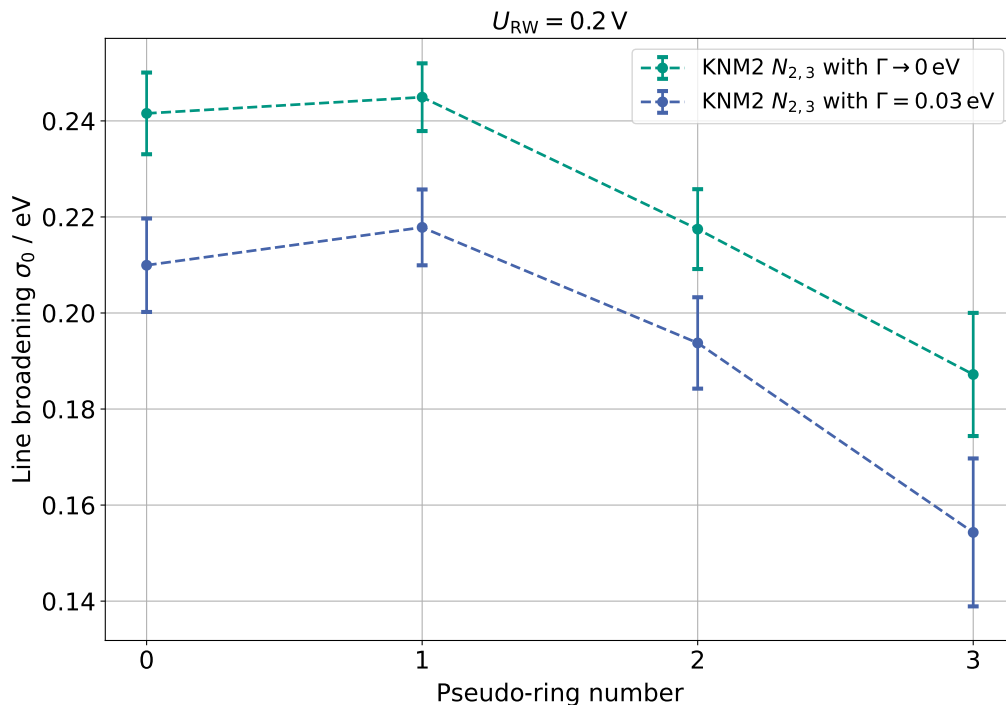


Figure 5.3: Pseudo-ring-wise line broadening of $N_{2,3}$ lines measurement. The intrinsic line width was assumed as a δ -function with $\Gamma \rightarrow 0$ and a regular Voigt profile with $\Gamma = 0.03$ eV. As expected, the line broadening is smaller for the $\Gamma = 0.03$ eV, because it absorbs some contribution of the total width in the intrinsic width. The line broadening σ_0 decreases at outer radii, which is explained in Sect. 5.5.2. The exact values for the δ -function are shown in Tab. A.6.

To further ensure the fit to converge, only the line position N_2 was fitted and the distance $\Delta E_{\text{rel}} = E_{\text{main},N_3} - E_{\text{main},N_2}$ was fixed by literature. The latter provides the value $\Delta E_{\text{rel}} = (670 \pm 14.1)$ meV [Vén+18].

Results and discussion

The pseudo-ring-wise fit results for the line broadening σ_0 are shown in Fig. 5.3. The shape of both $\Gamma \rightarrow 0$ and $\Gamma = 0.03$ eV look similar. Nevertheless, judging from the normed χ^2 (Fig. A.5), one can see that the model worked better for vanishing Lorentz widths, i.e. the total width can better be explained with Gaussian only. Therefore, it is proceeded with the line broadening values from the δ -function. In fact, they are the larger values and consequently the more conservative approach.

It can be noted that the fits themselves worked well, considering the low count rate in the order of 20 cps per pixel.

Due to the short measurement time (only one up/down scan) and thus the low total counts of the $N_{2,3}$ lines, the statistics is very low. This makes it more difficult to resolve the vanishing widths of the intrinsic lines. Thus, ring- or pixel-wise line broadening values are not used (Fig. A.6).

Also, σ_0 shows a radial dependence of ~ -18 meV/pseudo-ring = -6 meV/ring. This is also observed in the L_3 line measurements and therefore further discussed in Sect. 5.5.2.

The exact values from the δ -function approach, which are used to constraint the fitted line broadening in the L_3 line fits, are shown in tab Tab. A.6. The results for the intrinsic line widths are shown in Fig. 5.4. The values are in good agreement with one single value over all rings, which is physically expected but not directly visible from the L_3 line data, due to

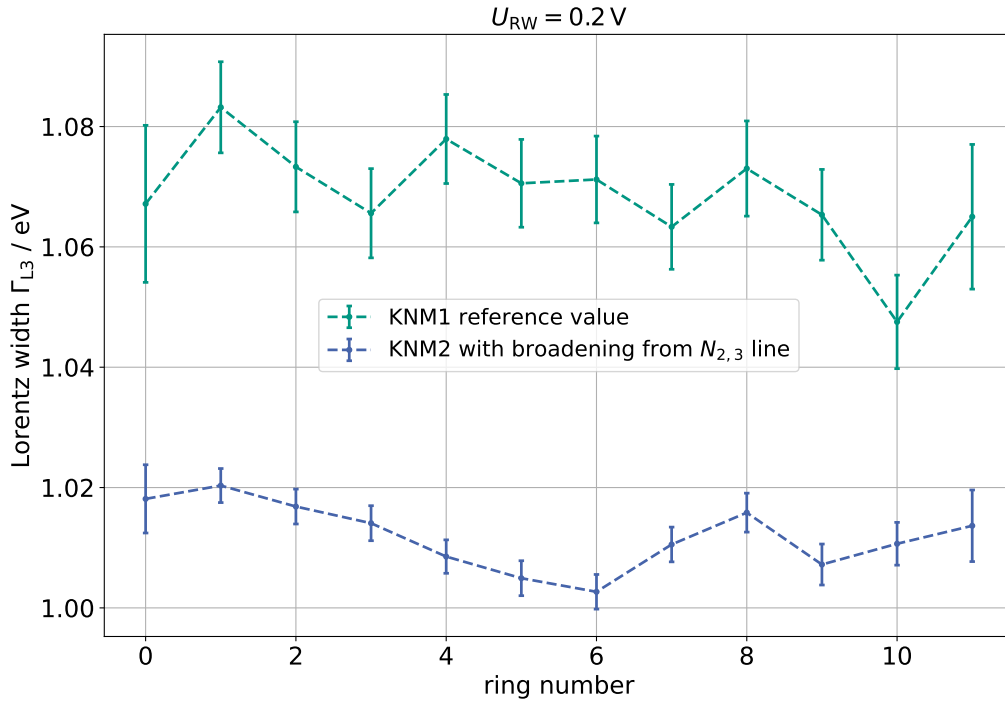


Figure 5.4: Fitted intrinsic L_3 line width with the $N_{2,3}$ constraining method, compared with the KNM1 reference measurement. Shown are the ring-wise values.

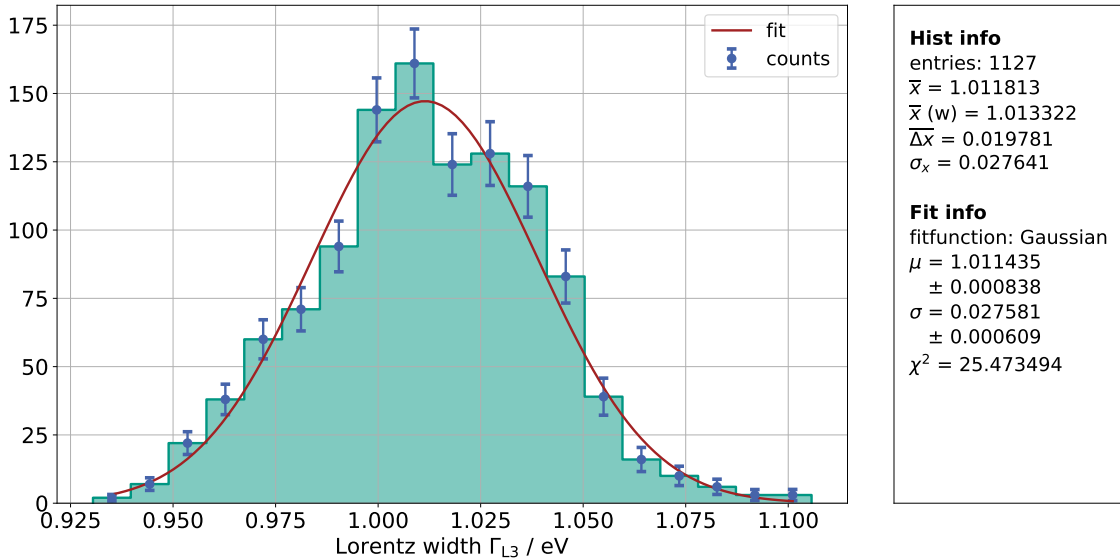


Figure 5.5: Histogram of fitted intrinsic L_3 line width with the $N_{2,3}$ constraining method. The results can nicely be described by Gaussian function around the mean value of $\Gamma_{L3} = 1.011$ eV.

the radial dependence of the total line width (Gauss + Lorentz). The fact that the fitted intrinsic Lorentz line width is radially constant, if using the radially dependent Gaussian line broadening values from the $N_{2,3}$ lines, shows that, with help from the pull method, the fit is capable of distinguishing between these two line width contributions.

Although the obtained values for the intrinsic line width do not show a general slope, they fluctuate more than their statistical uncertainties, indicating an additional systematic. One explanation for this are the reference values for the σ_0 themselves, which were used in a pseudo-ring-wise approximation.

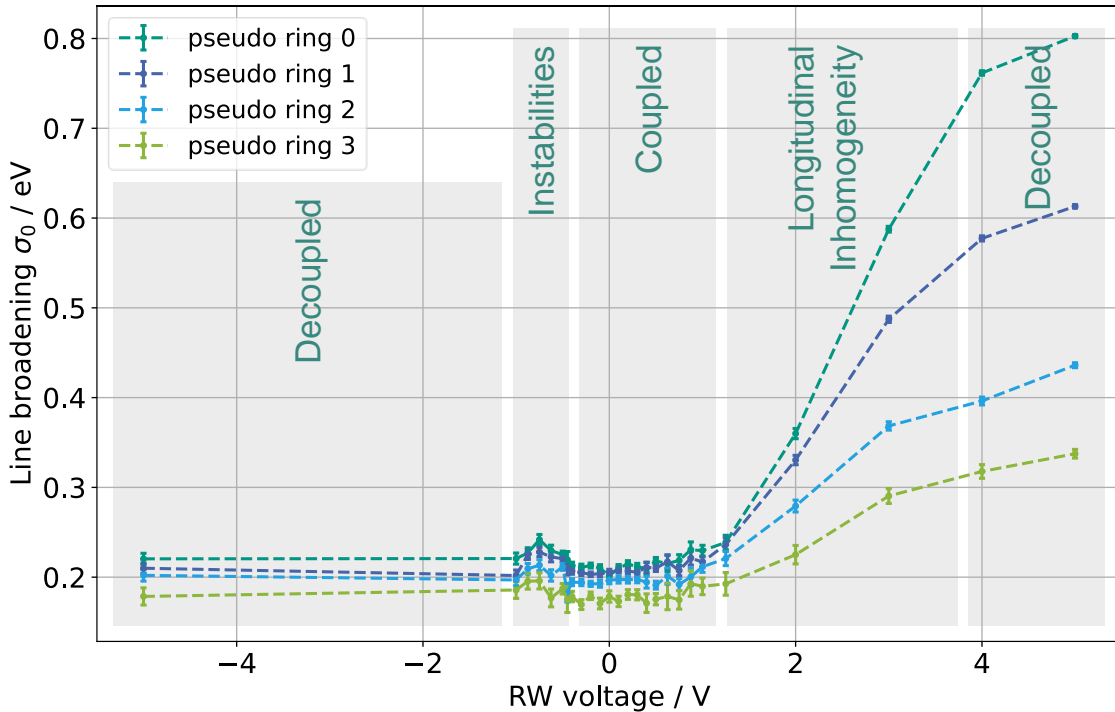


Figure 5.6: Pseudo-ring-wise line broadening over rear wall voltage. There are different regimes identifiable, depending on how the plasma reacts to a given rear wall voltage. The used rear wall voltages are not equidistant, meaning a focus was so set to the good coupling regime and positive voltages.

The mean value for the intrinsic line width can be determined to (Fig. 5.5)

$$\Gamma_{L3}^{\text{KNM2}} = (1.011 \pm 0.028) \text{ eV}. \quad (5.12)$$

This value is significantly smaller than the KNM1 reference value from Eq. (5.6). One possible explanation for this would be that the assumption of $\sigma_0 = 0$ in the reference measurements was not correct and there was an additional systematic contribution to the total line width. Consequently, this additional contribution is included in the reference value of the intrinsic line width. This is supported by the fact that the reference from KNM1 shows a radial dependence, which cannot be true for an intrinsic physical parameter.

Given the above, for the analysis of KNM2 krypton data it is proceeded with the reference value from the $N_{2,3}$ method.

5.4 Rear wall voltage dependent plasma regimes

The motion of ions and electrons inside the WGTS is determined by the drift due to electric fields, by the gas flow, and by diffusion. Driven by the gas flow, the ions leave the source to both ends and the electrons follow, creating the source potential shown in Fig. 3.5. The strong magnetic guiding field confines the ion and electron motion into longitudinal direction and maps the plasma in the WGTS onto the rear wall. The good longitudinal conductivity of the plasma allows to influence the plasma with the rear wall surface potential. In Fig. 5.6, the dependence of the krypton observable σ_0 on U_{RW} from -5 V to $+5 \text{ V}$ is shown. There are different regimes visible, which can phenomenologically be described as follows [Kuc16]:

- **Decoupled at negative rear wall voltages:** In the range $-5 \text{ V} \lesssim U_{\text{RW}} \lesssim -1 \text{ V}$, there is no dependence on the rear wall voltage visible. The negatively biased

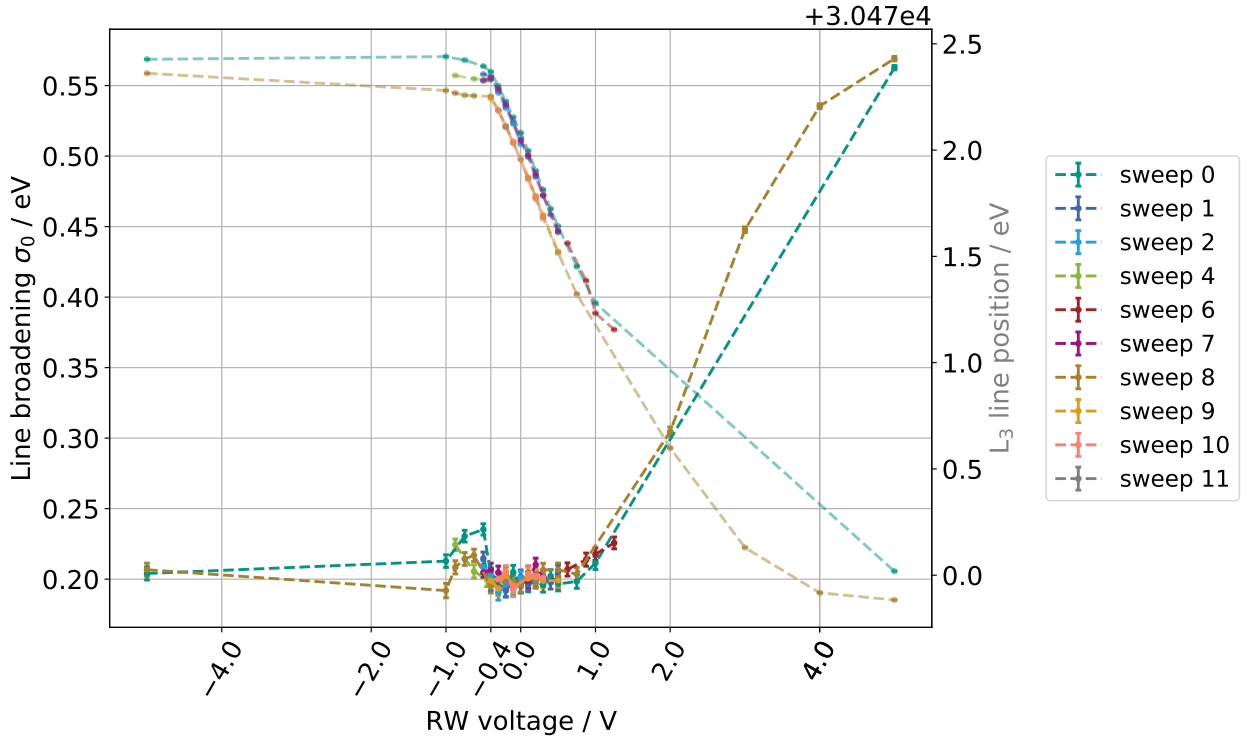


Figure 5.7: Sweep-wise line broadening and line position depending on the rear wall voltage. Here, the slightly transparent curves (from top left to bottom right) represent the line position. The shift in the line position is caused by a time dependent drift. The different sweeps show consistent results for almost all rear wall voltages. In the range $-1 \text{ V} \lesssim U_{RW} \lesssim -0.4 \text{ V}$ on the other hand, instabilities were observed, which lead to non-reproducible results.

rear wall blocks electrons, causing an overall negative space charge. Due to the magnetic confinement and the negative potentials at rear wall and dipole electrodes, the electrons must leave the source for the largest part via recombination. The slight increase of the rear wall current at even more negative rear wall voltages points to another mechanism that allows electrons to leave the source. One possibility are plasma instabilities which drive electron diffusion perpendicular to the magnetic field lines. An even more negative rear wall voltage does not change this picture because the major driver, the electron blocking of the rear wall, is already saturated at smaller absolute values of the rear wall voltage.

- **Instable:** In the range of $-1 \text{ V} \lesssim U_{RW} \lesssim -0.4 \text{ V}$ there is an increase of the line broadening visible compared to both neighbored regions, which is not understood yet. All three scans performed in this region show slightly different results which favors instabilities as possible cause. Small break-downs of the longitudinal fields could allow for electron batches to travel from the charged-up source to the rear wall. At more negative voltage, the coupling brakes down, the effect vanishes, and the transition to the decoupled regime is smoothed out.
- **Coupled:** In the range of $-0.4 \text{ V} \lesssim U_{RW} \lesssim 1 \text{ V}$, one can observe a good coupling regime, meaning the absolute plasma potential is dominated by the external potential of the rear wall (see line position in Fig. 5.7). The plasma not positively charged throughout the good coupling region. The turning point is supposed to be the point of minimal radial inhomogeneity, which lies inside the good coupling region. Below this turning point, electrons start to get trapped and ions can reach the rear wall.
- **Longitudinal inhomogeneity:** In the range of $1 \text{ V} \lesssim U_{RW} \lesssim 4 \text{ V}$ the plasma shows

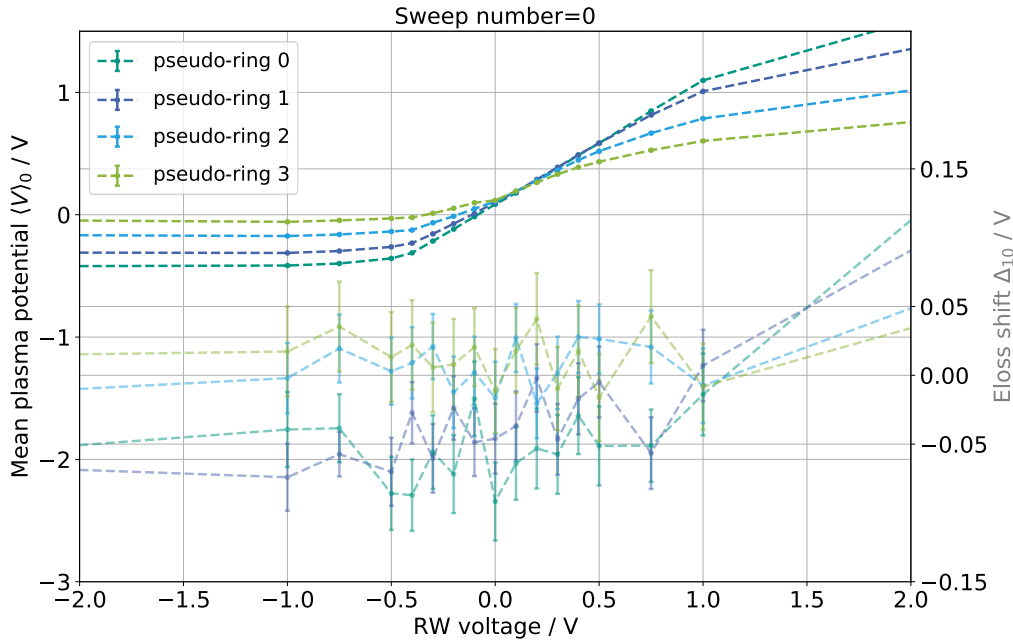


Figure 5.8: Rear wall voltage dependent energy loss shift parameter and mean plasma potential, exemplary for the first sweep. The four lower, slightly transparent, curves describe the pseudo-ring-wise energy loss shift Δ_{10} . The mean plasma potential is derived from the line position, using the KNM1 reference value. In the good coupling regime and for negative rear wall voltages the energy loss shift parameter barely changes and rises at the beginning of the inhomogeneity regime $U_{RW} > 1$ V.

increasing longitudinal and radial inhomogeneities with larger rear wall voltage. In this regime, the transition from good coupling to the decoupled regime accomplish. The strong radial dependence (pseudo-ring-wise) is explained in Sect. 5.5.

- **Decoupled at positive rear wall voltages:** In the range of $4 \text{ V} \lesssim U_{RW} \lesssim 5 \text{ V}$ the electron currents on the rear wall saturate and a positive space charge has built up inside the WGTS, as can be seen from the line position.

5.4.1 Longitudinal shape

The rear wall voltage dependent plasma regimes are described by the Voigt profile parameters line position and line broadening, which mainly represent the front part of the WGTS. Because this part is further away from the rear wall, the measured values should hold through the whole WGTS. To crosscheck this assumption and to investigate also the rear part of the WGTS, the energy loss shift parameter Δ_{10} from the scattering model (Sect. 4.4.2) can be used. Fig. 5.8 shows the dependence of the energy loss shift and the mean plasma potential $\langle V \rangle_0$ on the rear wall voltage. The mean plasma potential $\langle V \rangle_0$ is calculated using Eq. (4.13). The observed shape matches the expectations from Sect. 5.4. At negative rear wall voltages < -1 V, the rear wall is decoupled from the plasma and the penetration depth is short. The whole rear wall potential drops right at the rear wall and even more negative voltages does not change the longitudinal potential. As a consequence, $\langle V \rangle_0$ and Δ_{10} are constant.

In the instability regime $-1 \lesssim U_{RW} \lesssim -0.4$ V, the line position values of the different sweeps show non-reproducible results. However, the energy loss shift does not show a significant effect larger than the typical fluctuations indicating that the front and the rear part are equally influenced by the instabilities.

In the good coupling regime $-0.4 \lesssim U_{RW} \lesssim 1$ V, the plasma follows the external potential and shifts the whole plasma potential. In this regime, $\langle V \rangle_i$ scales linear with the rear wall

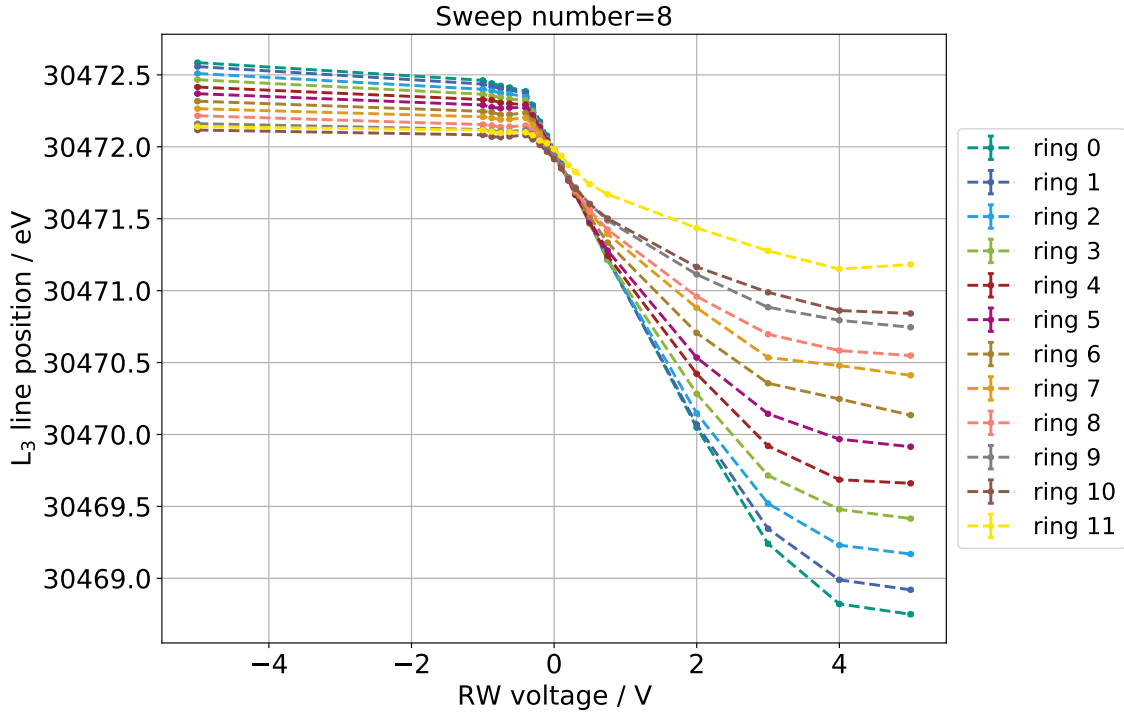


Figure 5.9: Line position versus rear wall voltage of all rings, exemplary for sweep 8. One can identify the uncoupled regions at large absolute rear wall voltages and the coupled region of $-0.4 \text{ V} \lesssim U_{\text{RW}} \lesssim 1 \text{ V}$. The latter can be used to determine the radially dependent coupling strength of the rear wall to the plasma. Also, there is a point of best radial homogeneity, where all lines cross.

voltage, leading to a constant Δ_{10} for outer rings and a small positive slope on inner rings due to the asymmetric potential shape.

For $U_{\text{RW}} \geq 1 \text{ V}$, the influence of the rear wall does not reach into the whole WGTS. It affects the rear part ($\langle V \rangle_1$) more than the front part ($\langle V \rangle_0$). Therefore, the coupling of $\langle V \rangle_0$ to the rear wall decreases, leading to an increase of the absolute Δ_{10} .

5.5 Radially dependent plasma potential

As can be seen in Fig. 5.9 and Fig. 5.6, there are radial effects visible for both L_3 line position and line broadening. They are of different shape, because the line position is proportional to the absolute potential $\langle V \rangle_0$, whereas the line broadening measures the longitudinal deviation from this value and other effects like temporal fluctuations or the influence of the as constant approximated background slope. Because it is difficult to distinguish between radial effects caused by the background slope and physical radial effects, like the radially dependent coupling of the rear wall to the overall plasma, identifying the reason and the causality between the radial decrease of the fitted parameter is challenging. With this in mind, only assumptions can be made.

Due to the strong dependence of the plasma on the gas densities, a radially decreasing column density could cause radial plasma observables. Although this is observed, it is most likely an effect caused by the background slope, as described in more detail in Sect. 5.5.1. A radially decreasing coupling strength is expected, because electrons can better compensate density inhomogeneities at the center of the flux tube where they see directly the potential of the rear wall. The less mobile ions on outer radii smooth out the transition to the grounded beam tube, leading to a worse coupling. This theory is quantified in Sect. 5.5.2.

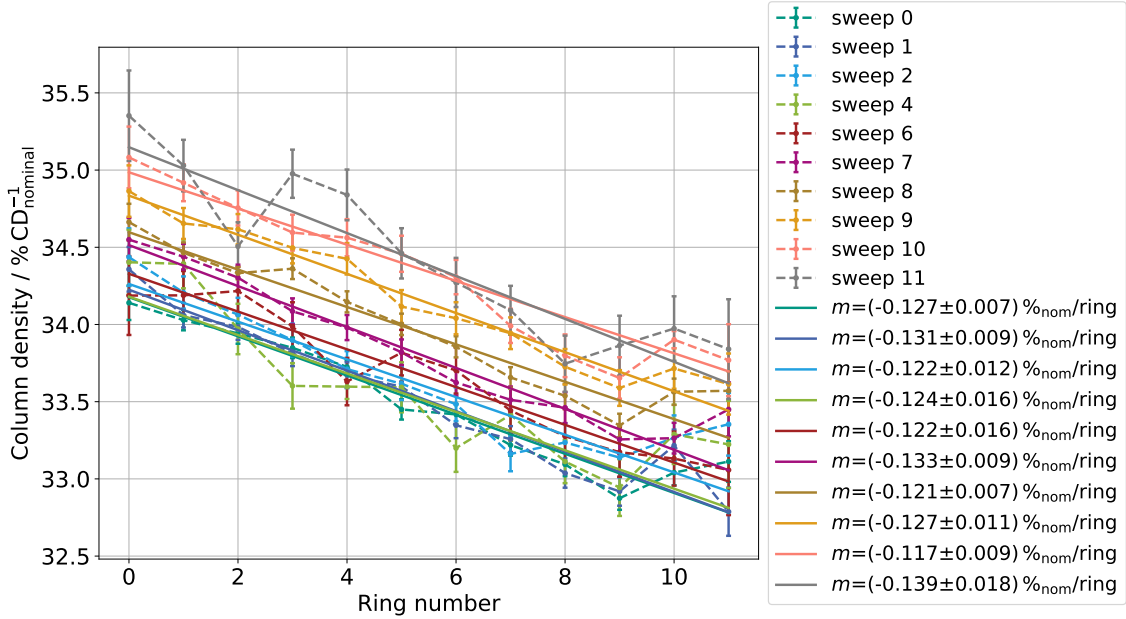


Figure 5.10: Fitted column density depending on the ring number for the different sweeps. Two effects are visible. First, the overall column density rises in time as can be seen by the continuously shifting sweep number and second, the fitted column density decreases radially, which can be caused by the background slope.

5.5.1 Radially dependent column density

In Fig. 5.10, the fitted column density over rings for each sweep is shown and linearly fitted. All sweeps draw a consistent picture of an averaged radial slope of $\sim (-0.125 \pm 0.003) \%_{\text{nom}}/\text{ring}$, which is $\sim (-0.368 \pm 0.009) \%/ring$ relatively to $\sim 34 \%_{\text{nom}}$. Consistently, the krypton activity in Fig. 5.20, which is directly proportional to the krypton column density, also shows a radial decrease. This supports the fact that there is a radial dependence in the column densities. This is unexpected, because all gas model simulations result in a radial homogeneity at the level of 10^{-5} [Mac16]. However, this favors the explanation that this effect is not a physical effect but caused by the background slope.

It is also to mention that for the determination of the column density, the amplitude of scattered electrons of the fitted krypton spectrum is used. Any other radial systematic effect which influences this krypton observable has an influence on the fitted column densities.

Given the above, it cannot be inferred whether the radially decreasing column density is cause or consequence of radially dependent plasma observables. As a consequence precise plasma simulations are needed.

5.5.2 Radially dependent coupling to the rear wall

Based on Fig. 5.9 and Fig. 5.6, the radially dependent coupling to the rear can be describes as follows.

In the good coupling regime, the plasma potential follows the external rear wall voltage without increasing the overall longitudinal inhomogeneity. Even so, this longitudinal inhomogeneity is not constant for all radii, but shows the influence of the background slope and the radially dependent coupling to the rear wall, leading to a radially inhomogeneous mean plasma potential.

At higher rear wall voltages $U_{\text{RW}} > 1 \text{ V}$, the overall longitudinal inhomogeneity increases and amplifies the radial effect because the radial inhomogeneity of the mean plasma potential increases.

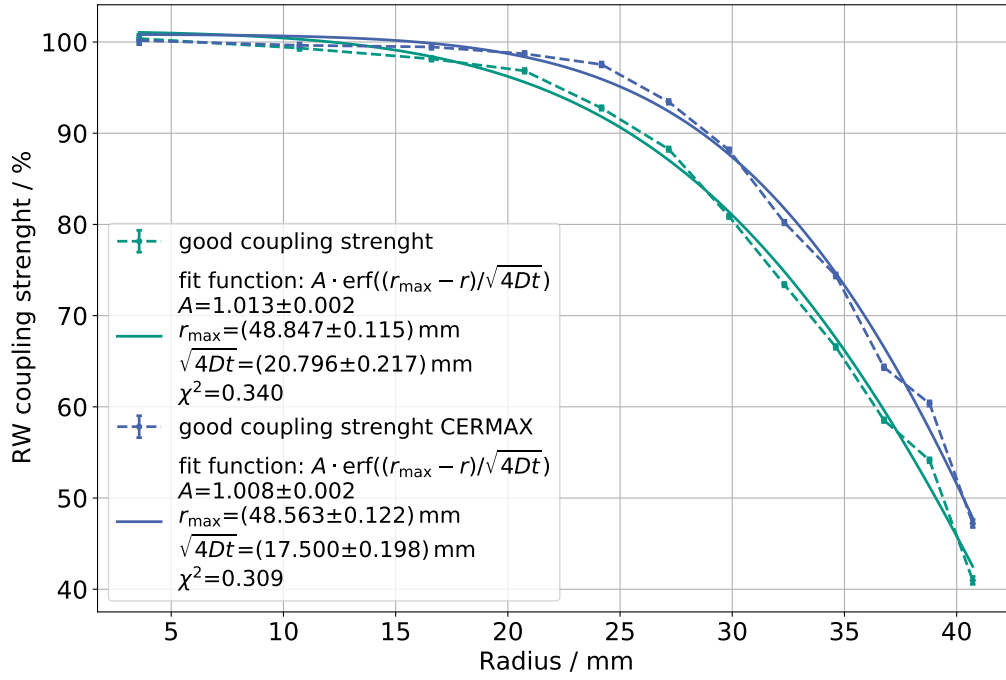


Figure 5.11: Radial coupling strength in good coupling regime. The values for the good coupling strength were determined by fitting the linear regime $-0.4 \text{ V} \lesssim U_{\text{RW}} \lesssim 1 \text{ V}$ of the line positions (see plot Fig. 5.9), for one exemplary sweep 8, and the CERMAX measurements.

Table 5.1: Fit results of Fick's equation for the good coupling regime in KNM2 krypton (Fig. 5.11) and CERMAX compared to PRO-KATRIN [Kle20].

	Amplitude A	Offset r_{\max} / mm	Kurtosis $\sqrt{4Dt}$ / mm	χ^2
PRO-KATRIN	1.009 ± 0.010	48.286 ± 0.831	18.116 ± 1.291	-
Krypton	1.013 ± 0.002	48.847 ± 0.115	20.796 ± 0.217	0.340
Krypton CERMAX	1.008 ± 0.002	48.563 ± 0.122	17.500 ± 0.198	0.309

Eventually, in the decoupled region, the plasma barely follows the externally applied rear wall voltage, thus the coupling strength $\rightarrow 0$.

Good coupling regime

The radial decrease of longitudinal inhomogeneity can be explained by analyzing the radial coupling of the absolute plasma potential to the rear wall. Fig. 5.9 shows the fitted L_3 line position depending on the applied rear wall voltage for each ring. The slope in the good coupling region can be interpreted as the coupling strength, i.e. how well the plasma potential follows the external one. The obtained slopes are plotted in Fig. 5.11 against the average radius of the corresponding ring. One can see that in the center the coupling is optimal and decreases to $\sim 40\%$ at the outermost ring 11.

To quantify the radially dependent plasma coupling, the error function as eigenfunction of diffusion processes, described by the Fick's equation [Per16]

$$\Phi(r) = A \cdot \text{erf} \left[\frac{r_{\max} - r}{\sqrt{4Dt}} \right] \quad (5.13)$$

is used. Here, A is the amplitude at $r = 0$, r_{\max} is the maximal radius where ions would be expected, i.e. the wall, and the parameter $\sqrt{4Dt}$ combines the diffusion constant D and

its time scale t .

The fit function describes well the observed behavior of a flat potential at the center and a decrease towards the beam tube wall, where the influence of the beam tube is getting stronger. This supports the assumption that positively charged ions are drifting towards the beam tube walls, where they are getting removed. The fit results are shown in Tab. 5.1 and compared to the corresponding PRO-KATRIN measurements at the same operational conditions (column density, temperature, etc.), but with tritium only¹. The results are in good agreement with each other, considering that the PRO-KATRIN measurements use a different method to determine the radial coupling.

Also, looking at the CERMAX curve shows how the additional photo electrons, caused by UV illumination, increase the overall coupling strength. At the center, the coupling is also without UV light perfect, but decreases with larger radii. This decrease is damped with CERMAX, especially for smaller radii and less on the outer radii. This can be explained by the boundary condition that the outermost ring must match the beam tube potential in both cases.

The results match to the expectations from the transversal plasma simulation shown in Fig. 5.12. It is to mention that the plasma potential simulation applies for a planar plasma (2D) configuration, but [Kuc16] has shown that for most potential shapes, it is a good approximation of the realistic axial-symmetric WGTS model. The transversal plasma potential shape at different z -positions illustrates the expectation of larger inhomogeneities at the center compared to larger radii. The krypton observable for longitudinal inhomogeneity σ_0 measures longitudinal deviations of the mean plasma potential $\langle V \rangle_0$, i.e. approximately the difference in amplitude of the blue and dark green curve in Fig. 5.12. One can see that this difference results in a curve of the same shape, but scaled to a smaller overall amplitude. As a result, the center shows the largest longitudinal inhomogeneity due to its best coupling.

Nonetheless, the radially dependent coupling is based on radially varying mean plasma potentials. However, in the good coupling regime at the point of best radial homogeneity, where all radii show the same mean plasma potential $\langle V \rangle_0$, the line broadening values σ_0 still show a remaining radial dependence which could be explained by the background slope.

The radially dependent coupling as cause for radial dependent inhomogeneities can be crosschecked by looking at larger rear wall voltages, i.e. the longitudinal inhomogeneity regime, and the relative line broadening with respect to the mean plasma potential.

Longitudinal inhomogeneity regime

Analog to the good coupling regime, the longitudinal inhomogeneity regime is characterized by radially dependent coupling strengths. But in this regime, the coupling strength is not constant for one ring in the whole regime, but slowly decreases towards the saturation regime at ~ 5 V. At such high rear wall voltages, the plasma potential decouples from the rear wall. Moreover, the overall increasing longitudinal inhomogeneity makes the difference of the radially dependent coupling strength more visible.

It is to mention that the coupling strength values are determined in the good coupling regime and do not hold for rear wall voltages outside the regime. Nonetheless, the relative connection that the inner rings couple better than the outer ones still holds for $U_{RW} > 1$ V (Fig. 5.9). The observed radial line broadening values of Fig. 5.13 show a similar pattern as the coupling strength in the line position values itself, which can be explained as follows. The overall shape of the longitudinal plasma is assumed to be the same and gets scaled

¹PRO-KATRIN measurements monitor the FPD rate deep inside the tritium spectrum while changing the rear wall voltage.

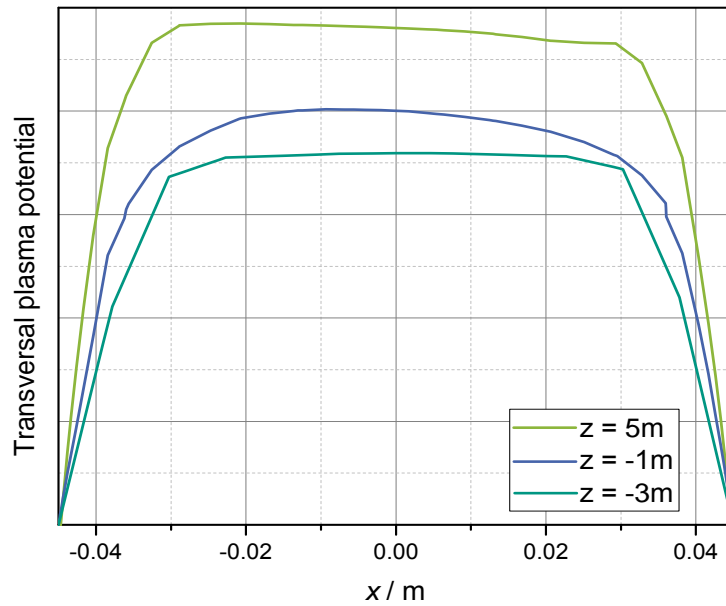


Figure 5.12: Simulated transversal plasma potential shape for planar plasma (2D) for different z -positions. The rear wall is at +1 V potential compared to the beam tube, i.e. right in between the good coupling regime and the start of longitudinal inhomogeneity. The simulation is calculated for tritium mode regarding temperature and column density. Plot from [Kuc16] (modified).

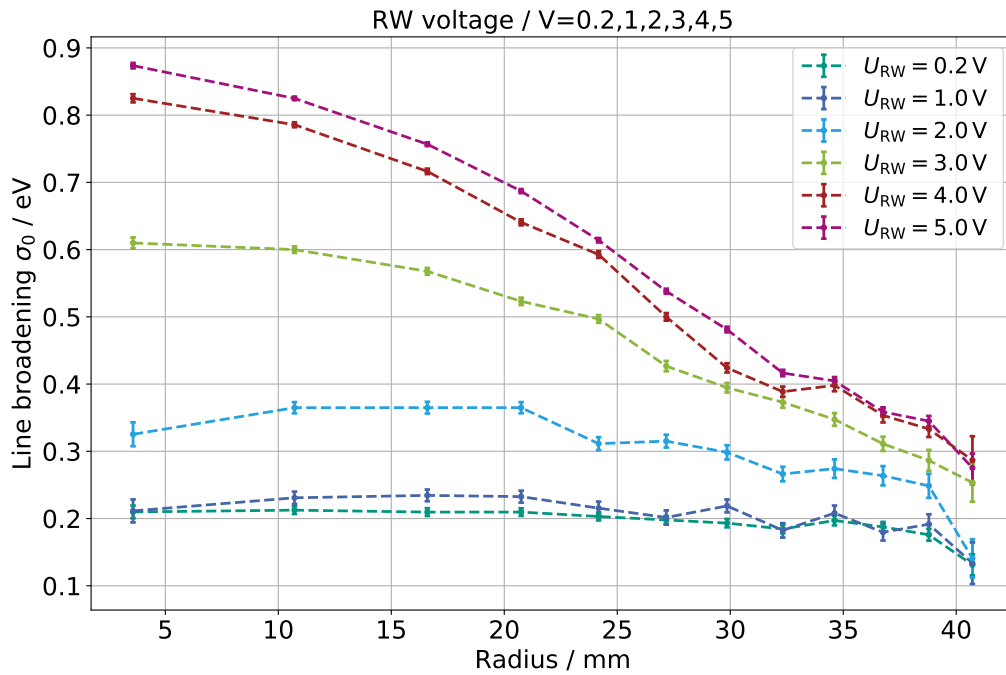


Figure 5.13: Line broadening over radius for rear wall voltages from good coupling, longitudinal inhomogeneity, and decoupled regime. The shape of the curves matches the expected shape from the radially dependent coupling strength.

with different rear wall voltages. Thus, a smaller absolute potential on outer radii also leads to smaller line broadening values. Therefore, at small radii, the line broadening increases significantly with the rear wall voltage, whereas at outer radii, only a small influence on U_{RW} can be seen. In fact, at the outermost radius, all values show almost the same broadening of ~ 0.2 eV, which matches the boundary condition that the line broadening

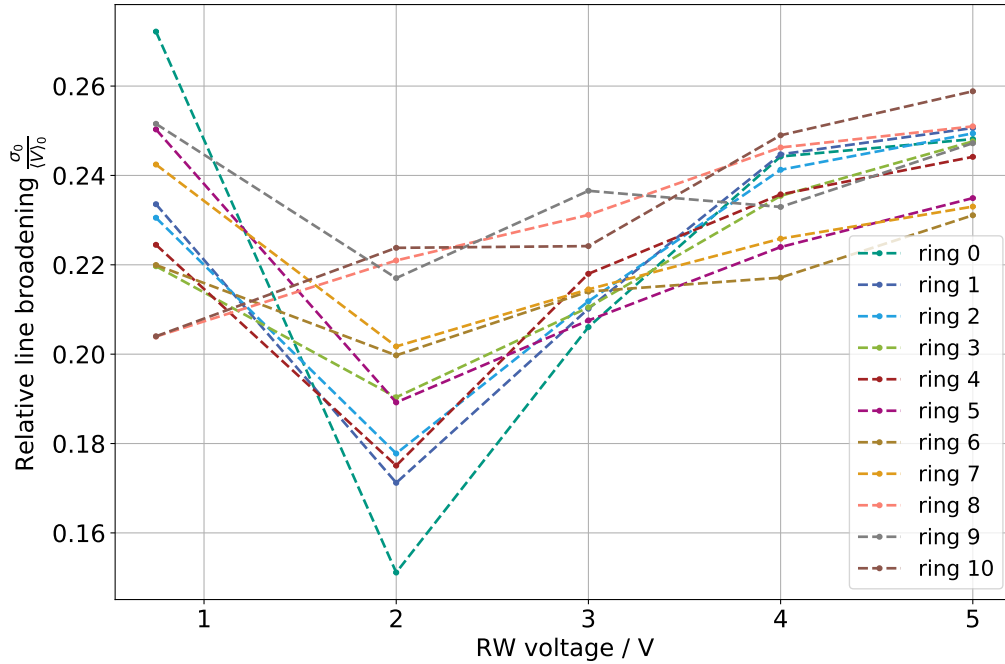


Figure 5.14: Ring-wise relative line broadening, exemplary for sweep 8. Ring 11 was excluded due to bad statistics and the error bars are removed for better visibility. The curves diverge towards the rear wall voltage at which the line position matches the reference value $E_{\text{main,ref}}$, because the denominator $\langle V \rangle_0$ equals zero. Thus, only rear wall voltages ≥ 0.75 V are shown. However, all rings show a similar shape and the radial dependence of σ_0 cannot be observed anymore. It must be mentioned that the result must be taken carefully because it strongly depends on the reference value $E_{\text{main,ref}}$, which was used from KNM1 and measured at different source conditions. A larger or smaller value increases the line distance of the individual rings significantly.

must vanish at the beam tube walls. The value is not zero because it is not right next to wall. There is another ring, which could not be included in the analysis due to the pixel selection. Additionally, the influence of the background slope is not considered yet.

This explanation can be verified by looking at the relative line broadening $\sigma_0/\langle V \rangle_0$. If they are both driven by the coupling effect, one would expect the ring dependent shapes to behave equally.

To calculate $\langle V \rangle_0$ from the line position via Eq. (4.13), the reference position $E_{\text{main,ref}}$ of L_3 must be known. This value refers to the point at which to expect no plasma potential. However, because this value is measured with an empty source, additional effects can falsify this value as discussed in Sect. 5.2. Additionally, this parameter was not measured in KNM2 and hence the value from KNM1 is used.

Because the line broadening values are consistently positive, whereas the mean plasma potential has a zero crossing, the relative line broadening diverges at $E_{L3,0} = E_{\text{main,ref}}$. As a result, the relative line broadening strongly depends on the reference value $E_{\text{main,ref}}$. Thus, the result shown in Fig. 5.14 must be interpreted carefully.

However, the radial dependence disappears which indicates that the radially dependent line broadening in this regime is a consequence of the radially dependent coupling.

Additionally, there is another effect contributing to the absolute value of the line broadening observable. In the decoupled regime, each ring converges to a different absolute potential value as can be seen in Fig. 5.9. Consequently, at $U_{\text{RW}} = 5$ V there is a total radial potential gradient of

$$\Delta V \simeq 2.5 \text{ eV} / (11 \text{ rings}) = 227.27 \text{ meV ring}^{-1}.$$

This radial gradient adds a significant contribution to the observed line broadening because one ring integrates over a certain amount of radial distance. Approximating this radial potential drop from the inner to the outer rings as linear, a Gaussian standard deviation of this flat distribution is $\sigma_{\Delta V} \simeq 65.53$ meV.

This radial inhomogeneity within one ring ΔV is approximately constant for all rings, because the radial ring width decreases towards outer rings¹, but the potential gradient increases. Therefore, the different rings in Fig. 5.14 still show the same relative line broadening.

Ultimately, the model of diffusion of ions and electrons introduced in Sect. 5.4 and Sect. 5.5.2 is good to consistently describe the observed rear wall and radially dependent line broadening. On the other hand, this description lacks the validation from a detailed plasma simulation at krypton conditions for both radial and longitudinal coordinates. Moreover, the precise discussion of the influence of the background slope could no be considered.

5.6 Rear wall voltage of best radial homogeneity

As Fig. 5.9 indicates, there is a point at which the average potential for all rings is identical². This point $U_{\text{RW,hom}}$ is of major interest because it is comparable with a ring-wise constant endpoint E_0 in neutrino mass measurements and is expected to also be the point of the best longitudinal homogeneity.

To obtain $U_{\text{RW,hom}}$ and to not be limited to the distinct measured rear wall voltages, the line position values get interpolated and the point $U_{\text{RW,hom}}$ fitted as described in the following. The general idea is to calculate the standard deviation and its error of the measured L_3 line positions at each U_{RW} available in the good coupling range³, individually for all sweeps. Further, the points are fitted under consideration of their error with a fit function which includes the position of the minimum $x_0 = U_{\text{RW,hom}}$ as a free parameter.

At each rear wall voltage, the sample standard deviation of the rings s can be calculated via

$$s = \sqrt{\frac{1}{n-1} \sum_i (x_i - \mu)^2}. \quad (5.14)$$

In this equation, x_i are the line positions for ring i , and μ the sample mean of x_i . Calculating the standard error of s can be done using the connection to the χ^2 distribution with $n-1$ degrees of freedom [EL98]

$$\chi_{n-1}^2 \propto \frac{(n-1)s^2}{\sigma^2}. \quad (5.15)$$

The variance of χ_{n-1}^2 is well known as

$$\sigma_{\chi_{n-1}^2} = 2(n-1). \quad (5.16)$$

The corresponding standard error of s^2 can therefore be determined to

$$\sigma_{s^2} = \sigma^2 \sqrt{\frac{2}{n-1}} \approx s^2 \sqrt{\frac{2}{n-1}}. \quad (5.17)$$

In this equation, s^2 is used as the most likely estimator for σ^2 . Eventually, because the parameter of interest is s , not s^2 , the error gets propagated in the same way as derived in Eq. (5.4).

¹The exact values for the radii can be found in Tab. 2.1.

²Fig. A.7 provides a different view on the data. Here, the searched $U_{\text{RW,hom}}$ represents a flat line over all rings.

³One can see that the point of best radial homogeneity is inside this regime.

For the fit function f , a combination of both quadratic and linear functions is chosen. The latter are motivated by the expected linear increase of the line distances to each other away from the minimum. The quadratic function is used to model the tipping point in the minimum.

The result is a parabolic function near the minimum with a curvature a in the range $(x_0 - c/2, x_0 + c/2)$ and linear curves with the same absolute slopes $\pm a \cdot c$ on both sides. An offset in y -direction is given by b . Continuity is required at both junctions, leading to the definition of f

$$f(x_0, a, b, c) = \begin{cases} -ac \cdot x + b + ac(x_0 - c/4) & \text{if } x < x_0 - c/2 \\ a(x - x_0)^2 + b & \text{if } x_0 - c/2 \leq x \leq x_0 + c/2 \\ ac \cdot x + b - ac(x_0 + c/4) & \text{if } x > x_0 + c/2. \end{cases} \quad (5.18)$$

One exemplary fit with this function is shown in Fig. 5.15.

This procedure is repeated for all performed sweeps, which provide enough (≥ 4) measured rear wall voltages in the good coupling regime. The fits works well and are able to consistently find the minimum. The result can be seen in Fig. 5.16. The values fluctuate in a relatively small range of ~ 20 mV around the mean value of

$$U_{\text{RW, hom}} = (159.65 \pm 6.60) \text{ mV}. \quad (5.19)$$

The first value is comparably high, but still compatible with the rest of the values. It can be concluded that the rear wall voltage of best radial homogeneity is not drifting over time which is an interesting fact considering the observed drift of the L_3 line position discussed in Sect. 5.8. Thus, $U_{\text{RW, hom}}$ can be assumed to be a constant intrinsic plasma property for the configuration in KNM2.

5.7 Time dependent drifts of column densities

In krypton mode, there are two column densities, the gas column density, mainly consisting of tritium, and the krypton column density. However, because the tritium column density is several magnitudes larger than the krypton one, it has the dominating influence on the plasma. Nevertheless, the stability of both should be investigated because the krypton conversion electrons are measured and a drift leads to a change of the observables.

Gas column density

As Fig. 5.10 indicates, there is a clear rise in overall gas column density over time. This is displayed for each pseudo-ring in Fig. 5.17. The shape is linear, despite little fluctuations caused by the limited sensitivity on the first scattering peak which is used for the fitting of the column density. The slope is equal within the uncertainties for all pseudo-rings and averages to $\bar{m} = (0.137 \pm 0.005) \%_{\text{nom}}/\text{d}$ which is $\sim 0.4 \%/\text{d}$ relative to the scale of $\sim 34 \% \text{CD}_{\text{nom}}^{-1}$. A drifting column density is not unusual in krypton mode and can be traced back to the different circulation mode of tritium, as described in Sect. 4.1.

It is difficult to conclude whether the overall plasma potential increases or decreases with increasing gas column density. In the case of 30 K, [Kuc16] has shown that a different column density should not affect the plasma in a way that it changes its shape, but scales it to a different overall plasma potential. In this case, simulations show that the front side of the WGTS is more affected by this scaling than the rear part which could therefore lead to a change in longitudinal homogeneity. Fig. 5.18 shows this qualitative connection, but must be taken with care, due to the different temperature in krypton mode and other simplifications which were made in the simulation (Sect. 3.4).

To crosscheck this theory, the energy loss shift Δ_{10} can be used because it is a measure for the potential difference of the front and rear part of the WGTS. However, this parameter

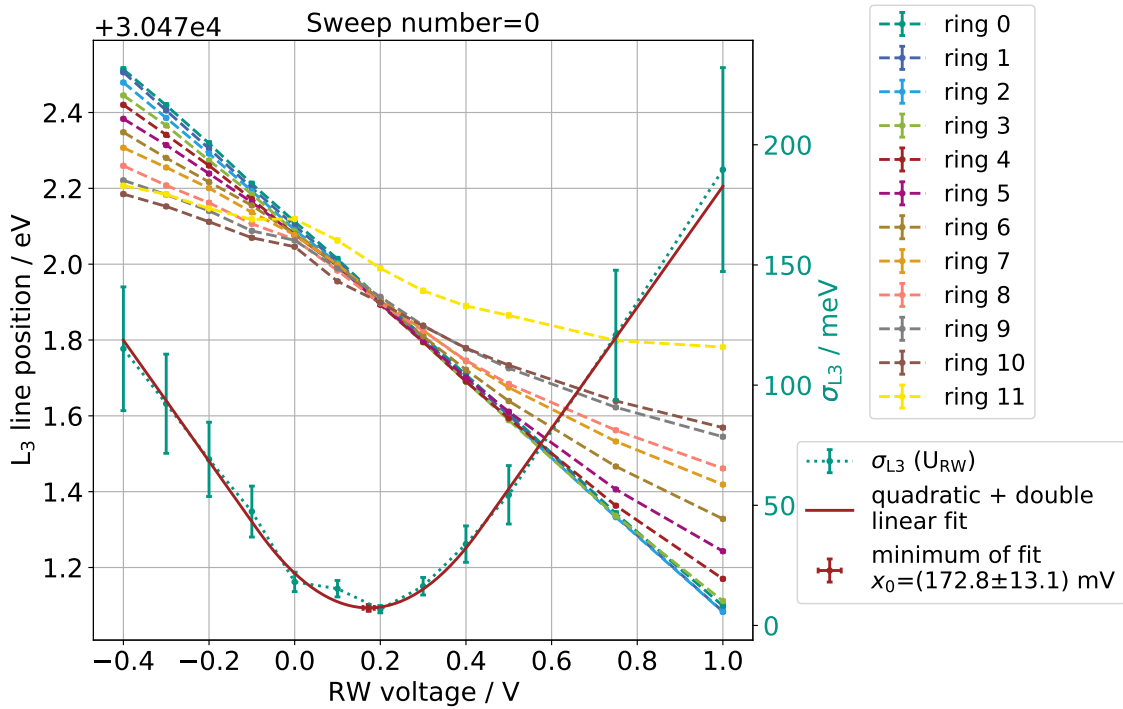


Figure 5.15: Ring-wise line positions in the good coupling regime along with the resulting standard deviation, exemplary for the first sweep. Note that σ_{L_3} is not the fitted line broadening σ_0 , but the standard deviation of the displayed L_3 line position curves. σ_{L_3} is used to determine the point at which all points are closest to each other, i.e. the point of best radial homogeneity. Ring 11 was excluded because it shows strong deviations from a linear behavior and distorts the calculations of σ_{L_3} . The minimum is fitted using a combination of quadratic and linear fit. The results matches the expected position seen by eye.

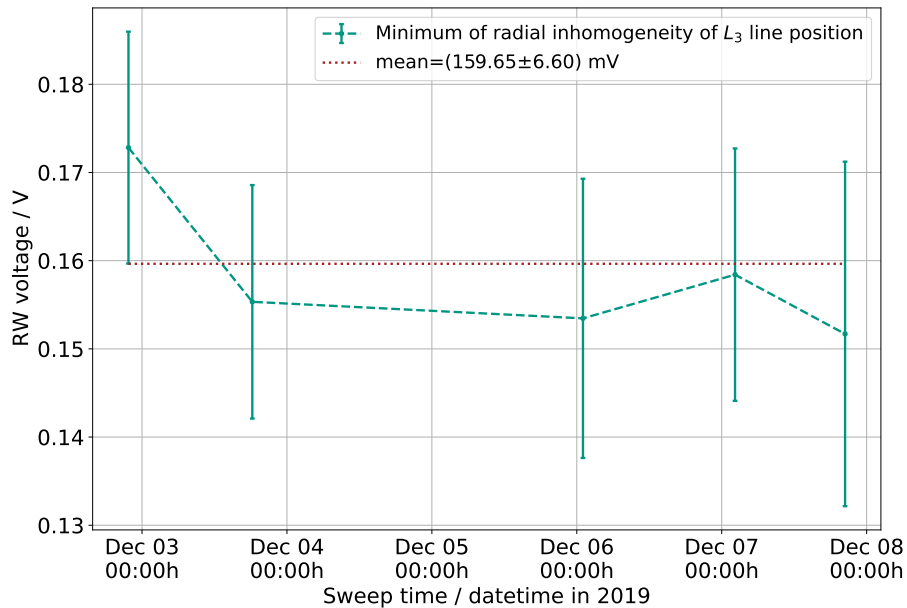


Figure 5.16: Rear wall voltage of best radial homogeneity over time during the KNM2 krypton campaign. Each point represents the fit results of the minimum determination as shown in Fig. 5.15.

lacks the needed reference value, i.e. the energy loss function ϵ_{loss} at 30 keV. This means it

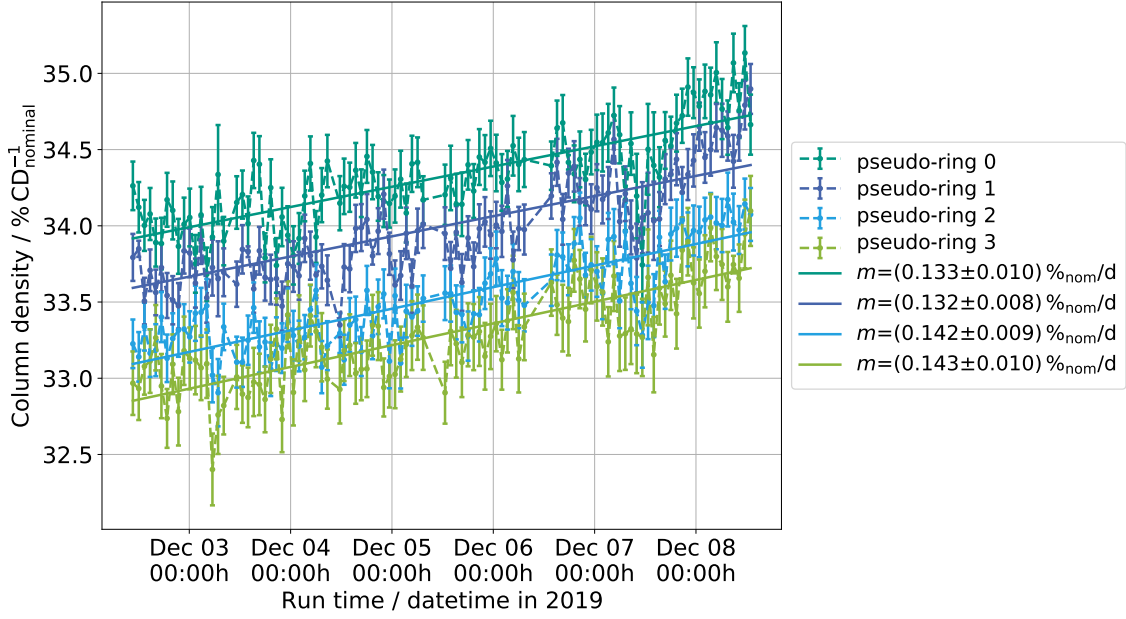


Figure 5.17: Fitted column density over time for each pseudo-ring. This is an alternative view of Fig. 5.10. The overall column density rises with the same slope for all pseudo-rings. The increase of the absolute column density towards the center could be explained by the background slope.

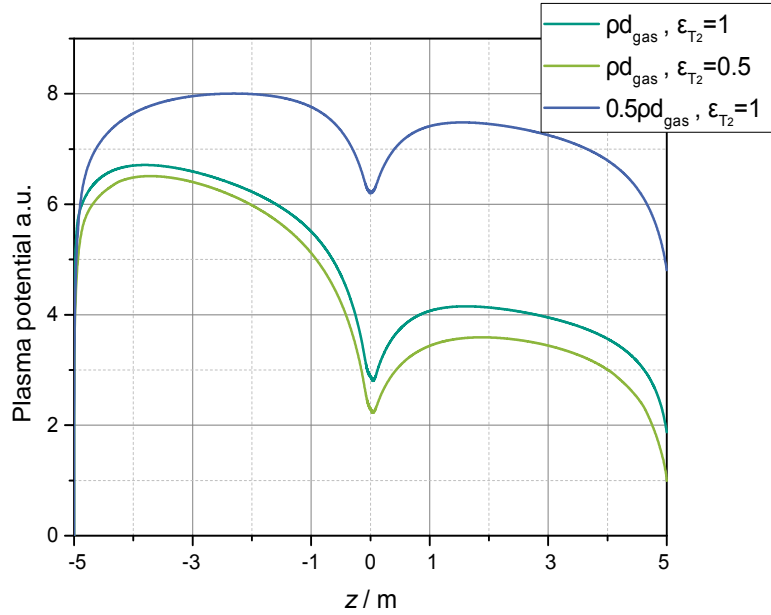


Figure 5.18: Illustration of plasma dependence on different column density configurations. Parameter ρd_{gas} describes the overall column density of all gases which are inside the WGTS and ϵ_{T2} the fraction of ρd_{T2} in ρd_{gas} . A smaller ϵ_{T2} corresponds to larger impurities. Plot from [Kuc16] (modified).

is not known which value corresponds to the zero crossing of Δ_{10} . As a consequence, it cannot be said if an increasing Δ_{10} parameter corresponds to an increase or decrease of the potential difference. The information which can still be extracted from Fig. A.8 is that the inhomogeneity of front and rear part of the WGTS change linearly over time, similar to the gas column density.

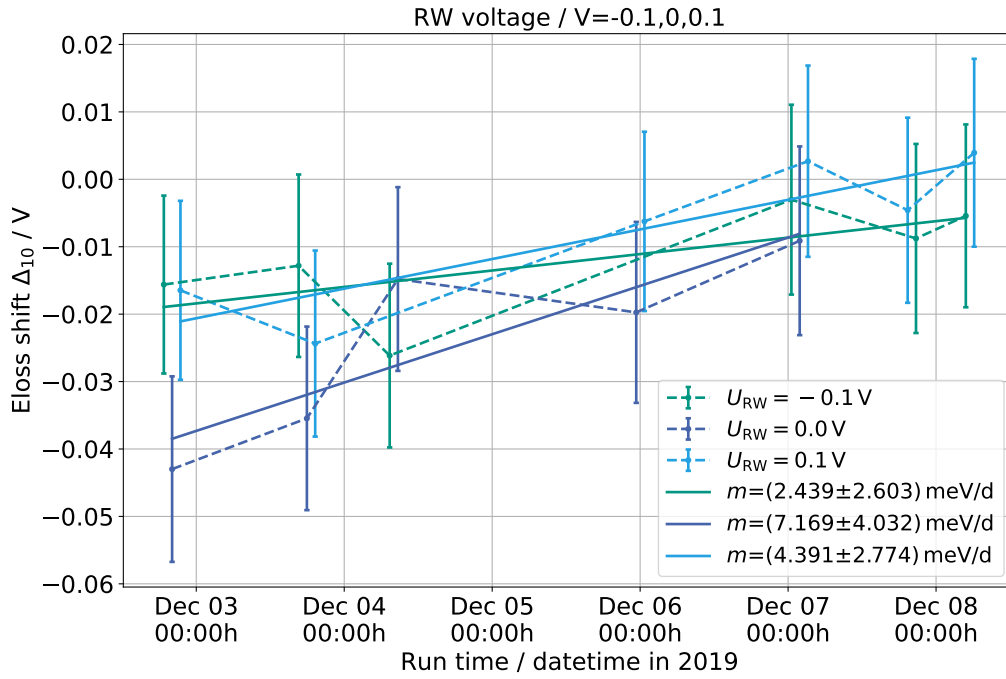


Figure 5.19: Energy loss shift parameter over time for three different rear wall voltages ($-0.1, 0, 0.1$) V. Due to the missing reference value $\bar{\epsilon}$, only the slope and the relative behavior is of relevance, not the absolute value of the y -axis. Despite the fluctuations a rise in time is visible.

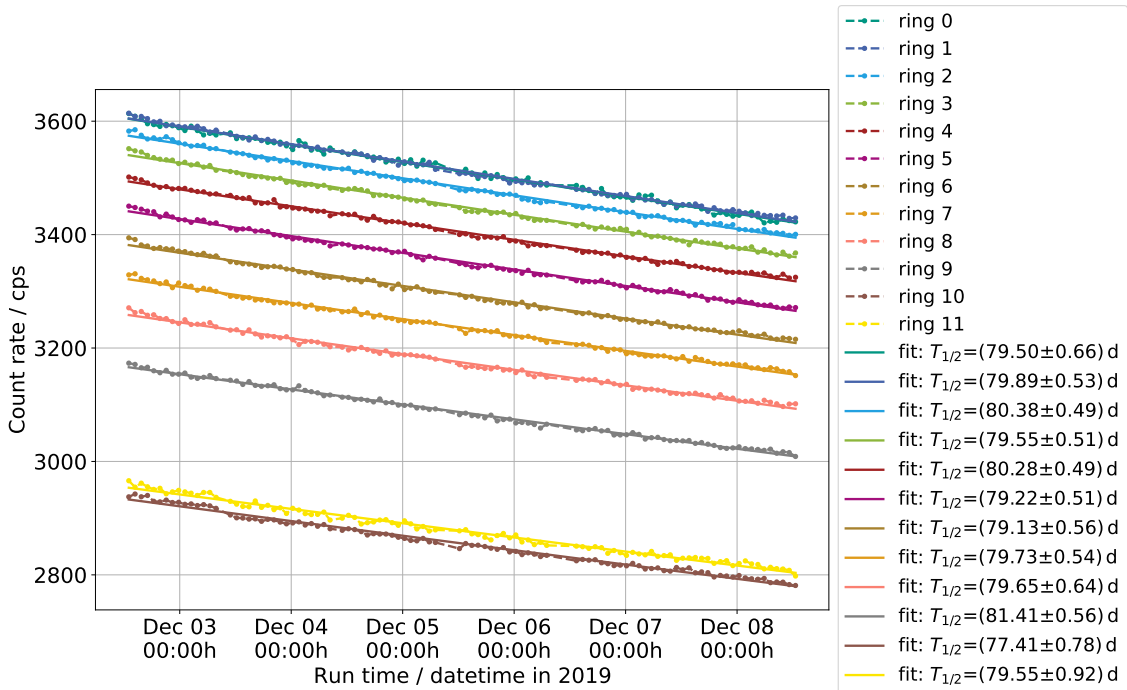


Figure 5.20: Averaged pixel-wise krypton count rate of over time for each ring. The decrease looks linear, but can exponentially be fitted for the determination of the observed half-life time of ^{83}Rb . The differences in the absolute rate and the large gap between ring 10 and 11 to ring 9 could be explained by radial non-adiabaticity and detector effects.

Krypton column density

For the determination of the krypton activity, the 60 s long stability runs at ~ 30 keV before each run can be used. At this voltage, the whole K32-transition is included and thus

a good measure for the krypton activity in the source. On the contrary, it shows strong radial effects which are caused by non-adiabatic electron transmission and pixel-dependent detection efficiencies of the detector. This is covered in Sect. 5.9.1.1.

Even so, this does not affect the time dependence as it is shown in Fig. 5.20. Conversely to the column density of tritium, the rates show a continuous decrease over time. This can be explained by the half-life time of the mother nuclide of krypton, ^{83}Rb , which has a half-life time of 86.2 d. The activity of the used krypton generator is therefore expected to decrease in the same order. Due to the short krypton half-life time of 1.83 h, the activity is given by ^{83}Rb . As a crosscheck, whether this is the main driver of the decrease, a fit of the half-life time is performed.

Crosscheck with $T_{1/2}$ fitting

The activity of a decay is characterized by a decay constant k or the half-life time $T_{1/2}$

$$k = \frac{\ln 0.5}{T_{1/2}}, \quad (5.20)$$

which describe the fraction of decayed atoms in a given period. The decay rate is therefore described via the differential equation

$$\frac{dN(t)}{dt} = -k \cdot N(t) \quad \text{and its solution} \quad N(t) = N_0 e^{-kt}. \quad (5.21)$$

In the case of a decay chain, the activity of nuclide N_2 depends on the activity of its mother nuclide N_1 . Hence, Eq. (5.21) is extended to

$$\frac{dN(t)}{dt} = -k_2 \cdot N_2(t) + k_1 \cdot N_1(t). \quad (5.22)$$

The solution of this differential equation is given by [Chr86]

$$N_2(t) = N_2^0 \cdot e^{-k_2 t} + \frac{k_1 N_1^0}{k_2 - k_1} (e^{-k_1 t} - e^{-k_2 t}). \quad (5.23)$$

In quasi-stationary approximation $k_1 \ll k_2$, k_1 can be neglected and the solution of Eq. (5.21) used for fitting the decay constant of the mother nuclide only.

As a result, a half-life time of (79.72 ± 0.40) d can be extracted from the data, which $\sim 7\%$ shorter than the literature value of 86.2 d. Hence, the decay of $^{83\text{m}}\text{Kr}$ is dominated by the decay of ^{83}Rb , but there must be an additional effect be responsible for the faster decrease, which is not identified.

5.8 Time dependent drifts of the L_3 line position

Looking at the fitted line position over time in Fig. 5.21 shows that the fitted line positions are drifting. The averaged slope of the different rear wall voltages is

$$\left\langle \frac{dE_{L_3}}{dt} \right\rangle = (-23.34 \pm 0.052) \text{ meV/d},$$

and notably negative. A negative slope of the line position corresponds to an overall increase of the source potential, either caused by the WGTS plasma or the beam tube work function. The overall drift is independent from the rear wall voltage.

In terms of time, there are four different regimes with different slopes visible. Before, during, after, and far after the CERMAX measurements.

The first regime at the beginning, until noon of December 4th, represents almost the fitted

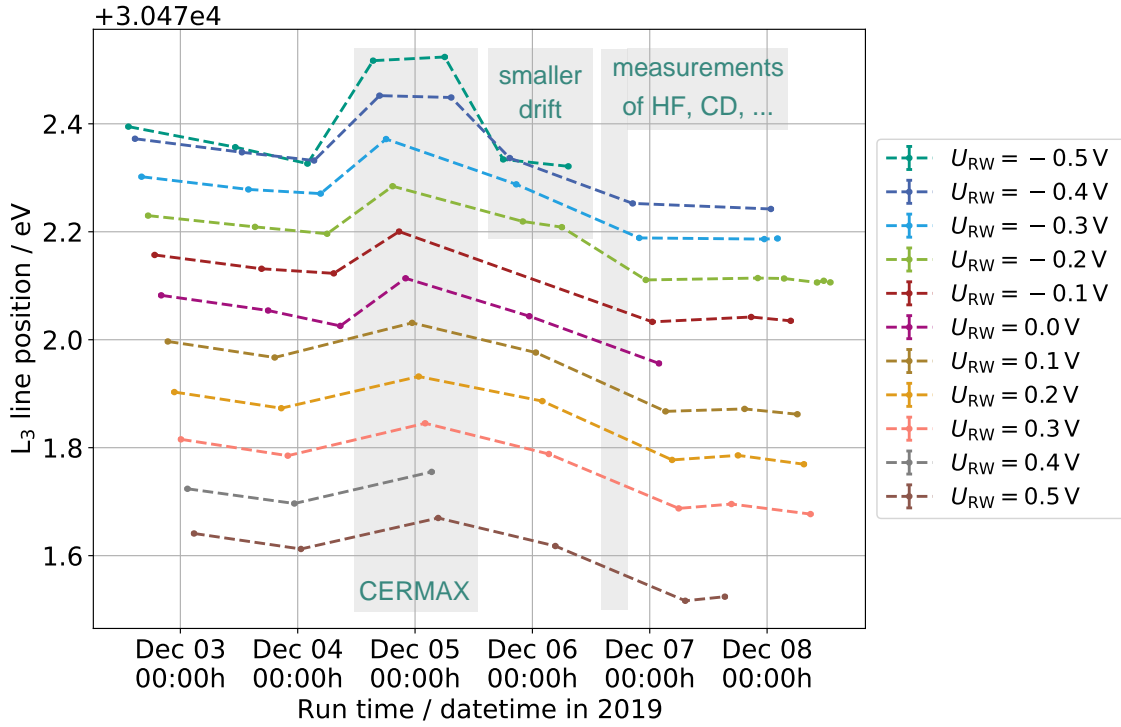


Figure 5.21: L_3 line position over time for different rear wall voltages in the good coupling regime, which have been measured at least three times. All displayed measurements drift about the same, independent from the rear wall voltage. By eye, there are four drifting regimes visible. Before, during, after, and far after the CERMAX measurements on December 4th and 5th.

slope for the whole campaign. At this time, the krypton mode with the different circulation methods of T_2 and Kr was still in “stabilization” phase, meaning adsorption processes have not reached an equilibrium.

During the CERMAX measurements, the line position globally increased which corresponds to a smaller overall plasma potential inside the source. This shows that the additional photo electrons lead to a higher negative space charge. Both measures for longitudinal inhomogeneity, the line broadening σ_0 and the energy loss shift Δ_{10} , do not show an effect during the CERMAX illumination (Fig. 5.22). Thus, the negative space charge must homogeneously evolve in the source and shift the potential without changing its shape.

Only two rear wall voltages were measured during the CERMAX illumination twice, which makes significant statements about the drift stability difficult. Nevertheless, these two measurements at $U_{RW} = -0.5$ V and $U_{RW} = -0.4$ V only show small changes of ≤ 10 meV. This could indicate that the drift is caused by something the CERMAX can counteract to. Either indirectly with the contribution of the additional photo electrons to the plasma, or directly for instance by cleaning the rear wall surface and prevent absorption of molecules. As soon as the CERMAX lamp was turned off again, the line position dropped back to where it was before. The two rear wall voltages $U_{RW} \in \{-0.5$ V, -0.2 V $\}$ which were repeated after the CERMAX measurements show a smaller drift than at the beginning.

After that, other different measurement such as high frequency measurements with the rear wall or I/U scans were performed. These measurements could have had an impact on the plasma conditions because the absolute drift increased to ~ 100 meV in less than a day. From the line positions it is difficult to conclude whether the impact of the other measurements was an overall shift of the potential or a continuous increase.

However, after these measurements, the line positions show almost no drift, but fluctuate on a small scale.

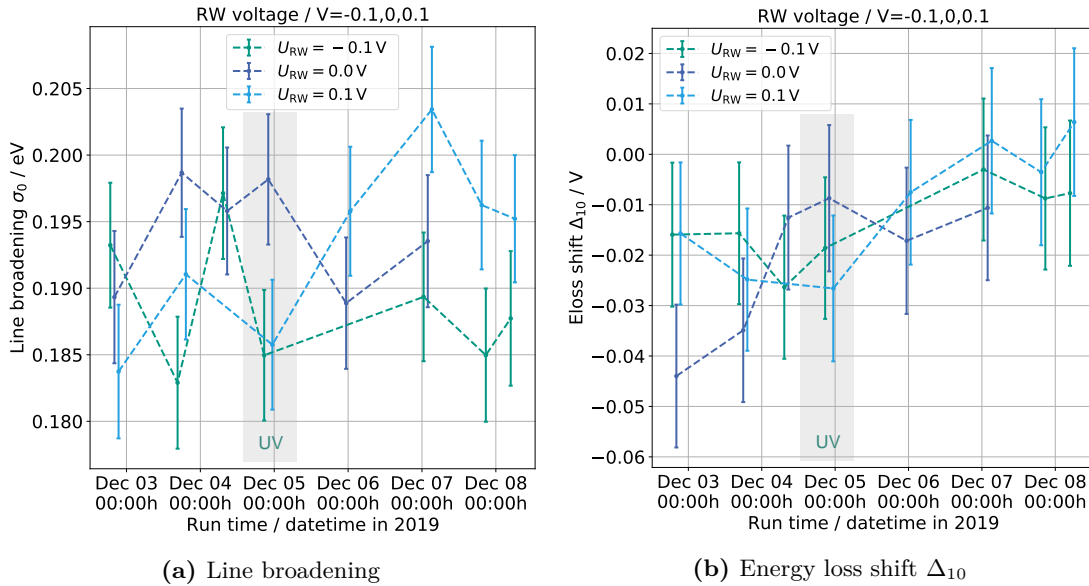


Figure 5.22: Line broadening and energy loss shift over time for the rear voltages -0.1 V, 0 V, and 0.1 V. The gray box marks the measurements which were recorded with the CERMAX illumination turned on. There is no influence of the CERMAX visible.

Possible sources which could have caused the observed drift are discussed in the following.

Column density, temperature and rear wall

As described in Sect. 3.2, the plasma depends strongly on the particle density and the temperature. A time-dependent change of these two parameters are therefore good candidates to explain the observed line position drift.

The time dependence of the total gas and the krypton column density is analyzed in Sect. 5.7. Although there are significant drifts in both column densities, it cannot satisfactorily explain the drift of the line position. The slope of the column densities are constant, whereas the drift shows regimes of different slopes.

Similar holds for the temperature. The temperature inside the source can be approximated with temperature sensors located around the WGTS beam tube. All show minor fluctuations in the range of ~ 40 mK around a constant mean. Consequently, temperature fluctuations are unlikely to be the cause of the observed drifts. One exemplary plot for the central temperature sensor is shown in Fig. 5.23.

Other systematic sources

Other measurements and calibrations have been performed between the different sweeps of the krypton runs. Some do not show a measurable influence, namely the emptying of the penning traps and I/U scans. In the morning of December 6th multiple measurements which changed slow control values and the rear wall voltage were performed for the first time within the krypton campaign. This includes column density measurements with the e-gun, PRO-KATRIN measurements, rear wall high frequency measurements, plasma fluctuation measurements, and HV calibrations.

No measurement changed the operational mode of the source. Only the magnetic and electric field of the spectrometer, and the rear wall were operated at different settings. These changes have verifiably been restored after the measurements and can be excluded as a possible cause of the drift.

Because none of the stated sources can explain the observed drift, a drift of the beam tube work function is favored. Although this cannot be verified with the existing data of KNM2,

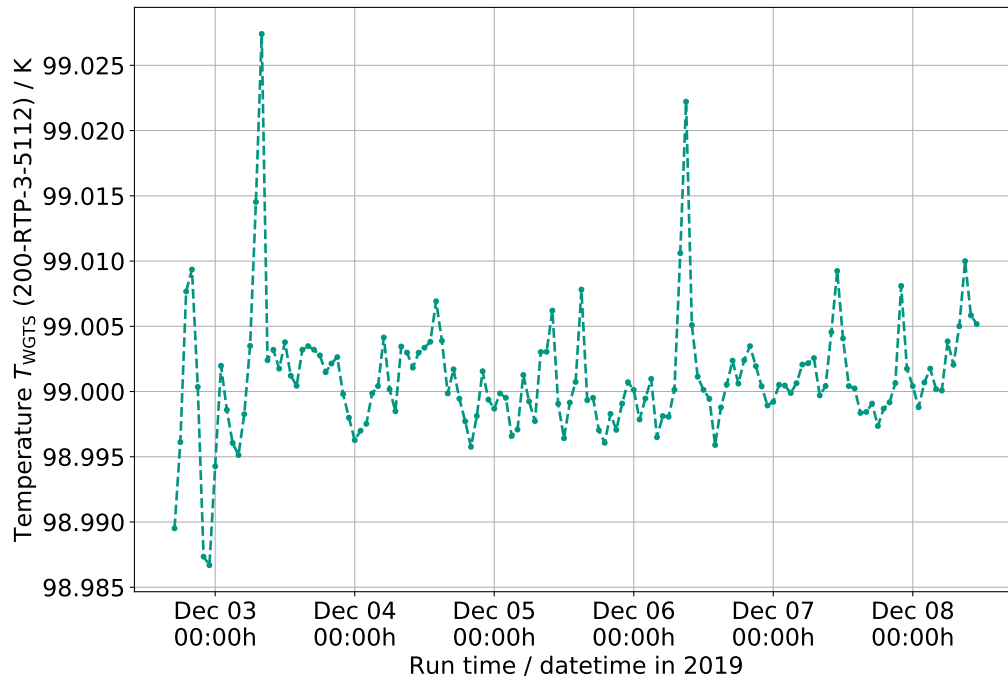


Figure 5.23: WGTS beam tube temperature over time for centrally placed temperature sensor 200-RTP-3-5112. The temperature is constant on a 0.4% level.

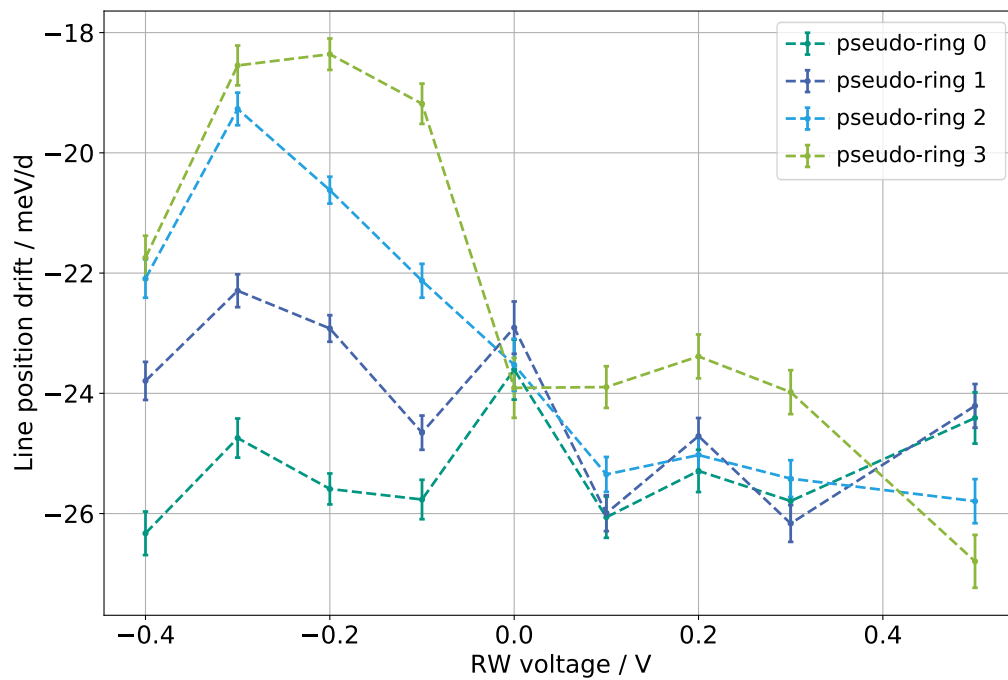


Figure 5.24: Pseudo-ring-wise line position drift depending on the rear wall voltage in the good coupling regime without the CERMAX line positions. The outermost rings show the least drift, except at $U_{RW} = 0$ V and $U_{RW} = 0.5$ V. For negative rear wall voltages the difference in radial drift is higher compared to positive ones.

dedicated measurements are planned for upcoming campaigns.

Additionally, the drifts show a radial dependence, which is investigated in the following.

5.8.1 Rear wall voltage and radially dependent drift over time

Fig. 5.24 shows the fitted drifts depending the rear wall voltage for each pseudo-ring. Only in the good coupling regime measurements were repeated often enough (> 3) to fit a slope over time. The radial drift of the line position varies strongly depending on the rear wall voltage. At negative rear wall voltages the drift of the inner rings is higher in amplitude compared to the outer ones. For positive voltages this still holds, but less clearly.

With the results from the radially dependent coupling, one can explain the observed pattern. The inner rings show better coupling to the rear wall and therefore higher absolute plasma potential values apart from the rear wall voltage of best radial homogeneity at $U_{RW, \text{hom}} \approx 160 \text{ mV}$. This can be seen in the plot, but deviates in two features. First, there should be no significant difference between negative and positive rear wall voltage in the good coupling regime, but negative rear wall voltages show higher differences of the pseudo-rings compared to positive ones. Second, the point at which are all lines cross is closer to 0 V than to $U_{RW, \text{hom}}$.

A radial dependence reduces the possible causes for the drift to the ones which are able to have a radially dependent influence.

Compared to the endpoint fit in neutrino mass measurement in KNM2, the line position drift in krypton is ~ 6 times larger and has a different structure. All slopes are negative and are mostly larger for inner radii than for outer ones. In neutrino mass measurements on the other hand, the inner radii drift the least with a small positive slope and the outer radii drift into the other direction with a larger amplitude.

Given the above, the reason for the drifts which would explain the observed shape of the different time dependent parameters cannot be identified. The fact that the CERMAX has an impact on the line position drifts with its additional electrons and surface cleaning effect, the radial pattern hints towards change of the beam tube work function.

The plasma at 30 K and higher column density in neutrino mass measurements is different to krypton conditions. Thus, different shapes of the drifts both caused by the same effect are not excluded ab initio, but the conclusion that it must originate from the same systematic cannot reliably be drawn.

5.9 Azimuthally dependent observables from misalignment

All the previous radial analyses were performed ring-wise¹. Looking in even more detailed pixel-wise analysis shows two azimuthal effects.

First, the radially decreasing rate is oscillating within one ring, even in the stability runs². This effect is independent from the rear wall voltage and can be explained by an offset of the flux tube center, i.e. a misalignment between the analyzing plane and the FPD.

Second, the line position oscillates within one ring, even if the ring-wise distribution is flat. This indicates a complex energy effect which needs sophisticated analysis.

All other observables do not show any significant azimuthal dependence.

5.9.1 Flux tube misalignment

One suitable parameter to investigate a misalignment is the background rate. It is the remaining rate at the upper end of the krypton spectrum from lines of higher energy. This includes electrons with surplus energy of more than 2 keV . At such high surplus energies, the adiabatic transmission by the magnetic field in the spectrometer is not ensured and leads to a higher loss of electrons on outer radii. The comparison with the non-adiabaticity simulations is covered in Sect. 5.9.1.1.

¹The fitting was performed pixel-wise and then averaged.

²One retarding voltage for one minute, no spectrum fitting performed.

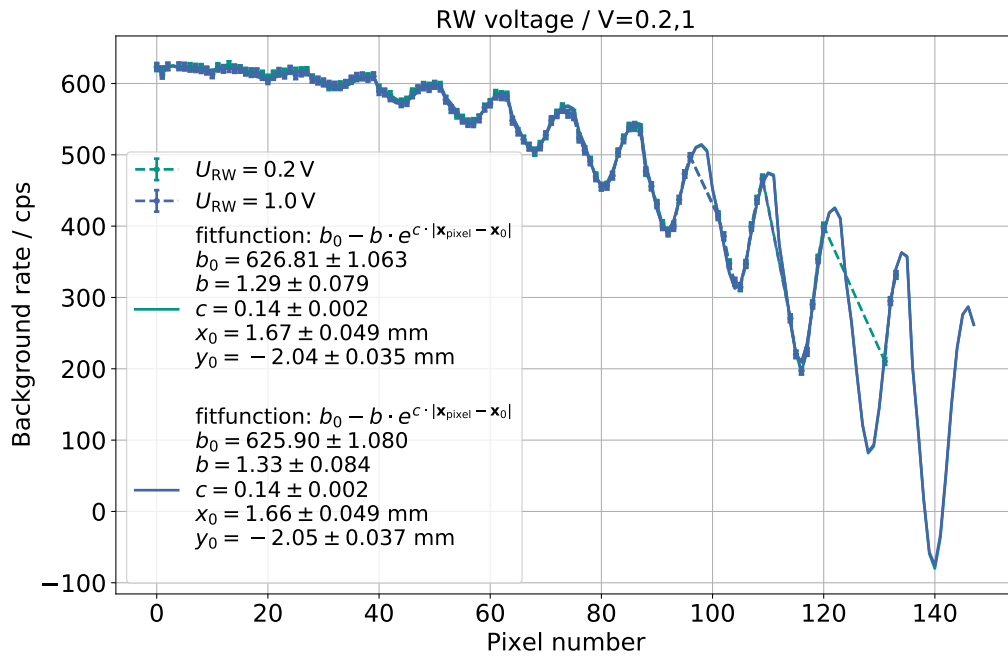


Figure 5.25: Fitted background rate over pixels for $U_{RW} = 0.2\text{ V}$ and $U_{RW} = 1\text{ V}$. Both lines show the same shape, independent from the rear wall voltage. The oscillation can be fitted by a radially decreasing exponential rate and an offset of the flux tube center.

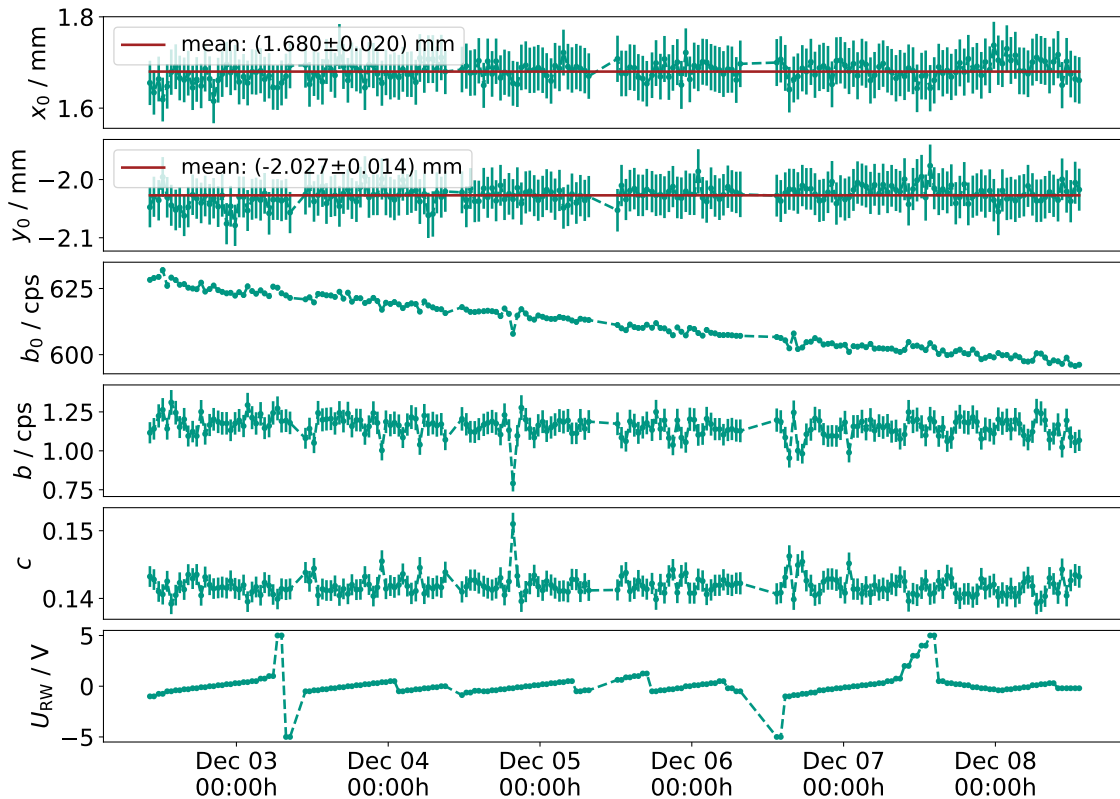


Figure 5.26: Time dependence of flux tube center offset fit parameters. The different parameters draw a consistent picture. The fitted center offset x_0 is constant over the whole campaign and the maximum rate in the bullseye b_0 decreases analog to the stability runs in Fig. 5.20.

In addition to the radial decrease, an oscillational pattern is visible which has a wavelength of 12 pixels, the number of pixels per ring. This indicates the existence of azimuthal effects because the expectation of radially symmetric distribution in a plot over pixels is a step-like pattern, in which the steps correspond to the individual rings. Inasmuch as the source activity and the field setting are assumed to be axially symmetric, the observed pattern is an indication that the center of the flux tube is not perfectly aligned to the center of the FPD.

For quantification, the background rate B is fitted with the center offset function

$$B = b_0 - b \cdot \exp^{c \cdot |x_p - x_0|} . \quad (5.24)$$

The exponential function accounts for the radially decreasing rate around the new flux tube center at x_0 and x_p are the Cartesian coordinates of pixel p . Because the coordinates of the individual FPD pixels are usually given in polar coordinates (r_p, ϕ_p) , in which r_p is the radius of the ring the pixels is in and ϕ_p the polar angle, they must be converted. Because each ring > 0 around the bullseye contains 12 pixels, the angles are given by multiples of $\pi/6$ with a ring-wise alternating offset of $\pi/12$ and 0. Then, the conversion into x_p and y_p is given by

$$x_p = r_p \cos \phi_p, \quad \text{and} \quad y_p = r_p \sin \phi_p . \quad (5.25)$$

Two exemplary fit results are shown in Fig. 5.25. The fitted curves describe the observed oscillational pattern with an average goodness of $\chi^2 = 9.84$. The obtained offset of $(x_0, y_0) \simeq (1.66, -2.05)$ mm is in the range of flux tube center offsets which have been observed before.

If the offset is a systematic effect originating from the experimental setup, it should not change significantly over time. The center offset fit is repeated for every scan in KNM2 and the fit results are shown in Fig. 5.26. One can see that the fitted offset (x_0, y_0) is constant over time and only shows statistical fluctuations over time from the average values

$$\bar{x}_0 = (1.680 \pm 0.020) \text{ mm} \quad \text{and} \quad \bar{y}_0 = (-2.027 \pm 0.014) \text{ mm} . \quad (5.26)$$

The maximum rate in the bullseye b_0 decreases correspondingly to the measured rate in the stability runs, which could be explained by the decay constant of ^{83}Rb . However, the fitted half-life of ^{83}Rb using the same method as in Sect. 5.7 is $T_{1/2} = (82.69 \pm 0.87)$ d, which is longer compared to the stability runs and closer to the literature value of 86.2 d. The amplitude and curvature of the exponential function b and c are also constant and do not show any time dependent effect. As expected from the background rate, all fitting parameters are independent from the applied rear wall voltage.

Because, the segmented FPD enables a radially dependent analysis of the flux tube, a misalignment can lead to false results because a radially dependent effect from the source is not correctly mapped onto the FPD. As a result, radial effects are wrongly averaged in ring- and pseudo-ring-wise analysis. Also, the pixel-wise calculated magnetic field and potential values do not correspond to the path the electrons have taken and lead to higher systematics.

Given the above, the fit of the flux tube center offset using the background rate has shown to be consistent. This enables the use of the values from Eq. (5.26) for the correction of the shifted flux tube center to investigate the influence on the azimuthal effect seen in energy.

Center offset correction

Because it is not trivial which fit parameters are affected by the flux tube center offset in which way, the input data get corrected and the fit repeated, i.e. the count rates from the

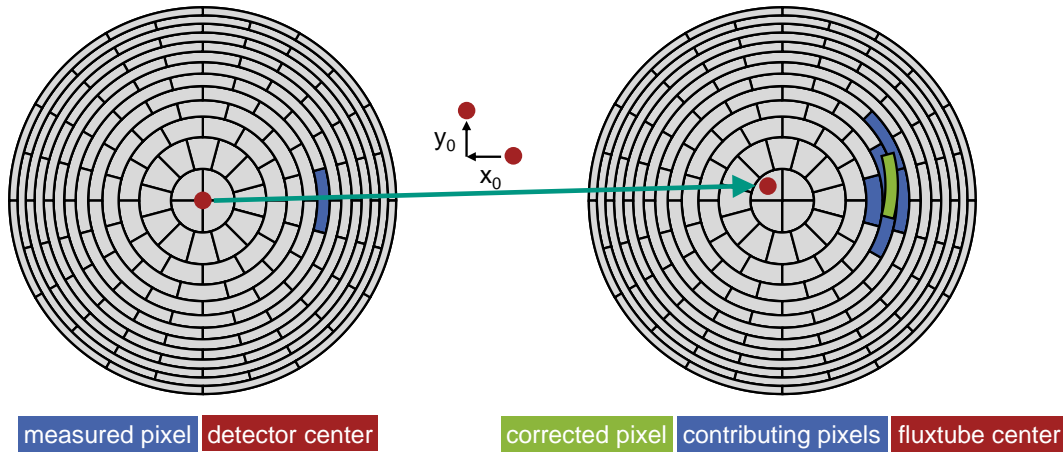


Figure 5.27: Pixel mixing method used to calculate new pixel-wise values for the count rates and the fields for the new pixel positions. The new values are weighted means of the contributing pixels, depending on the area they have in common.

run summary files and the period summary file. The latter contains pixel-wise magnetic and electric field values of the spectrometer determined by Monte Carlo simulations.

The idea of the correction is to set the FPD center around the newly fitted flux tube center. As a consequence, an arbitrary parameter $R_{\text{new},i}$ of a new pixel i has contributions from multiple old pixels. The new value of $R_{\text{new},i}$ is calculated by a weighted mean, with weights determined by the overlapping area of the new and the old pixels. This can be formulated as

$$R_{\text{new},i} = \sum_{j=0}^{147} w_{ij} R_{\text{old},j}, \quad (5.27)$$

in which w_{ij} are the normalized weights

$$w_{ij} = \frac{A_i \cap A_j}{|A_i|}. \quad (5.28)$$

In other words, w_{ij} corresponds to the relative area of the old pixel j , which lays now in pixel i . Because each pixel has the same size A , Eq. (5.28) can be simplified by $|A_i| = A$.

Fig. 5.28 shows that this method leads to the step-like pattern as expected from an aligned flux tube center onto the FPD.

On the contrary, the fitted line positions are not affected by this correction and show the same azimuthal dependence as shown in Fig. 5.29 and Fig. 5.30. This leads to the conclusion that another effect must be responsible for the azimuthal dependence in energy. One possible explanation could be two different offsets, e.g. between the source and the analyzing plane or in the calculation of the period summary files. This is further investigated in Sect. 5.9.2 after the investigation of the reason for the strong radial decrease of the background rate in the following.

5.9.1.1 Radially dependent non-adiabaticity

Because the gas dynamics simulations show no radial dependence down to a level of 10^{-5} , the radial rate distribution from the WGTS is assumed to be flat. On the contrary, the fitted column density, the fitted background rate used in the flux tube center correction, and the rate of the stability runs show an exponentially radial decrease. Because these rates include electrons with high surplus energies of > 2 keV, one explanation could be that the source activity is radially homogenous but the transmission is radially dependent

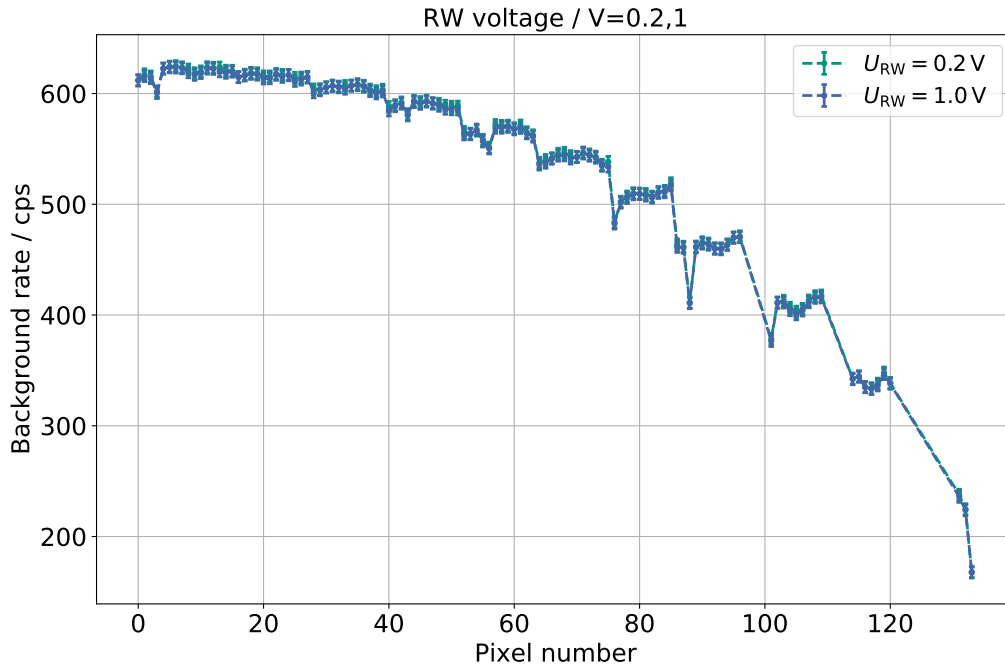


Figure 5.28: Center offset corrected fitted background rate for the first sweep. The rate shows the expected step-like pattern in the background rate which proves that the method works. There are some outliers due to detector effects, which do not affect the overall result.

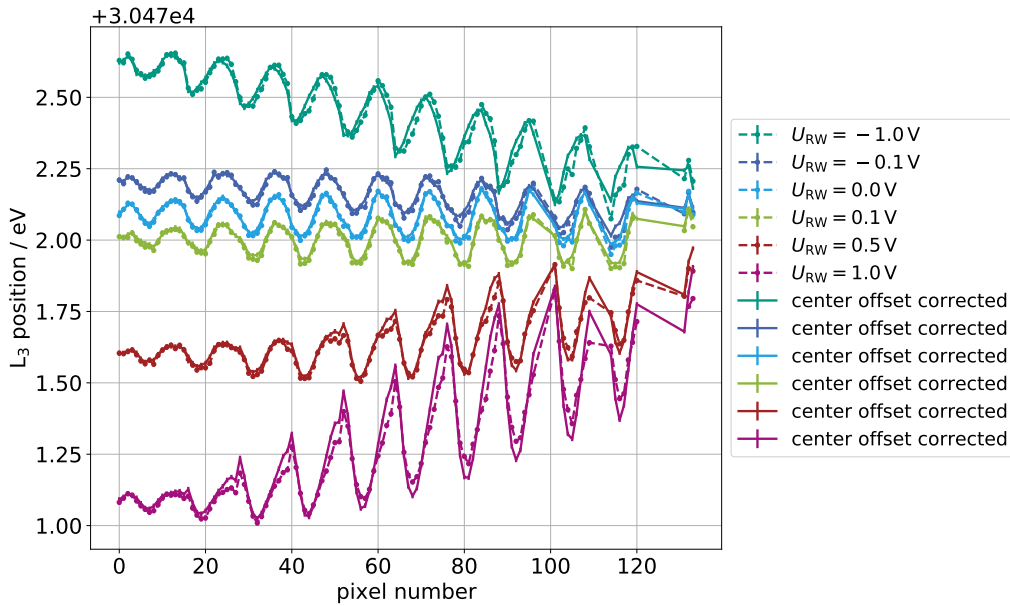
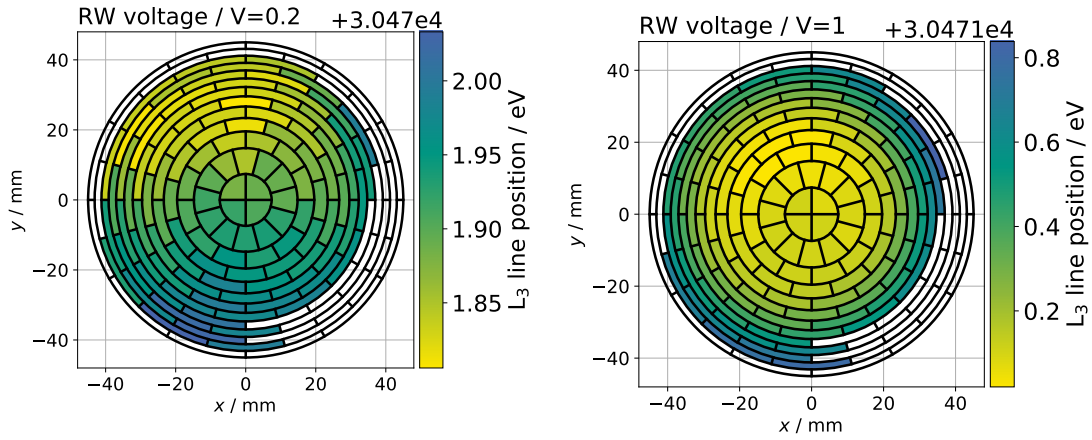


Figure 5.29: Pixel-wise line position for different rear wall voltages of both regular and center offset corrected fits for the first sweep. The line positions show corresponding results and the azimuthal pattern remains. This indicates that there is another effect responsible for the radial potential asymmetry.

and non-adiabatic due to synchrotron radiation or large initial angles. Consequently, the background rate is not constant for energies $> E_{L3}$ as it is fitted in the used krypton model, but has a slope. This introduces a large systematic effect on the fitted observables of the krypton spectrum and could explain many radial dependencies which are not explainable by physical effects, e.g. the radially decreasing fitted column density.



(a) $U_{RW} = 0.2$ V, i.e. in the good coupling regime close to where the total radial gradient is minimal. It visualizes that there is a remaining azimuthal effect, which is not simply explainable by a shift of the flux tube center. The whole part of the WGTS in which $y > 0$ shows smaller overall line position energies than for $y < 0$.

(b) $U_{RW} = 1$ V, i.e. in between the good coupling and instability regime. The external rear wall voltage dominates the pattern and the better coupling of the center becomes visible. Additionally, the center of the potential is not perfectly in the middle but shifted by a small offset.

Figure 5.30: FPD maps of the line position for the first sweep and two rear wall voltages after the rate correction, but the azimuthal pattern remains. This is a different view on the data shown in Fig. 5.29.

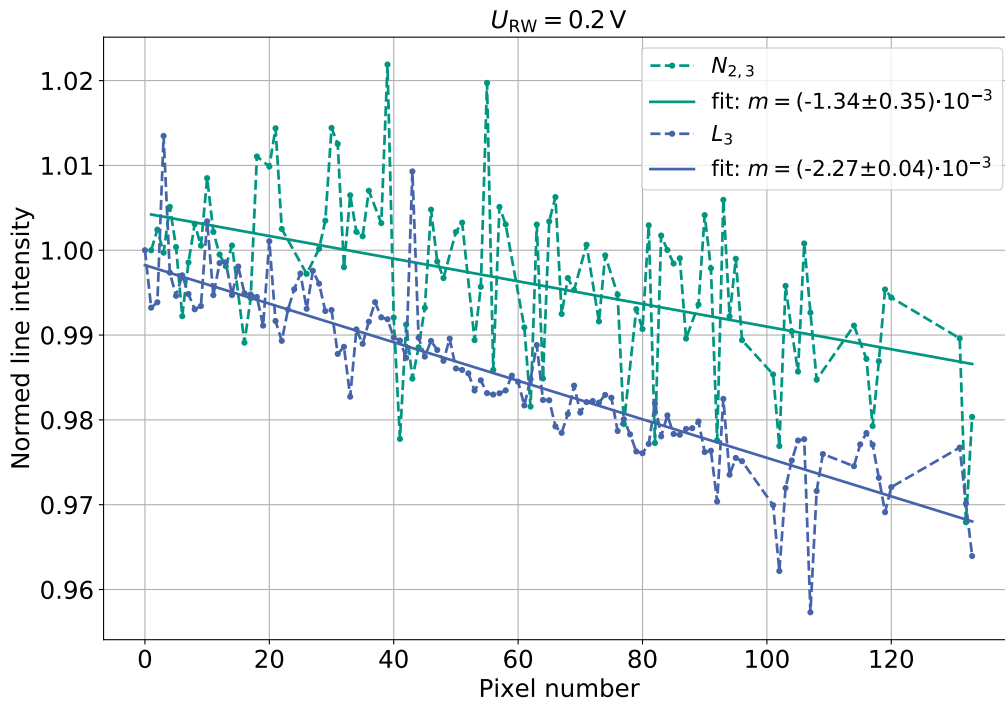


Figure 5.31: Linear fit of normed line intensity over pixel for $N_{2,3}$ and L_3 . For the latter only the first sweep is included. Due to the radially constant gas profile, the line intensities are expected to be flat. On the contrary, the observed intensities decrease by $\sim 3.5\%$ from the inside out. Both lines show a similar radial decrease, whereas the L_3 line has the additional effect of the background slope. The non-constant curve of $N_{2,3}$ can be explained by detector effects.

Additionally, looking at the fitted relative intensity of the lines L_3 and $N_{2,3}$ in Fig. 5.31 shows that a linear radial effect remains for the $N_{2,3}$ lines, which have no background.

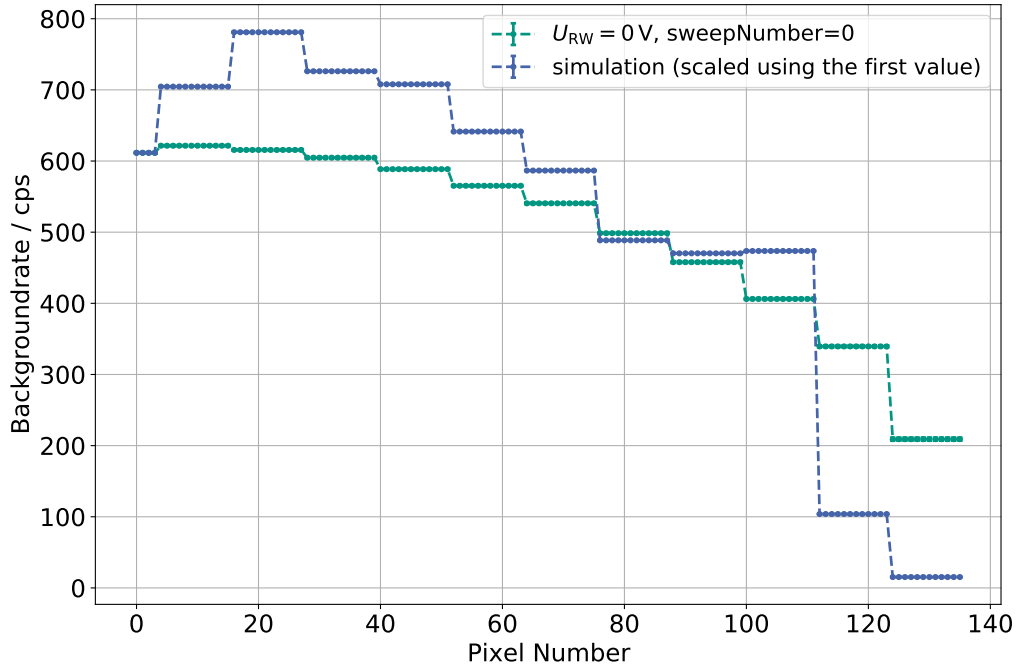


Figure 5.32: Comparison of the (center offset corrected) background rate with the simulation. One can see that both curves do not agree well with each other. Significant characteristics produced in the simulation are not observed in the measurement. However, the non-linear radial decrease is similar and the simulation data from [Wei20] is still preliminary and currently under further investigation.

However, this can be explained by detector effects.

To test if the radial decrease of the background rate is caused by non-adiabaticity, the transmission of the $L_3, M_{2,3}$ lines with their shake lines was simulated by [Wei20]. The preliminary simulated FPD signal includes the started electrons from the source, reduced by the ones which leave the flux tube or get reflected back to the source. The comparison of the simulated signal with the measured signal is shown in Fig. 5.32. Both curves, measurement and simulation, show a different behavior. The measurement is an exponentially decreasing curve, whereas the simulation shows a few characteristic points which are not observed in the measurement. First, the rate is increasing up to the second ring before it starts decreasing. Second, it shows a cutoff after pixel 111 (Ring 9) of electrons escaping the flux tube. Third, the rate almost vanishes at the outermost ring 11, whereas the measurement still has $\sim 1/3$ of the rate in the center.

Given the above, it can be concluded that the early state of the simulation cannot yet confirm the observed exponential decrease of the background rate and must be investigated further. However, the implementation of a non-constant background rate in the krypton model is indispensable for excluding its influence on other parameters.

5.9.2 Asymmetrical potential

The determination of an asymmetrical potential is challenging because it scales with the rear wall voltage. Looking at the FPD maps in Fig. 5.30 shows two manifestations of the potential offset depending on U_{RW} . At $U_{RW} = 0.2$ V, a dipole structure potential φ_0 can be seen. This potential can be explained by an misalignment of simulated pixel-wise potential values in the period summary file and the experienced electric potential of the transmitted electrons. Away from this point, at $U_{RW} \gtrsim 0.4$ V and $U_{RW} \lesssim -0.1$ V the radially dependent coupling dominates and the misalignment of the potential becomes visible as an center

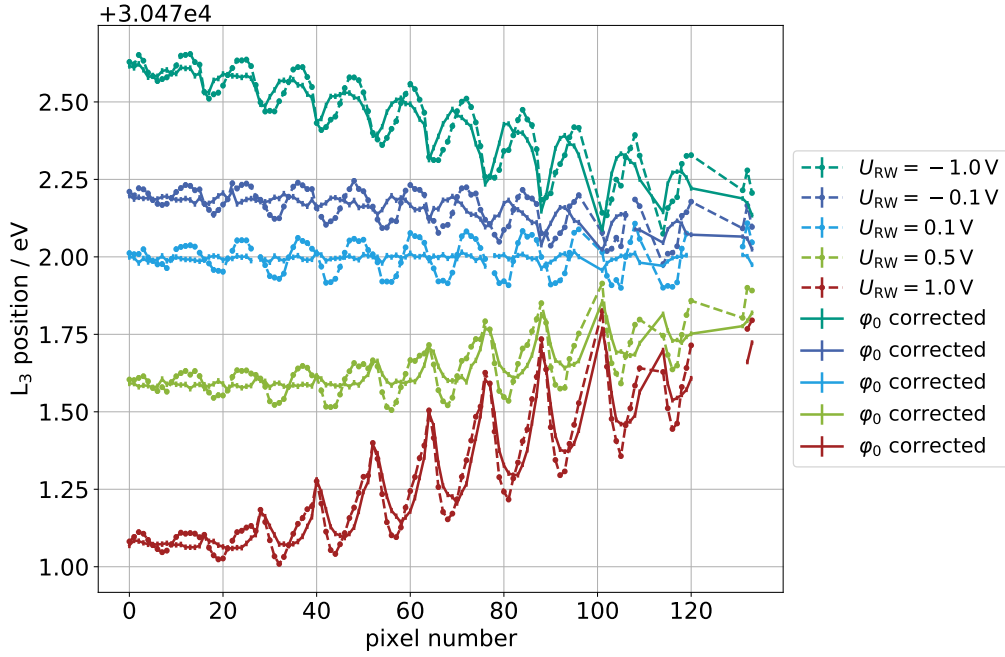


Figure 5.33: Corrected line positions with φ_0 , determined by the deviations from a linear fit of line $U_{RW} = 0.1$ V and $U_{RW} = 0.2$ V.

offset. This offset is like the observed offset in the background rate, caused by a flux-tube misalignment.

Dipole structure potential

Fig. 5.30(a) shows the fitted line positions at $U_{RW} = 0.2$ V, close to the point of maximal radial homogeneity. If averaged ring-wise, the radial potential is flat. However, a dipole structure potential is visible which can be explained by wrong pixel-wise values in the period summary file for the transmitted electrons. The reason for this is the radially dependent retarding potential of the main spectrometer, the so-called potential drop which is corrected by the pixel-wise field values of the period summary file. Adding up the pixel-wise values of both functions results in a constant distribution for all pixels. Contrarily, a shift of these two radially dependent functions leads to the observed dipole structure potential, larger values on one side and smaller values on the other side of the FPD.

The determination of this shift is difficult because for each try of a possible shift x_0 , a new period summary file which includes this shift has to be created and the spectrum fit repeated.

For this reason, the dipole structure potential is approximated as a potential $\varphi_0(p)$, determined at the point of best radial homogeneity. This allows the determination of the shift using larger absolute U_{RW} as a center offset.

The two manifestations depending on the rear wall voltage can be seen in Fig. 5.33. For small absolute rear wall voltages, e.g. $U_{RW} = 0.1$ V the amplitude of the oscillation is constant for all pixels. For larger absolute rear wall voltages on the other hand, the amplitude increases because potential differences for a given shift are larger due to the radially increasing gradient of L_3 line positions caused by the radially dependent coupling.

For the determination of φ_0 , the pixel-wise difference of the observed L_3 line positions from a linear fit is used. The chosen rear wall voltages for the linear fits are $U_{RW} = 0.1$ V and $U_{RW} = 0.2$ V because the flat curve of best radial homogeneity must be in between. Thus φ_0 is defined as

$$\varphi_0(p) = f(p) - E_{\text{main},0}(p), \quad (5.29)$$

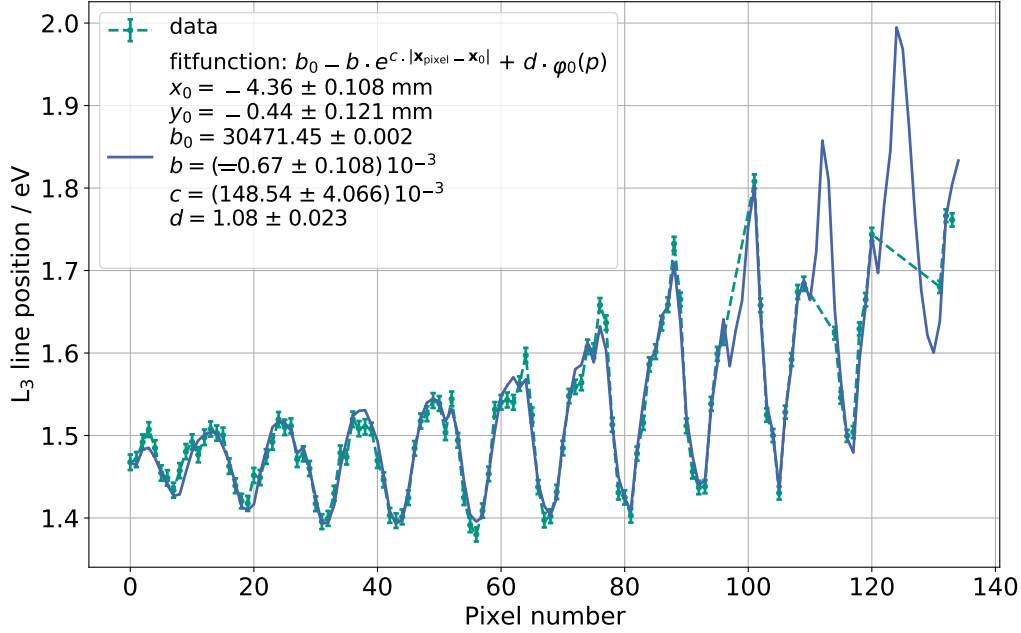


Figure 5.34: exemplary potential center offset fit for one run (58376) at $U_{RW} = 0.5$ V. The fit works well considering that φ_0 is determined phenomenologically and also shows some unsteady behavior. Even the points where the oscillational pattern is disturbed by kinks (e.g. at pixel 50) can be explained.

in which $f(p)$ is the linear fit of $E_{\text{main},0}(p)$, which are the averaged observed line position values of the two chosen rear wall voltages.

If φ_0 is subtracted from the measured line position values of the different rear wall voltages, the oscillational pattern almost disappears at inner rings for small absolute rear wall voltages and gets significantly reduced for others (Fig. 5.33). The remaining pattern can be used to determine the potential center offset by an exponential fit of the coupling, like the flux tube center offset in the background rate.

Potential center offset

Although the effect is different, with a small modification, the center offset function from Eq. (5.24) can be used. It is extended with an additional coupling term to the dipole potential φ_0 leading to

$$B = b_0 - b \cdot \exp^{c \cdot |x_p - x_0|} + d \cdot \varphi_0(p), \quad (5.30)$$

in which b_0 is the line position value for pixel 0, b is the amplitude of the radially dependent coupling approximated with an exponential function with exponent c . The Cartesian coordinates of the pixels x_p are shifted by the potential center offset of x_0 . One would expect for a constant center offset x_0 that $d = 1$ holds, independent from the rear wall voltage because it represents the coupling to the dipole structure potential, a constant difference between the period summary file and the potential drop.

As expected, the fits with the function from Eq. (5.30) work well for rear wall voltages $U_{RW} \lesssim -0.1$ V and $U_{RW} \gtrsim 0.4$ V, but not the other way around, because the center offset is determined via the radially decreasing or increasing potential, fitted by the exponential function. For small absolute rear wall voltages, this radial pattern gets negligibly small and the dipole structure potential dominates. Thus, only the runs at $U_{RW} < -0.1$ V and $U_{RW} > 0.4$ V are used for fitting. One exemplary fit result for $U_{RW} = 0.5$ V can be found in Fig. 5.34. One can see that the characteristic shape can be reproduced by the

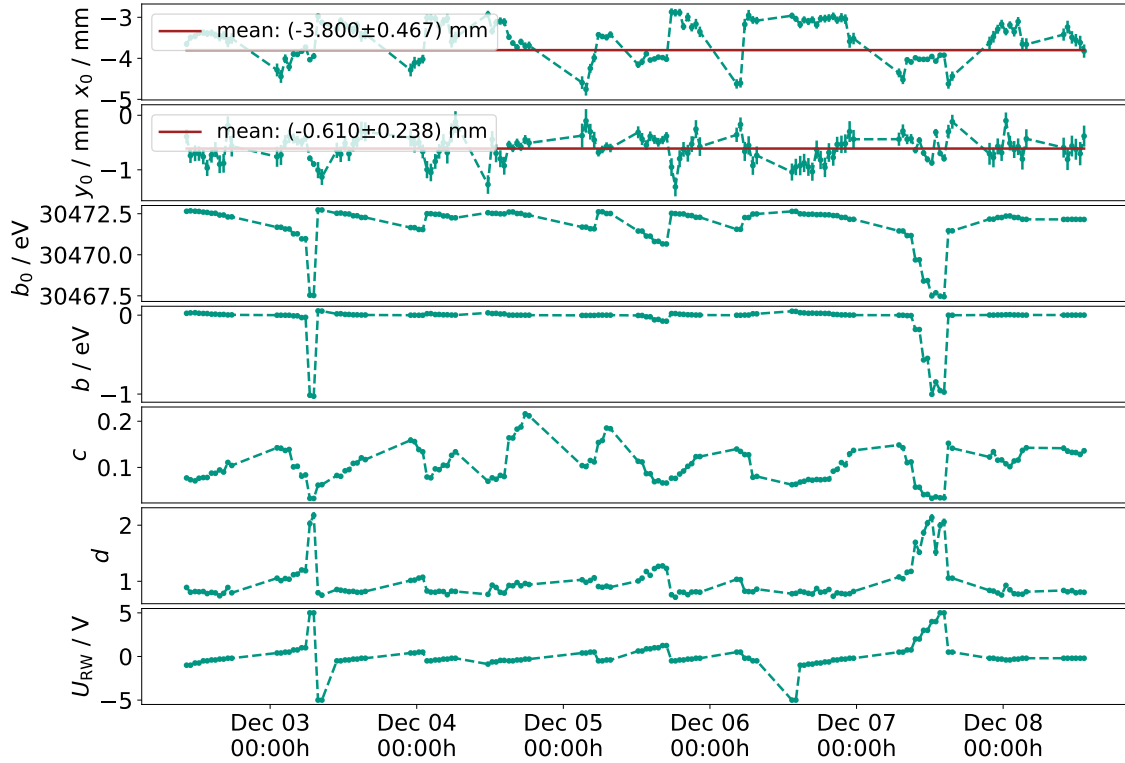


Figure 5.35: Potential center offset fit parameters of function (5.30) over time. Rear wall voltages $-0.1 \text{ V} \lesssim U_{\text{RW}} \lesssim 0.4 \text{ V}$ are excluded because in this regime c and b converge to 0 and produce arbitrary values for (x_0, y_0) . The fit parameters show a consistent behavior over time.

fit. Even the small spikes (e.g. at pixel 50) can be explained with a potential center offset. Also, the free fit parameter d is fitted to 1.08 which is larger than 1 but still compatible considering the experimental determination of φ_0 . Nonetheless, the potential offset $(x_0, y_0) = (-4.36 \text{ mm}, -0.44 \text{ mm})$ is fitted to a reasonable range of misalignment in the KATRIN setup.

Fig. 5.35 shows the fitted parameters of the fit function Eq. (5.30) for each run as a measure of time. All parameters draw a consistent picture and behave as expected. The fitted offset \mathbf{x}_0 fluctuates in range of $\sim 1.5 \text{ mm}$ in both x - and y -direction around the means of

$$\bar{x}_0 = (-3.800 \pm 0.467) \text{ mm} \quad \text{and} \quad \bar{y}_0 = (-0.610 \pm 0.238) \text{ mm}. \quad (5.31)$$

It has to be mentioned, that these values are significantly different to the ones determined by the flux tube center offset validating the existence of two different misalignment effects. The bullseye potential b_0 shows consistently the expected anticorrelation with the rear wall voltage, because of the negative charge of electrons. Likewise, the parameters of the radial coupling b and c describe the radial shape of the line position, needed to extract \mathbf{x}_0 , but are not of interest in this analysis.

Contrary to the expectation, the newly introduced parameter d shows a correlation with the rear wall voltage. This indicates that the experimental determination of the dipole structure potential by single runs is not working well. Instead, a fitting of the oscillational pattern with a trigonometric function could be used to better distinguish between the two manifestations.

Although this result shows that the oscillational pattern can be explained by a potential center offset, it is not trivial to identify where this comes from. An potential center offset

of ~ 4 mm could be created by non-axial-symmetric effects both in the beam tube due to installed components like turbo pumps or inside the spectrometers due to alignment of the electric potential between the source and the analyzing plane.

Ultimately, without further measurements and analyses, it is not possible to identify the cause of the misalignment seen in energy.

Conclusion and outlook

KATRIN has been successfully performing neutrino mass measurements since 2019. With a raw measurement time of 3 weeks, KATRIN was able to improve the existing result from predecessor experiments and set the new world-leading upper limit in direct m_ν measurements of

$$m_\nu \leq 1.1 \text{ eV}/c^2 \quad (90\% \text{ C.L.}).$$

KATRIN directly measures the kinematics of the tritium beta decay at its endpoint of 18.6 keV via high precision spectroscopy of the created electrons. To increase statistics and reduce systematics, a high luminosity source and a large scale MAC-E filter are used.

The desired goal is to reduce the sensitivity further down to 200 meV/c² (90 % C.L.) in the next 1000 days of measurement time, leading to even higher demands on the systematic budget. Thus, the inhomogeneous starting potential caused by the cold low density plasma inside the WGTS needs to be quantified and its influence minimized. For this reason, in dedicated commissioning measurement, ^{83m}Kr is additionally used in the source.

The preparation, execution, and analysis of the krypton plasma measurements in KNM2 was the topic of this thesis. In order to increase the understanding of the plasma properties of KATRIN, significant more measurement time compared to KNM1 time was devoted to the KNM2 krypton measurements. In total, 201 runs were recorded which comprise 25 different rear wall voltages. In combination with pixel-wise fitting, this allows for significant conclusions with regard to time and spatial dependencies of the plasma potential.

However, all observables showed a radial decrease which can be caused by a physical effect or by the constant approximation of the background slope. This effect complicates the analyses as they were performed in this work and summarized in the following.

Within this work, a new method was introduced to obtain the intrinsic line width by measuring both $N_{2,3}$ and L_3 line of the krypton conversion electron spectrum. As a result, the intrinsic line width could be determined to $\Gamma_{L_3}^{\text{KNM2}} = (1.011 \pm 0.028) \text{ eV}$ which draws more reasonable picture for the analysis of the line broadening compared to the reference value recorded in KNM1 and prior campaigns. However, a reference measurement of the L_3 main line position is still missing to derive the absolute scale of the plasma potential.

Within the good coupling regime in between $-0.4 \text{ V} \lesssim U_{\text{RW}} \lesssim 1 \text{ V}$, the radially dependent coupling strength was investigated using the krypton observable L_3 line position as a measure of the mean plasma potential $\langle V \rangle_0$. As a result, the radially dependent coupling strength was explainable by a diffusion driven model which features a maximal coupling of 100 % at the center of the flux tube and a decrease down to 40 % at the outermost ring.

The line broadening as a measure of the variance σ_0^2 of the potential also shows a radial decrease. The investigation of the relative line broadening $\sigma_0/\langle V \rangle_0$ removed the radial dependence for rear wall voltages $> 1 \text{ V}$, indicating that the longitudinal plasma potential shape gets scaled according to the radial coupling strength.

However, in the good coupling regime the radial dependence of the line broadening cannot be explained by the absolute radial plasma potential, but is likely to be caused by the influence of non-adiabatic transmission of background electrons.

This is supported by a remaining radial dependence of σ_0 even when $\langle V \rangle_0$ is constant for all rings, describing the U_{RW} of best radial homogeneity. The latter was determined to $U_{RW, \text{hom}} \approx 160 \text{ mV}$, using the minimal deviation of the L_3 line position values for each ring. Despite the drifting of the L_3 line positions, $U_{RW, \text{hom}}$ was constant over time and can therefore be assumed to be an intrinsic plasma property at KNM2 source conditions.

Meanwhile, comparable values were also found in the analysis of KNM3 krypton measurements, which were recorded almost half a year after KNM2.

Within the one week of krypton measurements in KNM2, the L_3 line position drifted by $\sim -24 \text{ meV/d}$. Comparing this drift to the CERMAX measurements, where the rear wall was illuminated with UV light, indicates a positive effect of the UV light on the stability of the line positions. The cause of the line positions drifts is likely to be a drift of the beam tube work functions. However, this assumption is not verified and under further investigation in KNM3.

Additionally, the drift of the krypton and tritium column densities and their influence were investigated. The decrease of the krypton rate could be traced back to the half-life time of its mother isotope ^{83}Rb . Although the gas column density increases over time, no direct influence of the column density drifts on the plasma could be identified.

Another analysis of this thesis covered the investigation of two azimuthal dependencies which can both be explained by misalignments compared to a perfectly axial-symmetric assembly of the experiment. First, the background count rates show a misalignment of $(x_0, y_0) \simeq (1.66, -2.05) \text{ mm}$, indicating an offset of the flux tube center. To study the remaining azimuthal effects, the pixel mixing method was developed, enabling a correction of the rates and the field values of the spectrometer to a new flux tube center.

The second azimuthal effect is an energy effect visible in the line position and is thus energy dependent. With extending the center offset fit function, the azimuthal energy dependence can be explained by an offset, which creates a dipole structure potential φ_0 , observed at $U_{RW, \text{hom}}$. This potential can be caused by an offset of the mapping of the electrostatic fields of either the analyzing plane or the source to the detector.

To summarize, the results of the KNM2 krypton campaign are two-sided. On one hand, the data provided by the measurement are manifold and enable a good understanding of plasma effects in the KATRIN source. On the other hand, the lack of valid plasma simulations and consideration of the background slope makes it challenging to put all different analyses into a big picture.

Outlook

The major challenges of KNM2 krypton measurements, which must be overcome in future analysis, are:

- The different operating conditions (mainly column density and temperature) of neutrino mass and krypton measurement.
- Lack of reference values.
- Large drifts of line position and column densities.
- Lack of precise knowledge of the energy loss function at 30 keV.
- Lack of consideration of the background slope.

With investigation and mitigation of the influence of these points, the understanding of the KATRIN plasma can further be improved. Thus, the analysis of the KNM2 will be repeated with a proper consideration of the background slope, which results are expected to better meet the current expectations of the plasma.

In the currently ongoing KNM3 campaign, the neutrino mass scans and the krypton measurements are both recorded at 80 K and dedicated measurements regarding the background slope at the L_3 line are performed.

Further, to obtain a precise longitudinal and radial profile of the plasma potential shape depending on the column density, temperature, magnetic fields, and rear wall voltage, a simulation has been developing, which will soon be available as the software frameworks `KARL` and `ACRONYM`.

A. Appendix

A.1 Derivation of the mass flow rate

The statistical description of the six-dimensional phase space of kinetic gases is possible with the Boltzmann transport equation [Kuc16]. The following equation

$$f(\mathbf{r}, \mathbf{v}, t) = \frac{d^6 N}{d^3 \mathbf{r} d^3 \mathbf{v}}, \quad (\text{A.1.1})$$

describes the probability of finding a particle at position \mathbf{r} and the time t with velocity \mathbf{v} . By using the method described in [SS98], neglecting all external forces and only considering binary collisions inside the gas, the transport equation for Eq. (A.1.1) can be written as

$$\frac{\partial f}{\partial t} + \mathbf{v} \frac{\partial f}{\partial \mathbf{r}} = Q(ff^*). \quad (\text{A.1.2})$$

Here, $Q(ff^*)$ is the collision integral for two particles with the distribution functions in phase space $f = f(\mathbf{r}, \mathbf{v}, t)$ and $f^* = f(\mathbf{r}, \mathbf{v}^*, t)$.

The gradients for pressure ξ_p and temperature ξ_T can be written dimensionless as

$$\xi_p = \frac{r}{p} \frac{dp}{dz}, \quad \xi_T = \frac{r}{T} \frac{dT}{dz}. \quad (\text{A.1.3})$$

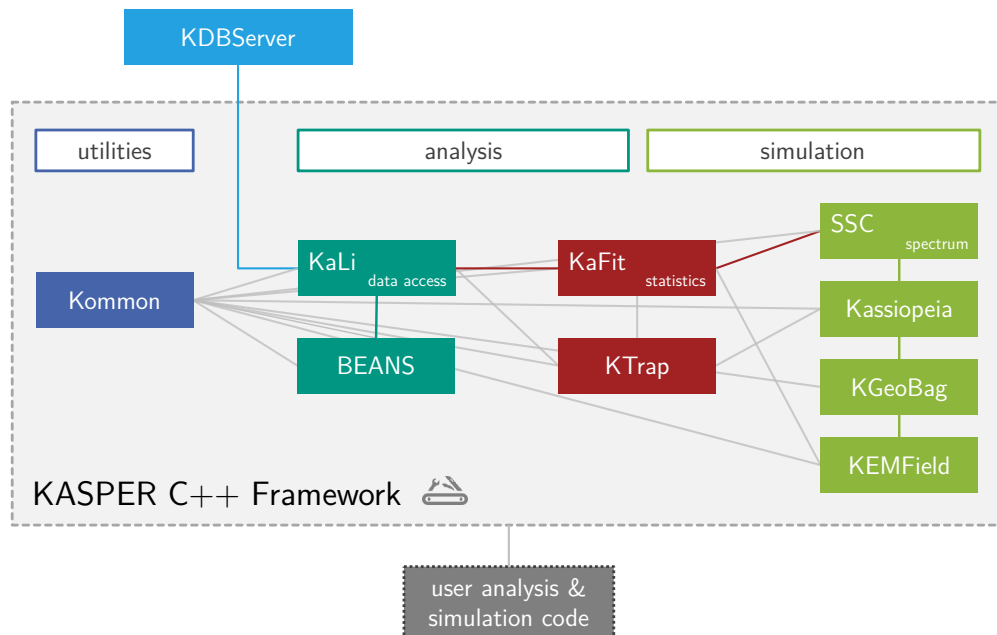


Figure A.1: Scheme of the KASPER software framework showing the different, independent elements and their connection to each other. Figure from [Kle14] (modified).

For small gradients they can be used to express the reduced flow rate

$$Q = G_p(\delta)\xi_p + G_T(\delta)\xi_T. \quad (\text{A.1.4})$$

The creep flow rates $G_p(\delta)$ and $G_T(\delta)$ can now be determined by numerically solving the linearized Boltzmann equation (Eq. (A.1.2)) and using interpolation for simplification [SS98].

Then, with the averaged $\overline{G_p(\delta)} = G$ (Poiseuille coefficient), one can obtain an equation for the mass flow rate \dot{M} , which reads as

$$\dot{M} = \frac{\pi R^3}{v_m} \left[-G \frac{\delta_{\text{in}} - \delta_{\text{out}}}{L} + G_T(\delta) \frac{p}{T} \frac{dT}{dz} \right], \quad (\text{A.1.5})$$

in which $L = 10$ m is the length of the WGTS and δ_{in} , δ_{out} the rarefaction factors at inlet and outlet position.

A.2 Retarding potential values for L_3 line runlist

The following values (in V) were used to scan the krypton L_3 line in both up and down direction. The effective potential is ~ 2 V smaller, due to the additional potential drop. The first value is just for stability control and is not used for the fitting. The distance between the values is smaller in region of the line position and larger at plateaus to save measuring time. For measuring the $N_{2,3}$ line, the values were just shifted by the distance of the line positions, i.e. ~ 1664.5 V.

29997.5, 30452, 30454, 30455, 30455.5, 30456, 30456.5, 30457, 30457.5, 30458, 30458.5, 30459, 30459.5, 30460, 30460.5, 30461, 30461.5, 30462, 30462.5, 30464.5, 30466.5, 30468.5, 30469.5, 30470.5, 30471, 30471.5, 30471.83, 30472.16, 30472.5, 30472.83, 30473.16, 30473.5, 30473.83, 30474.16, 30474.5, 30475, 30475.5, 30476.16, 30476.5, 30477.5, 30479.5, 30481.5, 30481.5, 30479.5, 30477.5, 30476.5, 30476.16, 30475.5, 30475, 30474.5, 30474.16, 30473.83, 30473.5, 30473.16, 30472.83, 30472.5, 30472.16, 30471.83, 30471.5, 30471, 30470.5, 30469.5, 30468.5, 30466.5, 30464.5, 30462.5, 30462, 30461.5, 30461, 30460.5, 30460, 30459.5, 30459, 30458.5, 30458, 30457.5, 30457, 30456.5, 30456, 30455.5, 30455, 30454, 30452

A.3 Documentation for python-based plot generator

The python class¹ `fitdata_handler` and `fitdata_plotter` can be used to create customizable scatterplots. It is designed to visualize `kafit-kandalf` fitted krypton spectra, but is generic so that it could also be used to plot other table-formatted data. The different parameters (fit results and run properties) as columns for the pixel-wise fit results in the rows. The possible properties available from krypton fits are listed in Sect. A.3.1.

It is to mention that the class is far away from “out-of-the-box”-use. All the plots needed for krypton should work, but for instance sometimes special fits need better starting parameters in order converge and to produce the desired result, or axes labels for certain parameters need to be set.

¹Source code can be found at <https://nuserv.uni-muenster.de:8443/0stertag/krypton-plot-generator>.

A.3.1 Krypton plot parameters

Available parameters for `xAxis`, `yAxis` and `legend` are the following.

```
'P11_ColumnDensityDeuterium', 'P43_LineBroadeningSquared', 'P44_LinePositionL3',
'P45_LineWidthL3Squared', 'P46_LineProbL3', 'P48_LineWidthL3SquaredShake',
'P50_ElossShift', 'P51_LinePositionL3ShakeRelative', 'P55_LineProbL3ShakeRelative',
'chi2', 'dof', 'IsSubRunWise', 'normchi2', 'pvalue', 'RunNumberFirst', 'RunNumberLast',
'runNumber', 'rwVoltage', 'runTime', 'ramp', 'cermax', 'sweepNumber', 'ring',
'radius', 'pseudoRing', 'lineBroadening', 'sweepTime'.
```

A.3.2 Class reference

Because `fitdata_plotter` is meant for user interaction, it will be explained more detailed in the following.

A.3.2.1 `__init__`

The `__init__`-function creates a `fitdata_plotter`-object, which creates a `fitdata_handler`-object, ensuring the proper initialization of the needed files for loading the plotting data.

```
__init__(fOutName="plot_data.csv", fName="merged.root",
        fMetaDataName="metadata.csv")
```

Arguments

- **fOutName:** `string`, file name of the `.csv` file, which contains all the data in table format. If this file exists, it is loaded, if not, it is created using the two files `fName` and `fMetaDataName`.
- **fName:** `string`, file name of the `.root` file, which includes the fit results of the `KaFit` fits. How this file can be created is specified in Sect. A.3.3.
- **fMetaDataName:** `string`, file name of the `.csv` file, which contains all the metadata information additional to the fit parameters. How this file can be created is specified in Sect. A.3.3.

Returns

The returned `fitdata_plotter`-object can be used to call the functions `DrawScatterplot` and `DrawHistogram`, as described the following.

A.3.2.2 `DrawScatterplot`

Main function to create scatterplots with additional functionality, which is explained in the following.

```
DrawScatterplot(xAxis, yAxis: str, splitAxis=None, excludeSplitValues=[],
        ↪ excludeXValues=[], includeXRange=[], initialOrPassFilters=[[None,
        ↪ None]], initialAndFilters=[[None, None]], initialAndNotFilters=[[None,
        ↪ None]], annotate=False, zoom=[[None, None]], fit=None, fitrange=None,
        ↪ savePlotData=False, includeCernmax=False, returnSubPlot=False,
        ↪ averageRamps=True, plotFormat=[12,7.5], removeOutlier=False,
        ↪ createPlot=True, ignoreErrors=False)
```

Arguments

- **xAxis:** `string`, parameter to plot on the x -axis. Item from Sect. A.3.1.

- **yAxis**: `string`, parameter to plot on the y -axis. Item from Sect. A.3.1.
- **splitAxis**: *optional*, `string`, parameter to separate as individual datasets in the legend. Item from Sect. A.3.1.
- **excludeSplitValues**: *optional*, `list` of values of `splitAxis` not to draw into the plot.
- **excludeXValues**: *optional*, `list` of entries of `xAxis` not to draw into the plot.
- **includeXRange**: *optional*, `tuple`, `[xMin, xMax]` to constrain the used data to a given range.
- **initialOrPassFilters**: *optional*, `list` of `tuples`, `[[parameter, value], ...]` to filter data to pass. For example, only draw the fitted line position over time for RW voltage 0.1 V and 0.5 V:

```
DrawScatterplot('runTime', 'P44_LinePositionL3',
  ↪ initialOrPassFilters=[['rwVoltage',0.1], ['rwVoltage',0.5]])
```

- **initialAndFilters**: *optional*, `list` of `tuples`, `[[parameter, value], ...]` to further constraint the data. For example, only draw the fitted line position over time for RW voltage 0.1 V and ring 0:

```
DrawScatterplot('runTime', 'P44_LinePositionL3',
  ↪ initialAndFilters=[['rwVoltage',0.1], ['ring',0]])
```

- **initialAndNotFilters**: *optional*, `list` of `tuples`, `[[parameter, value], ...]` to exclude certain values. Compared to `excludeXValues` or `excludeSplitValues` this can be used on axis, which are not plotted. For example, exclude run 54555 in a pseudo-ring-wise plot of line position over RW voltage:

```
DrawScatterplot('rwVoltage', 'P44_LinePositionL3', 'pseudoRing',
  ↪ initialAndNotFilters=[['runNumber',54555]])
```

- **annotate**: *optional*, `boolean`, whether or not to annotate the plotted data points with their value.
- **zoom**: *optional*, `list` of 2 `tuples`, `[[x_min,x_max],[y_min,y_max]]` values for changing the displayed range of the plot in x and y -direction. To use the default automatic zooming `None` can be used instead. To only draw the line position between $-2.5 \text{ V} \leq U_{\text{RW}} \leq 2.5 \text{ V}$, but to leave y open one could use

```
DrawScatterplot('rwVoltage', 'P44_LinePositionL3',
  ↪ zoom=[[-2.5,2.5], None])
```

- **fit**: *optional*, `string` of used fit. Currently implemented are `'linear'` and `'doubleLinear'`. Every dataset from the `splitAxis` is fitted independently. The fit results are plotted in the legend and returned as `fitResults`-DataFrame (see Returns paragraph below).
- **fitrange**: *optional*, `tuple`, `[x_min,x_max]` values, which are used for the fit. Only used, if `fit` is not `None`. For the fit, this is equal to `includeXRange=[x_min,x_max]`, but all the other values are still displayed.
- **savePlotData**: *optional*, `boolean`, whether or not to save the data of the plot as `*.csv`-file.
- **includeCermx**: *optional*, `boolean`, whether or not to include the cermx data.

- **returnSubPlot**: *optional*, `boolean`, whether or not to additionally return the `matplotlib.axes`-object. This can be helpful, if the plot shall be altered in some way after drawing the data in it.
- **averageRamps**: *optional*, `boolean`, whether or not to average the data of ramp up and down scans of one run to one.
- **plotFormat**: *optional*, `tuple`, size of plot canvas.
- **removeOutlier**: *optional*, `boolean`, whether or not to remove outliers. This can be used if some values are far away from the rest.
- **createPlot**: *optional*, `boolean`, whether or not to save the plot as image. This can be used for instance if just the fit results are of relevance.
- **ignoreErrors**: *optional*, `boolean`, whether or not to use and plot errors (if available).

Returns

Depending on the arguments, `DrawScatterplot` returns either one, two or three objects:

- `plotFrame` is returned. It is a `DataFrame`-object from the `pandas` library. It has the columns `'x', 'y', 'yErr', 'label'` and contains the plotted data.
- `fitResults`, `plotFrame` is returned if the argument `fit` is specified. `fitResults` is a `DataFrame`-object from the `pandas` library and contains all fitted parameters of the fit with the corresponding errors.
- `ax`, `plotFrame` is returned if the argument `returnSubPlot` equals `true`.
- `fitResults`, `ax`, `plotFrame` is returned if both arguments `returnSubPlot` and `fit` are specified.

A.3.2.3 DrawHistogram

Main function to create histograms with additional functionality, which is explained in the following.

```
DrawHistogram(yAxis, initialOrPassFilters=[[None, None]],
→ initialAndFilters=[[None, None]], initialAndNotFilters=[[None, None]],
→ fit='gauss', includeCermx=False, removeOutlier=False)
```

Arguments

- **yAxis**: `string`, parameter to use for plotting the histogram. Item from Sect. A.3.1.
- **initialOrPassFilters**: *optional*, `list` of `tuples`, `[[parameter, value], ...]` to filter data to pass. Analog to argument in `DrawScatterplot`.
- **initialAndFilters**: *optional*, `list` of `tuples`, `[[parameter, value], ...]` to further constraint the data. Analog to argument in `DrawScatterplot`.
- **initialAndNotFilters**: *optional*, `list` of `tuples`, `[[parameter, value], ...]` to exclude on not plotted axes. Analog to argument in `DrawScatterplot`.
- **fit**: *optional*, `string` of used fit. Currently implemented is Gauss, which is also set as default.
- **includeCermx**: *optional*, `boolean`, whether or not to include the cermx data.
- **removeOutlier**: *optional*, `boolean`, whether or not to remove outliers. This can be used if some values are far away from the rest.

Returns

`DrawHistogram` returns the `matplotlib.axes`-object of the drawn plot.

A.3.3 Step-by-step instructions for pixel-wise KaFit results

1. Merge the pixel-wise fit results into one `KaFitResult_Run*_pixel_mode.root` file for each run.

```
#!/bin/bash
kafit-kandalf merge --mode=pixel
```

2. Merge all the `KaFitResult_Run*_pixel_mode.root` into one single root file `merged.root`.

```
#!/bin/bash
hadd ./merged.root KaFitResult_Run0005*
```

3. In the case of the krypton, there are additional information about the runs, which are not included in the fit results file. Namely, run time, RW voltage and the ramping direction for each run. The python script below crawls through all `*.ktf` files in the folder (and subfolder) and extracts these data. The result is the `metadata.csv`-file including this information.

```
#!/bin/bash
python3 ReadMetadataFromKtfFiles.py
```

4. In order to save time and to create the possibility of using different data for plotting as well, `fitdata_handler` looks for a `plot_data.csv` file containing all the data in table format. If this file is not existing, it will create this file using `merged.root` and `metadata.csv`.

5. To create plots, two functions are available: `DrawScatterplot()` and `DrawHist()`, which are described in detail in the previous Sect. A.3.2.2 and Sect. A.3.2.3. All three parameters for `xAxis`, `yAxis` and `splitAxis` name columns in the data table and can therefore independently chosen from Sect. A.3.1. Even though, not all combinations make sense. The following snippet shows how to create a plot of the fit parameter `'P43_LineBroadeningSquared'` versus the RW voltage, split by pseudo-rings.

```
# /usr/bin/python3
from kafit_plot import *
kafitObj = fitdata_plotter()
kafitObj.DrawScatterplot('rwVoltage', 'P43_LineBroadeningSquared',
↪ 'pseudoRing')
```

A.4 Additional analysis plots

In this section are additional plots from Chap. 5 located, which provide more detailed information.

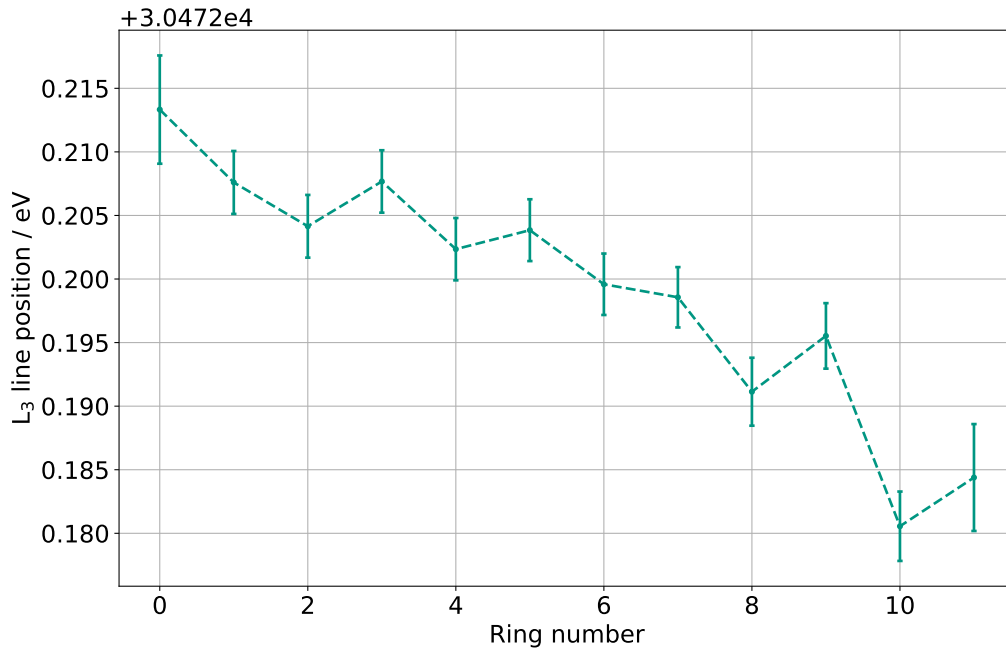


Figure A.2: Radial dependence of the line position in KNM1 reference measurement at $U_{RW} = -150$ mV.

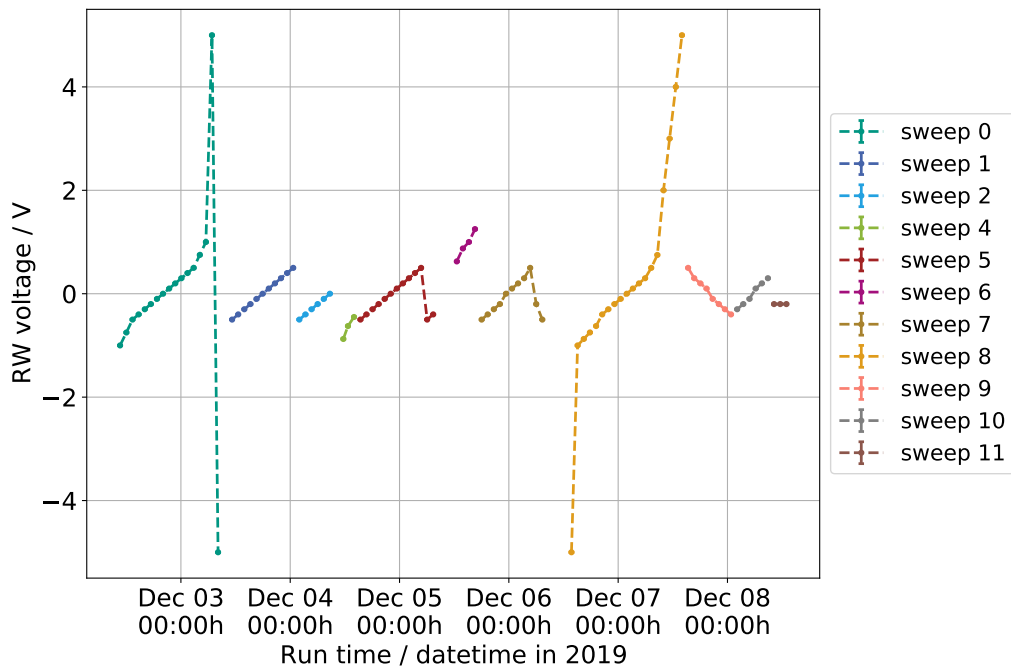


Figure A.3: Illustration of measured sweeps. Sweeps are defined as blocks of continuous measurement.

Table A.1: KNM2 krypton L_3 runs used in the analysis. Run numbers are pairs for up- and downward scans. UV corresponds to the CERMAX illumination.

Run numbers	Date and time	U_{RW} / V	UV	Run numbers	Date and time	U_{RW} / V	UV
58102 58103	02.12.2019 10:19	-1	no	58264 58265	05.12.2019 13:35	0.875	no
58105 58106	02.12.2019 11:42	-0.75	no	58267 58268	05.12.2019 14:54	1	no
58108 58109	02.12.2019 13:03	-0.5	no	58270 58271	05.12.2019 16:14	1.25	no
58111 58112	02.12.2019 14:24	-0.4	no	58274 58275	05.12.2019 17:42	-0.5	no
58114 58115	02.12.2019 15:44	-0.3	no	58277 58278	05.12.2019 19:02	-0.4	no
58117 58118	02.12.2019 17:04	-0.2	no	58280 58281	05.12.2019 20:22	-0.3	no
58120 58121	02.12.2019 18:25	-0.1	no	58283 58284	05.12.2019 21:42	-0.2	no
58123 58124	02.12.2019 19:45	0	no	58286 58287	05.12.2019 23:02	0	no
58126 58127	02.12.2019 21:06	0.1	no	58289 58290	06.12.2019 00:22	0.1	no
58129 58130	02.12.2019 22:26	0.2	no	58292 58293	06.12.2019 01:42	0.2	no
58132 58133	02.12.2019 23:47	0.3	no	58295 58296	06.12.2019 03:02	0.3	no
58135 58136	03.12.2019 01:08	0.4	no	58298 58299	06.12.2019 04:22	0.5	no
58138 58139	03.12.2019 02:28	0.5	no	58301 58302	06.12.2019 05:42	-0.2	no
58141 58142	03.12.2019 03:49	0.75	no	58304 58305	06.12.2019 07:01	-0.5	no
58144 58145	03.12.2019 05:09	1	no	58337 58338	06.12.2019 13:25	-5	no
58147 58148	03.12.2019 06:30	5	no	58340 58341	06.12.2019 14:46	-1	no
58150 58151	03.12.2019 07:50	-5	no	58343 58344	06.12.2019 16:07	-0.875	no
58153 58154	03.12.2019 10:55	-0.5	no	58346 58347	06.12.2019 17:28	-0.75	no
58156 58157	03.12.2019 12:16	-0.4	no	58349 58350	06.12.2019 18:49	-0.625	no
58159 58160	03.12.2019 13:36	-0.3	no	58352 58353	06.12.2019 20:11	-0.4	no
58162 58163	03.12.2019 14:56	-0.2	no	58355 58356	06.12.2019 21:31	-0.3	no
58165 58166	03.12.2019 16:17	-0.1	no	58358 58359	06.12.2019 22:52	-0.2	no
58168 58169	03.12.2019 17:37	0	no	58361 58362	07.12.2019 00:12	-0.1	no
58171 58172	03.12.2019 18:58	0.1	no	58364 58365	07.12.2019 01:33	0	no
58174 58175	03.12.2019 20:19	0.2	no	58367 58368	07.12.2019 02:54	0.1	no
58177 58178	03.12.2019 21:39	0.3	no	58370 58371	07.12.2019 04:14	0.2	no
58180 58181	03.12.2019 23:00	0.4	no	58373 58374	07.12.2019 05:36	0.3	no
58183 58184	04.12.2019 00:20	0.5	no	58376 58377	07.12.2019 06:56	0.5	no
58186 58187	04.12.2019 01:40	-0.5	no	58379 58380	07.12.2019 08:17	0.75	no
58189 58190	04.12.2019 03:01	-0.4	no	58382 58383	07.12.2019 09:38	2	no
58192 58193	04.12.2019 04:21	-0.3	no	58385 58386	07.12.2019 10:58	3	no
58195 58196	04.12.2019 05:42	-0.2	no	58388 58389	07.12.2019 12:19	4	no
58198 58199	04.12.2019 07:03	-0.1	no	58391 58392	07.12.2019 13:41	5	no
58201 58202	04.12.2019 08:23	0	no	58394 58395	07.12.2019 15:02	0.5	no
58210 58211	04.12.2019 12:21	-0.625	no	58397 58398	07.12.2019 16:23	0.3	no
58213 58214	04.12.2019 13:41	-0.45	no	58400 58401	07.12.2019 17:44	0.2	no
58216 58217	04.12.2019 15:06	-0.5	yes	58403 58404	07.12.2019 19:04	0.1	no
58219 58220	04.12.2019 16:25	-0.4	yes	58406 58407	07.12.2019 20:25	-0.1	no
58222 58223	04.12.2019 17:45	-0.3	yes	58409 58410	07.12.2019 21:46	-0.2	no
58225 58226	04.12.2019 19:05	-0.2	yes	58412 58413	07.12.2019 23:06	-0.3	no
58228 58229	04.12.2019 20:25	-0.1	yes	58415 58416	08.12.2019 00:27	-0.4	no
58231 58232	04.12.2019 21:44	0	yes	58418 58419	08.12.2019 01:48	-0.3	no
58234 58235	04.12.2019 23:04	0.1	yes	58421 58422	08.12.2019 03:09	-0.2	no
58237 58238	05.12.2019 00:24	0.2	yes	58424 58425	08.12.2019 04:30	-0.1	no
58240 58241	05.12.2019 01:44	0.3	yes	58427 58428	08.12.2019 05:51	0.1	no
58243 58244	05.12.2019 03:04	0.4	yes	58430 58431	08.12.2019 07:12	0.2	no
58246 58247	05.12.2019 04:25	0.5	yes	58433 58434	08.12.2019 08:33	0.3	no
58249 58250	05.12.2019 05:44	-0.5	yes	58436 58437	08.12.2019 09:54	-0.2	no
58252 58253	05.12.2019 07:04	-0.4	yes	58439 58440	08.12.2019 11:15	-0.2	no
58261 58262	05.12.2019 12:15	0.625	no	58442 58443	08.12.2019 12:36	-0.2	no

Table A.2: KNM2 krypton $N_{2,3}$ runs used in the analysis. Run numbers are for up- and downward scans. UV corresponds to the CERMAX illumination.

Run numbers	Date and time	U_{RW} / V	UV
58204 58205	04.12.2019 10:02	0.2	no

Table A.3: Sweep numbers with their included run numbers An illustration of the performed sweeps over time can be found in Fig. A.3.

Sweep number	Sweep time	Run numbers	Notes
0	2019-12-02 21:45	58059 - 58151	-
1	2019-12-03 18:15	58152 - 58184	-
2	2019-12-04 05:42	58185 - 58202	-
3	2019-12-04 10:20	58203 - 58205	$N_{2,3}$
4	2019-12-04 12:59	58206 - 58214	-
5	2019-12-04 23:43	58215 - 58253	CERMAX
6	2019-12-05 14:54	58260 - 58271	-
7	2019-12-06 01:01	58273 - 58305	-
8	2019-12-07 02:12	58336 - 58392	-
9	2019-12-07 20:25	58393 - 58416	-
10	2019-12-08 05:51	58417 - 58434	-
11	2019-12-08 11:54	58435 - 58443	-

Table A.4: KNM1 krypton L_3 reference runs used for comparison. Run numbers are for up- and downward scans. UV corresponds to the CERMAX illumination.

Run numbers	Date and time	U_{RW} / V	UV
54376 54383	28.05.2019 18:38	-0.15	no
54389 54393	28.05.2019 20:10	-0.15	no
54422 54426	29.05.2019 00:16	-0.15	no
54442 54449	29.05.2019 02:49	-0.15	no
54455 54459	29.05.2019 04:21	-0.15	no
54475 54482	29.05.2019 06:54	-0.15	no

Table A.5: 2.7 G field setting in krypton mode. The values for the eLFCS and EMCS were determined by simulation.

Coil	Current / A	Coil	Current / A
eLFCS 1	0.0	eLFCS 12	5.3
eLFCS 2	0.0	eLFCS 13	10.7
eLFCS 3	5.0	eLFCS 14	-22.0
eLFCS 4	0.0	eLFCS 15	0.0
eLFCS 5	0.0	eLFCS 16	0.0
eLFCS 6	10.0	eLFCS 17	0.0
eLFCS 7	17.0	eLFCS 18	0.0
eLFCS 8	27.0	eLFCS 19	0.0
eLFCS 9	30.0	eLFCS 20	0.0
eLFCS 10	3.0	EMCS X	0.0
eLFCS 11	9.0	EMCS Y	45.0

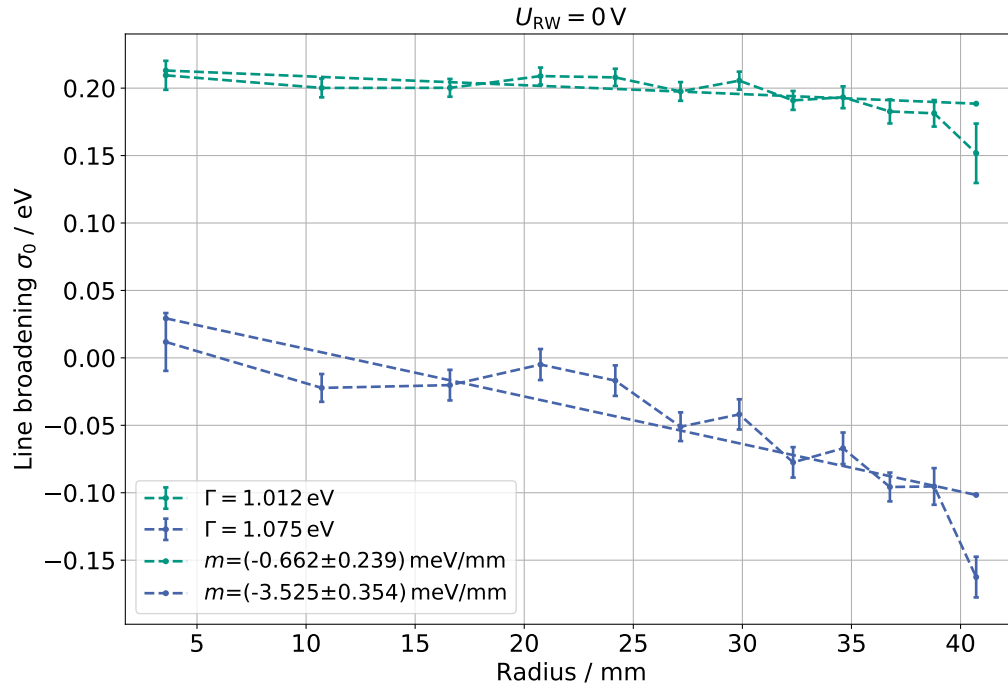


Figure A.4: Line broadening comparison for two different reference values for the intrinsic line width.

Table A.6: Pseudo-ring-wise line broadening values for $N_{2,3}$ added up from pixel-wise fitted values.

Pseudo-ring	Line broadening σ_0 / meV	Line broadening error σ_{σ_0} / meV
0	241.56	8.51
1	244.94	7.05
2	217.47	8.31
3	187.20	12.82

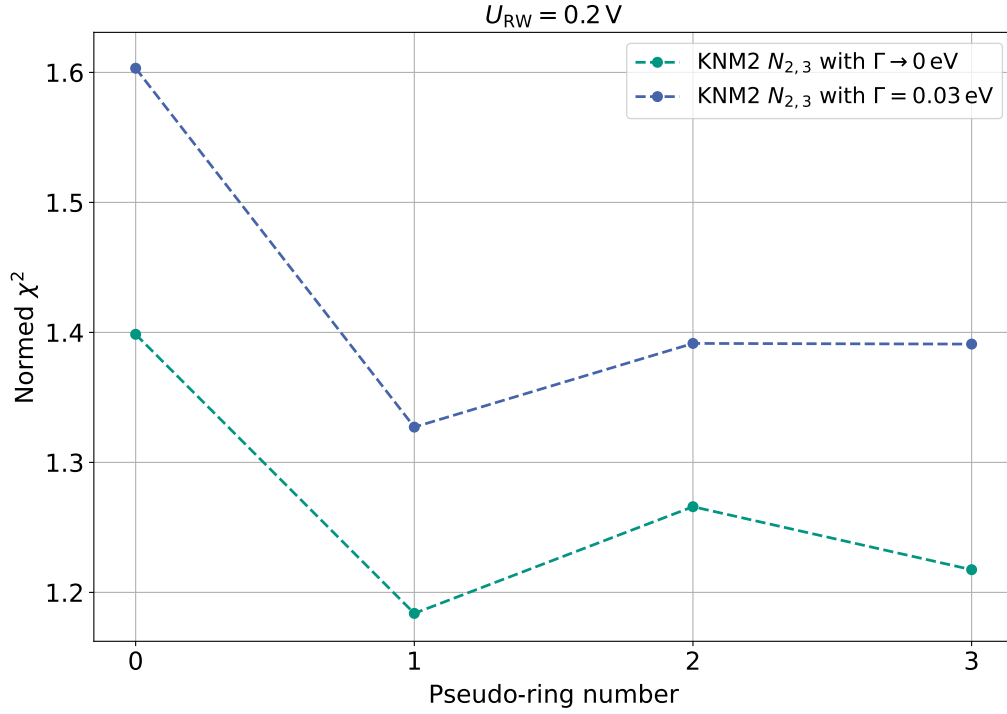


Figure A.5: Normed chi-squared for $N_{2,3}$ lines fits. On average, the normed χ^2 for the δ -function equals $\chi_{\text{norm},\delta}^2 = 1.25$ and for $\Gamma = 0.03 \text{ eV}$ it is $\chi_{\text{norm},\delta}^2 = 1.42$. In total, there are 25 degrees of freedom for the 218 converged fits.

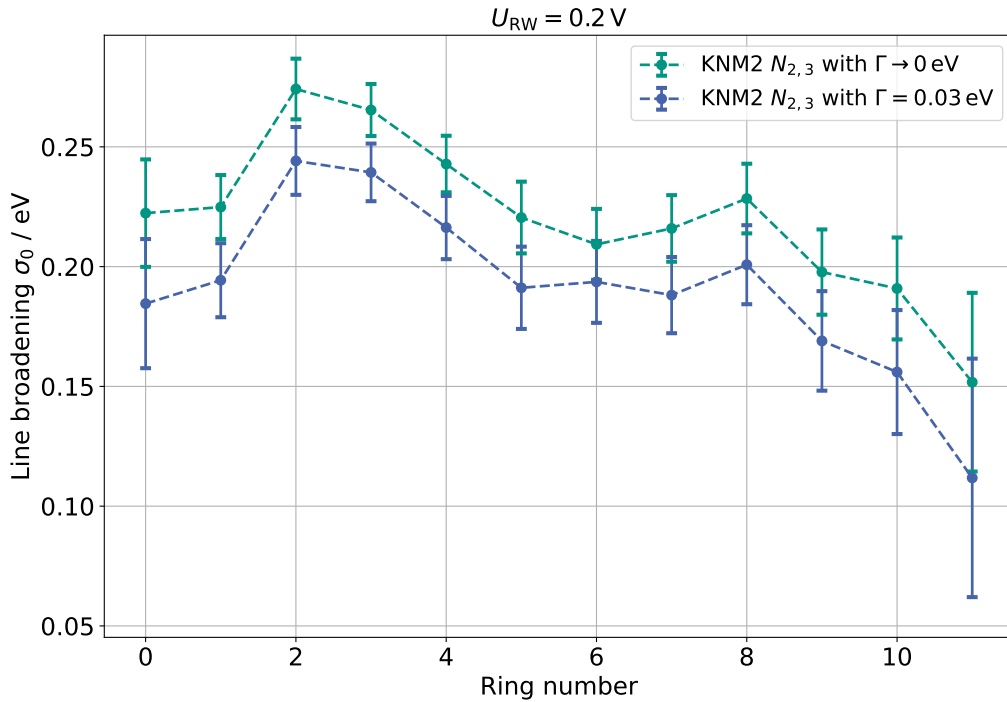


Figure A.6: Ring-wise line broadening of $N_{2,3}$ lines measurement. The intrinsic line width was assumed as a δ -function and a regular Voigt with $\Gamma = 0.03 \text{ eV}$. As expected, the line broadening is higher for the δ because it already absorbs some contribution to the total width. The errorbars are large due to the small sensitivity for these lines and the short measurement time.

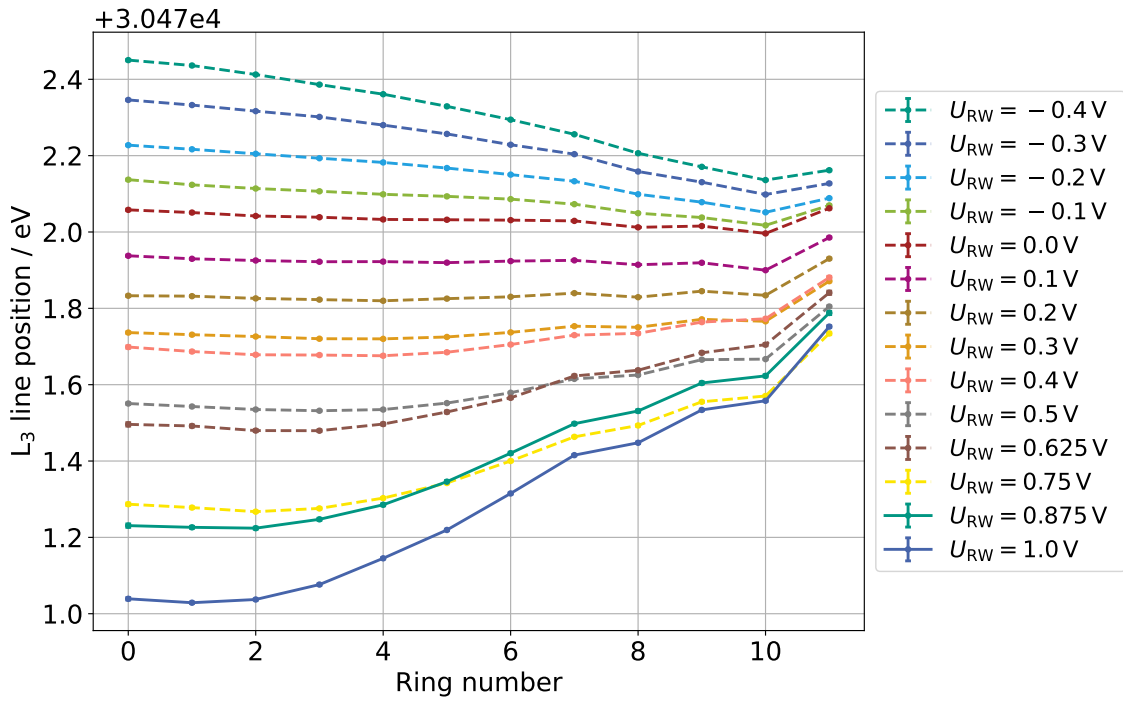


Figure A.7: Line position over ring number in the good coupling regime. The values for ring 11 show major discrepancies from the structure of the curve.

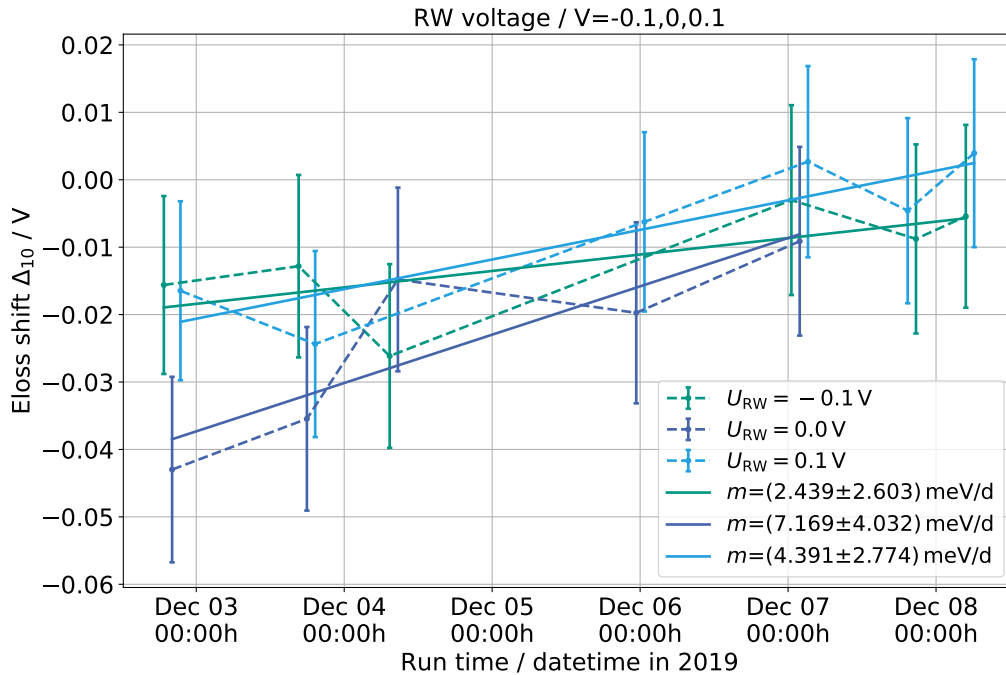


Figure A.8: Energy loss shift parameter over time for three different RW voltages ($-0.1, 0, 0.1$) V. Due to the missing reference value $\bar{\epsilon}$, only the slope and the relative behavior is of relevance, not the absolute value of the y -axis. Despite the large error bars, a clear rise in time is visible.

Bibliography

- [Ahm02] Q. R. Ahmad et al. (SNO Collaboration). “Direct Evidence for Neutrino Flavor Transformation from Neutral-Current Interactions in the Sudbury Neutrino Observatory”. *Phys. Rev. Lett.* 89.1 (2002). DOI: 10.1103/PhysRevLett.89.011301.
- [Ake+19] M. Aker et al. “Improved Upper Limit on the Neutrino Mass from a Direct Kinematic Method by KATRIN”. *Physical Review Letters* 123.22 (2019). DOI: 10.1103/physrevlett.123.221802. ISSN: 1079-7114. URL: <http://dx.doi.org/10.1103/PhysRevLett.123.221802>.
- [Ang+05] J. Angrik et al. “KATRIN Design Report 2004”. *FZKA Scientific Report 7090* (2005).
- [Arm+85] G. Armen et al. “Threshold Double Photoexcitation of Argon with Synchrotron Radiation”. *Phys. Rev. Lett.* 54 (3 1985), pp. 182–185. DOI: 10.1103/PhysRevLett.54.182. URL: <https://link.aps.org/doi/10.1103/PhysRevLett.54.182>.
- [Ase+00] V. Aseev et al. “Energy loss of 18 keV electrons in gaseous T and quench condensed D films”. *The European Physical Journal D* 10 (Mar. 2000), pp. 39–52. DOI: 10.1007/s100530050525.
- [Ase11] V. N. Aseev et al. “Upper limit on electron antineutrino mass from Troitsk experiment”. *Phys. Rev. D* 84.11 (2011). DOI: 10.1103/PhysRevD.84.112003, p. 112003.
- [Beh20] J. Behrens. *Magnetic Field uncertainties*. Internal KATRIN talk. 2020. URL: https://ikp-katrin-wiki.ikp.kit.edu/katrin/images/5/5e/AnaCall_20200317_behrens_bfields.pdf.
- [Bel+08] A. Belevsev et al. “Investigation of space-charge effects in gaseous tritium as a source of distortions of the beta spectrum observed in the Troitsk neutrino-mass experiment”. *Physics of Atomic Nuclei* 71 (Mar. 2008), pp. 427–436. DOI: 10.1134/S1063778808030046.
- [Bie17] B. Bieringer. “Designing and optimizing the UV illumination of the rear wall at the KATRIN experiment by simulation”. Bachelor’s thesis. Westfälische Wilhelms-Universität Münster, 2017.
- [Cal06] J. D. Callen. *Fundamentals of Plasma Physics*. Draft material. University of Wisconsin, Madison, 2006. URL: <http://homepages.cae.wisc.edu/~callen/book.html>.
- [Chr86] J. Christoffers. “Kinetik radioaktiver Zerfallsreihen” (1986). URL: <https://uol.de/f/5/inst/chemie/ag/occhris/download/pdf1.pdf>.
- [Cow56] C. L. Cowan Jr., F. Reines, F. B. Harrison, H. W. Kruse, A. D. McGuire. “Detection of the Free Neutrino: a Confirmation”. *Science* 124.3212 (1956). DOI: 10.1126/science.124.3212.103, pp. 103–104.

- [CP01] J. Campbell and T. Papp. “WIDTHS OF THE ATOMIC K-N7 LEVELS”. *Atomic Data and Nuclear Data Tables* 77.1 (2001), pp. 1–56. ISSN: 0092-640X. DOI: <https://doi.org/10.1006/adnd.2000.0848>. URL: <http://www.sciencedirect.com/science/article/pii/S0092640X00908489>.
- [Dan62] G. Danby, J.-M. Gaillard, K. Goulianos, L. M. Lederman, N. Mistry, M. Schwartz, J. Steinberger. “Observation of High-Energy Neutrino Reactions and the Existence of Two Kinds of Neutrinos”. *Phys. Rev. Lett.* 9.1 (1962). DOI: 10.1103/PhysRevLett.9.36, pp. 36–44.
- [Deb19] K. Debowski. “Optimization of the Integral Measurement of the Electron Energy Loss Function at KATRIN”. Master’s thesis. Karlsruhe Institute of Technology, 2019.
- [DeC89] D. DeCamp et al. (ALEPH Collaboration). “Determination of the number of light neutrino species”. *Phys. Lett. B* 231.4 (1989). DOI: 10.1016/0370-2693(89)90704-1, pp. 519–529.
- [DHH68] R. Davis Jr., D. S. Harmer, and K. C. Hoffman. “Search for Neutrinos from the Sun”. *Phys. Rev. Lett.* 20.21 (1968). DOI: 10.1103/PhysRevLett.20.1205, pp. 1205–1209.
- [Dia11] M. U. Diaz. “Off-line commissioning of a non-destructive FT-ICR detection system for monitoring the ion concentration in the KATRIN beamline”. PhD thesis. Ruprecht-Karls-Universität, Heidelberg, Germany, 2011.
- [Din05] A. Dinklage. *Plasma Physics : Confinement, Transport and Collective Effects*. Ed. by T. Klinger, G. Marx, and L. H. Schweikhard. Berlin, Heidelberg, 2005. URL: <http://swbplus.bsz-bw.de/bsz276360818cov.htm>.
- [EL98] G. C. E.L. Lehmann. *Theory of Point Estimation, Second Edition*. Berlin, Heidelberg: Springer Berlin Heidelberg, 1998. ISBN: 0-387-98502-6. URL: <https://link.springer.com/book/10.1007/b98854>.
- [Erh16] M. Erhard. “Influence of the magnetic field on the transmission characteristics and the neutrino mass systematic of the KATRIN experiment”. *Karlsruhe Institute of Technology* (2016). Dissertation.
- [Est+19] I. Esteban et al. “Global analysis of three-flavour neutrino oscillations: synergies and tensions in the determination of θ_{23} , δ_{CP} , and the mass ordering”. *Journal of High Energy Physics* 2019.1 (2019), p. 106. ISSN: 1029-8479. DOI: 10.1007/JHEP01(2019)106. URL: [https://doi.org/10.1007/JHEP01\(2019\)106](https://doi.org/10.1007/JHEP01(2019)106).
- [Fer34] E. Fermi. “Versuch einer Theorie der β -Strahlen. I”. *Zeitschrift für Physik* 88.3 - 4 (1934). DOI: 10.1007/BF01351864, pp. 161–177.
- [Fra76] R. N. Franklin. *Plasma phenomena in gas discharges*. 1976.
- [Fuk98] Y. Fukuda et al. (Super-Kamiokande Collaboration). “Evidence for Oscillation of Atmospheric Neutrinos”. *Phys. Rev. Lett.* 81.8 (1998). DOI: 10.1103/PhysRevLett.81.1562, pp. 1562–1567.
- [Ful20] A. Fulst. “Investigations of Systematics at the KATRIN Experiment”. PhD thesis, forthcoming. 2020.
- [Gal12] P. Gallagher. *Introduction to plasma physics, 2012. lecture slides*. Lecture slides. 2012. URL: https://www.tcd.ie/Physics/people/Peter.Gallagher/lectures/PlasmaPhysics/Lecture1n2_basic_properties.pdf.
- [Gro15] S. Groh. “Modeling of the response function and measurement of transmission properties of the KATRIN experiment”. PhD thesis. Karlsruhe Institute of Technology, 2015. DOI: 10.5445/IR/1000046546.

- [Har15] F. Harms. “Characterization and Minimization of Background Processes in the KATRIN Main Spectrometer”. PhD thesis. Karlsruhe Institute of Technology, 2015.
- [Hoe12] M. Hoetzel. “Simulation and analysis of source-related effects for KATRIN”. PhD thesis. Karlsruhe Institute of Technology, 2012.
- [Hua10] J. Hua. “Simulation des Kryptonmodus der Tritiumquelle WGTS im KATRIN Experiment”. Diploma thesis. Karlsruhe Institute of Technology, 2010.
- [Hut03] I. Hutchinson. *Introduction to Plasma Physics I*. Lecture slides. 2003. URL: <https://ocw.mit.edu/courses/nuclear-engineering/22-611j-introduction-to-plasma-physics-i-fall-2003/lecture-notes/>.
- [Ice11] IceCube Collaboration. “The IceCube Neutrino Observatory VI: Neutrino Oscillations, Supernova Searches, Ice Properties”. *ICRC*. paper 0848. 2011, p. 18. arXiv: 1111.2731. URL: <http://arxiv.org/abs/1111.2731>.
- [Jam98] F. James. *Function Minimization and Error Analysis*. 94.1. CERN. Geneva, Switzerland, Aug. 1998.
- [KAT01] KATRIN collaboration. “KATRIN: A next generation tritium beta decay experiment with sub-eV sensitivity for the electron neutrino mass” (2001). arXiv: 0109033. URL: <http://arxiv.org/abs/hep-ex/0109033>.
- [KCD68] M. O. Krause, T. A. Carlson, and R. D. Dismukes. “Double Electron Ejection in the Photoabsorption Process”. *Phys. Rev.* 170 (1 1968), pp. 37–47. DOI: 10.1103/PhysRev.170.37. URL: <https://link.aps.org/doi/10.1103/PhysRev.170.37>.
- [Kle14] M. Kleesiek. “A Data Analysis and Sensitivity Optimization Framework for KATRIN”. PhD thesis. Karlsruhe Institute of Technology, 2014.
- [Kle+19] M. Kleesiek et al. “ β -Decay spectrum, response function and statistical model for neutrino mass measurements with the KATRIN experiment”. *The European physical journal / C* 79.3 (2019). 51.03.01; LK 01, Article: 2014. ISSN: 1434-6044, 1434-6052. DOI: 10.1140/epjc/s10052-019-6686-7.
- [Kle19] M. Klein. “Tritium ions in KATRIN: blocking, removal and detection”. 51.03.01; LK 01. PhD thesis. Karlsruher Institut für Technologie (KIT), 2019. 340 pp. DOI: 10.5445/IR/1000093526.
- [Kle20] M. Klein. *Radial plasma potential from coupling strength (PRO-KATRIN)*. Internal KATRIN document. 2020. URL: [https://ikp-katrin-wiki.ikp.kit.edu/katrin/index.php/Radial_plasma_potential_from_coupling_strength_\(PRO-KATRIN\)](https://ikp-katrin-wiki.ikp.kit.edu/katrin/index.php/Radial_plasma_potential_from_coupling_strength_(PRO-KATRIN)).
- [Kod+01] K. Kodama et al. “Observation of tau neutrino interactions”. *Physics Letters B* 504.3 (2001), pp. 218–224. ISSN: 0370-2693. DOI: [https://doi.org/10.1016/S0370-2693\(01\)00307-0](https://doi.org/10.1016/S0370-2693(01)00307-0). URL: <http://www.sciencedirect.com/science/article/pii/S0370269301003070>.
- [Kra05] C. Kraus et al. “Final results from phase II of the Mainz neutrino mass search in tritium β decay”. *The European Physical Journal C* 40.4 (2005). DOI: 10.1140/epjc/s2005-02139-7, pp. 447–468.
- [Kri19] H. V. Krieger. *Grundlagen der Strahlungsphysik und des Strahlenschutzes*. Berlin, [2019]. URL: <http://swbplus.bsz-bw.de/bsz1684977495cov.htmhttps://doi.org/10.1007/978-3-662-60584-4>.

- [KS10] D. Kalempa and F. Sharipov. *Separation phenomenon in the Windowless Gaseous Tritium Source of KATRIN experiment. Ternary mixtures*. Technical report. 2010. URL: <http://fisica.ufpr.br/sharipov/KATRIN/report5.pdf>.
- [Kuc16] L. Kuckert. “The windowless gaseous tritium source of the KATRIN experiment - characterisation of gas dynamical and plasma properties”. PhD thesis. Karlsruhe Institute of Technology, 2016. URL: <http://dx.doi.org/10.5445/IR/1000065077>.
- [Lü10] H. Lüth. *Solid Surfaces, Interfaces and Thin Films*. Berlin, Heidelberg: Springer Berlin Heidelberg, 2010. ISBN: 978-3-642-13592-7. DOI: <https://doi.org/10.1007/978-3-642-13592-7>. URL: <http://link.springer.com/10.1007/978-3-642-29944-5>.
- [Lis17] L. Lista. *Statistical Methods for Data Analysis in Particle Physics*. Vol. 941. Lecture Notes in Physics. Heidelberg: Springer Heidelberg, 2017. ISBN: 978-3-319-62839-4. DOI: 10.1007/978-3-319-62840-0. URL: <https://link.springer.com/book/10.1007%2F978-3-319-62840-0>.
- [Loz14] V. Lozza et al. (SNO+ Collaboration). “Neutrinoless double beta decay search with SNO+”. *EPJ Web of Conferences, RPSCINT 2013 - International Workshop on Radiopure Scintillators* 65 (2014). DOI: 10.1051/epjconf/20136501003, p. 01003.
- [LY56] T. D. Lee and C. N. Yang. “Question of Parity Conservation in Weak Interactions”. *Phys. Rev.* 104 (1 1956). DOI: 10.1103/PhysRev.104.254, pp. 254–258. URL: <https://link.aps.org/doi/10.1103/PhysRev.104.254>.
- [Mac16] M. Machatschek. “Simulation of the $^{83\text{m}}\text{Kr}$ Mode of the Tritium Source of the KATRIN Experiment”. Master’s thesis. Karlsruhe Institute of Technology, 2016.
- [Mac19] M. Machatschek. *KNM1 Gaseous Krypton Campaign Report*. Internal KATRIN document. 2019.
- [Mac20] M. Machatschek. “A Phenomenological Theory of KATRIN Source Potential Systematics and its Application in Krypton-83m Calibration Measurements”. PhD thesis, forthcoming. 2020.
- [Mar19] A. Marsteller. *Krypton mode operation of the Tritium Loop*. Internal KATRIN talk, 37th collaboration meeting. 2019. URL: <https://fuzzy.fzk.de/bscw/bscw.cgi/d1305763/95-TRP-3703-P1-AMarsteller.pdf>.
- [McC15] E. McCutchan. “Nuclear data sheets for $A = 83$ ”. 125 (Mar. 2015), pp. 201–394. DOI: 10.1016/j.nds.2015.02.002.
- [McC73] F. J. McCormack. “Construction of linearized kinetic models for gaseous mixtures and molecular gases”. *The Physics of Fluids* 16.12 (1973), pp. 2095–2105. DOI: 10.1063/1.1694272. URL: <https://aip.scitation.org/doi/abs/10.1063/1.1694272>.
- [Mey85] K. v. Meyenn, ed. *Wolfgang Pauli, Wissenschaftlicher Briefwechsel mit Bohr, Einstein, Heisenberg u.a. Band II: 1930–1939*. Vol. 6. Sources in the History of Mathematics and Physical Sciences. Berlin, Heidelberg: Springer-Verlag, 1985. DOI: 10.1007/978-3-540-78801-0.
- [MSL15] M. Martinez-Sanchez and P. Lozano. *Space Propulsion*. Lecture slides. 2015. URL: <https://ocw.mit.edu/courses/aeronautics-and-astronautics/16-522-space-propulsion-spring-2015/lecture-notes/>.

- [Mur06] H. Murayama. *Quantum Mechanics I*. 2006. URL: <http://hitoshi.berkeley.edu/221a/delta.pdf>.
- [OL77] J. Olivero and R. Longbothum. “Empirical fits to the Voigt line width: A brief review”. *Journal of Quantitative Spectroscopy and Radiative Transfer* 17.2 (1977), pp. 233–236. ISSN: 0022-4073. DOI: [https://doi.org/10.1016/0022-4073\(77\)90161-3](https://doi.org/10.1016/0022-4073(77)90161-3). URL: <http://www.sciencedirect.com/science/article/pii/0022407377901613>.
- [Ost08] B. Ostrick. “Eine kondensierte $^{83\text{m}}\text{Kr}$ -Kalibrationsquelle für das KATRIN-Experiment”. PhD thesis. Westfälische Wilhelms-Universität Münster, 2008.
- [Per16] N. Perez. *Electrochemistry and Corrosion Science*. Springer-Lehrbuch. Switzerland: Springer International, 2016. ISBN: 978-3-642-29943-8. DOI: 10.1007/978-3-319-24847-9. URL: <https://link.springer.com/book/10.1007%2F978-3-319-24847-9>.
- [Pla83] R. L. Plackett. “Karl Pearson and the Chi-Squared Test”. *International Statistical Review / Revue Internationale de Statistique* 51.1 (1983), pp. 59–72. ISSN: 03067734, 17515823. URL: <http://www.jstor.org/stable/1402731>.
- [Pon67] B. Pontecorvo. “Neutrino Experiments and the Problem of Conservation of Leptonic Charge”. *Zh. Eksp. Teor. Fiz.* 53 (1967), pp. 1717–1725.
- [Rö15] M. Röllig. “Tritium analytics by beta induced X-ray spectrometry”. 51.03.01; LK 01. PhD thesis. 2015. 202 pp. DOI: 10.5445/IR/1000054050.
- [Rba] *Rubidium-83 Product Information*. 2019. URL: <https://www.isotopes.gov/sites/default/files/2019-09/Rb-83.pdf>.
- [Rei13] J. Reich. “Magnetic Field Inhomogeneities and Their Influence on Transmission and Background at the KATRIN Main Spectrometer”. PhD thesis. Karlsruhe Institute of Technology, 2013.
- [RK88] R. G. H. Robertson and D. A. Knapp. “Direct Measurements of Neutrino Mass”. *Annual Review of Nuclear and Particle Science* 38.1 (1988), pp. 185–215. DOI: 10.1146/annurev.ns.38.120188.001153. eprint: <https://doi.org/10.1146/annurev.ns.38.120188.001153>. URL: <https://doi.org/10.1146/annurev.ns.38.120188.001153>.
- [Rob10] H. Robertson. “Kinematic Determination of Neutrino Mass”. *The Future of Neutrino Mass Measurements: Terrestrial, Astrophysical, and Cosmological Measurements in the Next Decade* (2010). URL: http://www.int.washington.edu/talks/WorkShops/int_10_44W/.
- [Rob91] R. G. H. Robertson, T. J. Bowles, G. J. Stephenson Jr., D. L. Wark, J. F. Wilkerson, D. A. Knapp. “Limit on ν_e^- mass from observation of the β decay of molecular tritium”. *Phys. Rev. Lett.* 67 (1991). DOI: 10.1103/PhysRevLett.67.957, p. 957.
- [Rod18] C. Rodenbeck. “Calibration and Monitoring of KATRIN’s Precision High Voltage System with First $^{83\text{m}}\text{Kr}$ Measurements”. Master’s thesis. Karlsruhe Institute of Technology, 2018.
- [Sch16] K. Schönung. “Development of a Rear Wall for the KATRIN Rear Section and investigation of tritium compatibility of Rear Section components”. PhD thesis. PhD thesis. Karlsruher Institut für Technologie (KIT), 2016. 336 pp. DOI: 10.5445/IR/1000056077.
- [Sle15] M. Slezak. “Monitoring of the energy scale in the KATRIN neutrino experiment”. PhD thesis. Charles University in Prague, NPI Rez, 2015.

- [SM19] H. Seitz-Moskaliuk. “Characterisation of the KATRIN tritium source and evaluation of systematic effects”. 51.03.01; LK 01. PhD thesis. Karlsruher Institut für Technologie (KIT), 2019. 204 pp. DOI: 10.5445/IR/1000090748.
- [SS98] F. Sharipov and V. Seleznev. “Data on Internal Rarefied Gas Flows”. *Journal of Physical and Chemical Reference Data* 27.3 (1998), pp. 657–706. DOI: 10.1063/1.556019. URL: <https://doi.org/10.1063/1.556019>.
- [TL29] L. Tonks and I. Langmuir. “A General Theory of the Plasma of an Arc”. *Phys. Rev.* 34 (6 1929), pp. 876–922. DOI: 10.1103/PhysRev.34.876. URL: <https://link.aps.org/doi/10.1103/PhysRev.34.876>.
- [Vén+18] D. Vénos et al. “Properties of ^{83m}Kr conversion electrons and their use in the KATRIN experiment”. *Journal of Instrumentation* 13.02 (2018), T02012–T02012. DOI: 10.1088/1748-0221/13/02/t02012. URL: <https://doi.org/10.1088/1748-0221/13/02/t02012>.
- [War+91] D. L. Wark et al. “Correspondence of electron spectra from photoionization and nuclear internal conversion”. *Phys. Rev. Lett.* 67 (17 1991), pp. 2291–2294. DOI: 10.1103/PhysRevLett.67.2291. URL: <https://link.aps.org/doi/10.1103/PhysRevLett.67.2291>.
- [WB35] E. Wigner and J. Bardeen. “Theory of the Work Functions of Monovalent Metals”. *Phys. Rev.* 48 (1 1935), pp. 84–87. DOI: 10.1103/PhysRev.48.84. URL: <https://link.aps.org/doi/10.1103/PhysRev.48.84>.
- [Wei20] E. Weiss. *Non-adiabaticity simulation*. Internal KATRIN document. 2020. URL: https://ikp-katrin-wiki.ikp.kit.edu/katrin/index.php/File:Non_adiabaticity_simulations.png.
- [Wu+57] C. S. Wu et al. “Experimental Test of Parity Conservation in Beta Decay”. *Phys. Rev.* 105.4 (1957). DOI: 10.1103/PhysRev.105.1413, pp. 1413–1415.
- [WW30] V. Weisskopf and E. Wigner. “Berechnung der natürlichen Linienbreite auf Grund der Diracschen Lichttheorie”. *Zeitschrift für Physik* 63 (1930), pp. 54–73. DOI: 10.1007/BF01336768. URL: <https://doi.org/10.1007/BF01336768>.

Danksagung

Am Ende möchte ich mich bei all denjenigen bedanken, die mich während meiner Arbeit im letzten Jahr unterstützt haben. Besonders hervorheben möchte ich:

- Prof. Dr. Guido Drexlin, der mir meine Masterarbeit bei KATRIN ermöglicht hat und mich in der Zeit auf vielseitige Art und Weise gefordert und gefördert hat.
- Prof. Dr. Ulrich Husemann, für die Übernahme des Korreferats.
- Dr. Magnus Schlösser, für die zielorientierte und inspirierende Form der Leitung des Plasma Teams.
- Moritz Machatschek, für die ununterbrochene Unterstützung in allen Fragen, die Einarbeitung in bestehende Frameworks, die Arbeitsteilung während der Messphase und den Durchblick bei der Interpretation der Ergebnisse.
- Dr. Manuel Klein, für die entspannte Atmosphäre im Büro, die Einführung in Plasma, die Hilfestellung und Kreativität bei der Erstellung von Analysen.
- Fabian Friedel, für die Einführung ins Plasma Team, die zielstrebige Arbeitsweise und das Kennen der richtigen Ansprechpartner für viele Themen.
- Caroline Rodenbeck, für die Einarbeitung im Kontrollraum und die Unterstützung bei der Automatisierung unserer Messungen.
- Klaus Mehret, der jeden Tag aufs Neue für abwechslungsreiche Gespräche gesorgt hat und für die wichtigste Konstante in meinem Tagesablauf verantwortlich war: Mittagessen um 11:30.
- Meine Frau Lissy, die dafür gesorgt hat, dass ich mich besonders an längeren Tagen im Institut immer auf zu Hause gefreut habe. Danke für die Freiheit bei den vielen Abenden, an denen ich noch am Computer saß und die gemeinsamen Mittagessen in Zeiten von Corona und Home Office.
- Meine Eltern Annette und Roland, die mir mein gesamtes Studium erst ermöglicht haben und mich während der ganzen Zeit durchweg unterstützt und begleitet haben. Danke, dass ich mich immer frei in allen Entscheidungen gefühlt habe.
- Erneut Fabian Friedel, Manuel Klein und Moritz Machatschek für das ausführliche Korrekturlesen dieser Arbeit.

Genereller Dank geht an die gesamte KATRIN Gruppe für die tolle Atmosphäre, die sich vor allem durch ihre konsequente Hilfsbereitschaft auszeichnet.